

DISSERTATION

CALIBRATION OF THE PIERRE AUGER OBSERVATORY FLUORESCENCE DETECTORS AND
THE EFFECT ON MEASUREMENTS

Submitted by

Ben Gookin

Department of Physics

In partial fulfillment of the requirements

For the Degree of Doctor of Philosophy

Colorado State University

Fort Collins, Colorado

Summer 2015

Doctoral Committee:

Advisor: John Harton

Walter Toki
Kristen Buchanan
Carmen Menoni

Copyright by Ben Gookin 2015

All Rights Reserved

ABSTRACT

CALIBRATION OF THE PIERRE AUGER OBSERVATORY FLUORESCENCE DETECTORS AND THE EFFECT ON MEASUREMENTS

The Pierre Auger Observatory is a high-energy cosmic ray observatory located in Malargüe, Mendoza, Argentina. It is used to probe the highest energy particles in the Universe, with energies greater than 10^{18} eV, which strike the Earth constantly. The observatory uses two techniques to observe the air shower initiated by a cosmic ray: a surface detector composed of an array of more than 1600 water Cherenkov tanks covering 3000 km^2 , and 27 nitrogen fluorescence telescopes overlooking this array. The Cherenkov detectors run all the time and therefore have high statistics on the air showers. The fluorescence detectors run only on clear moonless nights, but observe the longitudinal development of the air shower and make a calorimetric measure of its energy. The energy measurement from the the fluorescence detectors is used to cross calibrate the surface detectors, and makes the measurements made by the Auger Observatory surface detector highly model-independent. The calibration of the fluorescence detectors is then of the utmost importance to the measurements of the Observatory. Described here are the methods of the absolute and multi-wavelength calibration of the fluorescence detectors, and improvements in each leading to a reduction in calibration uncertainties to 4% and 3.5%, respectively. Also presented here are the effects of introducing a new, and more detailed, multi-wavelength calibration on the fluorescence detector energy estimation and the depth of the air shower maximum measurement, leading to a change of $1 \pm 0.03\%$ in the absolute energy scale at 10^{18} eV, and a negligible change in the measurement on shower maximum.

ACKNOWLEDGEMENTS

I am deeply grateful for the people this department has afforded me to meet. Wendy helped me to navigate the perilous logistics of graduate school, and still somehow remained my friend, and for that, I am eternally thankful. I am in the debt of the other graduate students that, like me, thought it was a good idea to go to graduate school. The friendships that formed in our shared misery, and the encouragement we offered one another are something I will cherish; including Leif for creating this \LaTeX dissertation document class. I could not imagine a better research group to be a part of. Alexei's attention to detail helped to further my understanding from cosmic ray particle physics to infrared soldering techniques. Jeff was the first member of the group I met when I visited seven years ago, and I will never forget his giddiness at the prospect of me attending CSU. If I only know how much time I would be spending in his office bouncing ideas of each other regarding calibration conundrums, and various car maintenance issues, it was where most of my graduate education took place. John was suspiciously absent when I visited, but if he had been around I would not have believed he was going to be my advisor. His patience, (constant) reassurance, and willingness to chat physics or anything else are exceedingly rare qualities in a mentor that have helped me immeasurably. I am thankful for the support of my family, my mom and dad, and brother, who cultivated my scientific curiosities.

Most of all I would like to acknowledge Sara. Her love and encouragement are what have kept me going. She is a continuous source of inspiration, whose confidence and support are what I admire and love greatly about her. Her willingness to listen to my prattling about my work and physics is a testament to her patience and virtue. And lastly, I cannot forget Ferdy, my writing buddy, he made sure everything made sense.

TABLE OF CONTENTS

Abstract	ii
Acknowledgements	iii
Chapter 1. Cosmic Rays	1
1.1. Cosmic Origin of Contamination	3
1.1.1. Victor Hess and his Discovery	4
1.2. Detection Methods and Early Discoveries	4
1.2.1. Detector Improvements	5
1.2.2. The Beginnings of the Particle Zoo	6
1.2.3. Air Showers and Very High Energies	9
1.3. Current Understanding of Cosmic Rays	11
1.3.1. The Extensive Air Shower (EAS)	11
1.3.2. Glimpses of Composition	15
1.3.3. Ground Arrays	16
1.3.4. Particle Flux and the Cosmic Ray Energy Spectrum	18
1.3.5. Energy Spectrum and Acceleration Mechanism Hypotheses	20
1.3.6. The Cosmic Microwave Background and its Implications	22
Chapter 2. The Pierre Auger Observatory	26
2.1. The Surface Detector	27
2.2. The Fluorescence Detector	31
2.2.1. Fluorescence Light Detection	32
2.2.2. The Pierre Auger Observatory Fluorescence Telescope	33
2.2.3. The FD Camera	36

2.2.4.	The PMT and Triggering Schemes.....	37
2.2.5.	Monitoring and Calibration.....	39
2.3.	Recent Extensions of the Observatory.....	44
2.3.1.	HEAT and AMIGA	45
2.4.	Overview of Results.....	47
2.4.1.	Energy Spectrum.....	47
2.4.2.	Composition	49
Chapter 3.	Calibration.....	53
3.1.	Surface Detector Calibration	53
3.1.1.	The vertical-equivalent Muon.....	54
3.2.	Fluorescence Detector Calibration.....	57
3.2.1.	Atmospheric Calibration.....	58
3.2.2.	Relative Calibration.....	60
3.3.	Absolute Calibration and the “Drum” Light Source	63
3.3.1.	The Drum and its Calibration.....	63
3.3.2.	Absolute Calibration of the Fluorescence Detectors	77
3.3.3.	Reduction of Uncertainties	79
3.4.	The Multi-wavelength Calibration.....	80
3.4.1.	History of the Multi-Wavelength Calibration.....	81
3.4.2.	Monochromator-based Multi-Wavelength Calibration	84
3.4.3.	The Multi-wavelength Drum Emission Spectrum.....	90
3.4.4.	Lab PMT Quantum Efficiency.....	93
3.4.5.	Uncertainties in Lab Measurements in Malargüe.....	96
3.4.6.	Multi-Wavelength Calibration of the Fluorescence Detectors	98

3.4.7.	Uncertainties in FD Measurements	99
3.4.8.	Photodiode Monitor Data	105
3.5.	Calculation of the FD Efficiency	105
3.5.1.	FD Efficiency.....	106
3.5.2.	Final Uncertainty Calculation	107
3.5.3.	Comparisons Between Differently Constructed Telescopes	108
3.5.4.	FD Efficiencies	110
3.6.	New Calibrations: Now What?.....	111
Chapter 4. The Effects of Calibrations on Measurements		112
4.1.	Hybrid Data.....	113
4.1.1.	Hybrid Geometry.....	114
4.1.2.	Measuring the Longitudinal Profile	117
4.1.3.	Fluorescence Yield	118
4.1.4.	Attenuation of Fluorescence Light	120
4.2.	Building the Analysis	122
4.2.1.	Showers Simulations.....	123
4.2.2.	Auger Offline Software Framework.....	123
4.2.3.	Hybrid Reconstruction	126
4.3.	Measurements	127
4.3.1.	Data Selection.....	127
4.3.2.	Energy Estimation	130
4.3.3.	Showers Maximum, X_{max}	136
4.3.4.	Distance Dependence	147
4.3.5.	Azimuth Dependence.....	151

Chapter 5. Conclusions	157
5.1. Absolute FD Calibration	157
5.2. Detailed Multi-wavelength Calibration	157
5.2.1. Effect on FD physics measurements	158
5.3. Outlook	159
Bibliography	160
Appendix A. Measured Multi-Wavelength Calibrations	181
Appendix B. Reconstructed X_{max} Distributions	184

CHAPTER 1

COSMIC RAYS

The discovery of the highest energy cosmic particles has a terrestrial origin story, and as often happens in physics, a combination of serendipity and intrepid perseverance illuminated the shadows of human ignorance. At the turn of the twentieth century physicists were busy fumbling about with, as Pierre Auger put it, their newly developed “sixth sense regarding [their] measurement of phenomena outside our sensory experience” [1], meaning experimenting with new forms of radiation. The early work in new forms of radiation would quickly turn into an odyssey into the invisible world of subatomic particles, and the physics governing them, and revolutionize our understanding of the universe.

Roentgen’s discovery of x-rays in 1895 had extended the known electromagnetic radiation into a realm of highly penetrating light. The following year, spurred on by Roentgen’s rays, Becquerel’s experiments with photographic films and seemingly phosphorescent uranium salts led him to wonder if these types of materials emitted an energetic and penetrating radiation similar to Roentgen’s x-rays. He found that the materials were not phosphorescent, but instead spontaneously ionized and exposed his photographic plates without an external energy source, such as the sun [2]. The phenomena demonstrated by these certain elements was another newly discovered form of radiation Marie Curie later called “radioactivity” during her and husband’s experiments [3]. Becquerel later showed that the radiation he had observed was different than x-rays, due to its deflection in the presence of electromagnetic fields, similar to cathode rays, and thus showed that radioactive elements emit radiation in the form of charged particles [4]. Soon after Becquerel’s discovery, the Curies showed that other elements besides uranium are radioactive.

With the knowledge of these new forms of radiation, the phenomena that Crookes [5] and Wilson [6] investigated could be explained. Twenty years prior to the discovery of x-rays, during his investigations into “radiant matter” Crookes found that an electrically charged object would not retain its charge, even when in a sealed and insulated chamber. He then evacuated the chamber and found that the object would keep its charge, and hypothesized that when air was present within the chamber it was somehow forming ions, and thereby allowing the charge to escape. The radioactivity discovered by Becquerel and others could explain how the air inside Crooke’s chamber became ionized. The radioactive particles penetrated through the glass chamber and ionized the air within. In 1901, after the discovery of radioactivity, Wilson wanted to better understand how air inside a sealed chamber is ionized by radioactive elements, he sought to make more quantitative measurements of the ionization using a gold leaf electroscope. Wilson’s electroscope could measure the rate at which the charge leaked off the gold leaf, thereby measuring the rate of ionization within the volume of air surrounding the leaf. In his experiments with the electroscope Wilson found little control over the rate at which it discharged, and found the rates at which different gases within the chamber ionized were similar to the known rates from radioactive elements as shown by the Curies [7].

The understanding then was that the air within an electroscope chamber was being ionized by radioactive “contamination of the walls and the gas, [and] radiations from the surrounding bodies” [1]. When the physicists attempted to reduce the contamination from known forms of radiation and radioactivity, they discovered there was another form radiation bombarding their detectors that was extremely penetrating and eventually found to be non-terrestrial.

1.1. COSMIC ORIGIN OF CONTAMINATION

Following Wilson's work with his electroscope, physicists tried to determine the cause of the ionization of air in terms of the known radiation at the time. Ideally, the first step was to attempt to stop the air within an electroscope from ionizing, and then introduce known ionizing agents, such as uranium, to determine what could be causing the charge to leak from the electroscope. However, preventing the air from ionizing proved to be more difficult than anticipated, as this "residual" radiation seemed to be ever-present. Pacini made measurements on multiple continents and on the oceans and found that the radiation was everywhere and concluded that the radiation must be coming from within the earth's crust [8]. Cathode rays, x-rays, and radioactivity were all easily stopped by a few centimeters of lead shielding, so naturally researchers assumed that enclosing an electroscope in a two centimeter lead shield should stop the ionization, but this is not what was observed [9]. Instead the rate was decreased by a factor of two, a decrease attributable to shielding the electroscope from radiation emanating from the ground [1].

Physicists sought to increase the shielding from radiation coming from earth by moving their electroscopes away from the ground, which meant ascending tall buildings or using balloons. Before these experiments could be carried out, improvements to the electroscopes and ionization chambers were needed to make them more portable and unaffected by changes in environment such as large changes in air pressure. The first attempt at measuring the radiation away from its seemingly terrestrial source was performed by Father Theodore Wulf, and using electroscopes of his own design he made measurements at the top of the Eiffel tower. Father Wulf found that the ionization rate decreased by 64%, however this was less than he calculated for the absorption of the air between him and the ground below [10].

1.1.1. VICTOR HESS AND HIS DISCOVERY. To perform the ultimate test of whether the Earth was the source of the radiation, Victor Hess made seven balloon flights in 1912, and using Wulf electroscopes measured the ionization rate as a function of altitude up to 5300 m [11]. He found that the ionization increased with altitude and concluded that radiation with very high penetrating power enters the earth's atmosphere from above, calling it *höhenstrahlung* [12], which translates to "rays from the sky".

After Hess' initial flights in 1912, young physicist Wener Kolhörster made subsequent balloon flights to higher altitudes, ~ 8 km [13], in 1913 and confirmed Hess' findings that the ionization rate increased with altitude to a rate of about thirty times that of what was measured on the ground; data are shown in figure 1.1.

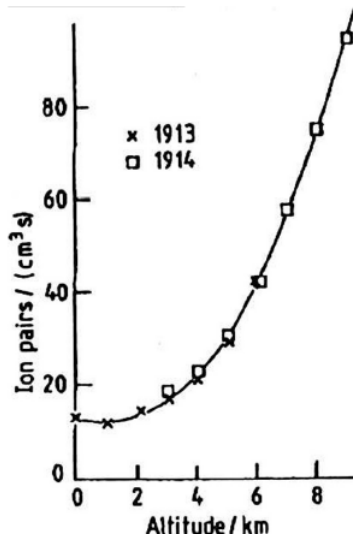


FIGURE 1.1. Measurements made by Kolhörster on his balloon flights showing that the rate of ionization, measured in ion pairs per unit volume, increases with altitude [14].

1.2. DETECTION METHODS AND EARLY DISCOVERIES

Shortly after Kolhörster made his measurements confirming Hess' initial work, World War I erupted and all research relevant to *höhenstrahlung* ceased until the early 1920s.

When physicists restarted their investigations after the war they sought to understand just how penetrating this new form of radiation really was and to learn its true nature.

1.2.1. DETECTOR IMPROVEMENTS. After the war, interest in Hess' "rays from the sky" grew around the world and peaked the curiosity of prominent American physicist Robert Millikan. Millikan wanted to make his own measurements about the highly penetrating radiation permeating the atmosphere, and so he and his graduate student, Otis, took on this task. Their work culminated in Otis' 1924 dissertation that concluded the penetrating radiation was not coming from beyond earth [15]. Millikan continued this study of the radiation and eventually he reversed his conclusion and agreed with Hess. Otis' career in physics was short-lived. Then during a lecture at Leeds University, Millikan in detailing his experiments with the famous radiation explained that it does not originate from within earth's atmosphere, and it therefore should be named "cosmic rays" [16].

With its new moniker, physicists were poised to take on the challenge of measuring the properties cosmic rays, and up first was determining just how penetrating these rays are. Hess and others had already demonstrated that the cosmic rays were highly penetrating since they must traverse the atmosphere with ease, but to determine just how penetrating cosmic rays are, physicists employed clever shielding strategies. Natural cosmic ray shields were used by physicists by taking their sensitive instruments underground below large bodies of water or deep into mines. Improvements to the instruments allowed for better measurements in these remote and rugged locations. The workhorse of ionization detection, the Geiger tube, had been improved in collaboration with Müller [17], and then in pioneering work Bothe and Kolhörster developed coincidence counting techniques using the Geiger-Müller tubes [18]. Even with these improved detectors physicists found that the cosmic rays penetrated through all thicknesses of earth and water.

Work done in atmospheric physics regarding cloud formation and nucleation theory of condensation was concurrent with the development of cosmic ray physics, and Wilson was instrumental in both. After his experiments with gold leaf electroscopes Wilson again aided the progress of cosmic ray research, but this time it was with his work in condensation and cloud formation. By the 1900s physicists had shown that dust particles were the cause of nucleation sites in condensation of adiabatically cooled gases [19, 20]. After the discover of x-rays, physicists wondered if the ions produced in the gas by the radiation could be sites of nucleation, and in 1898 Thomson demonstrated this using a beam of x-rays focused on a gas chamber [21]. To be sure that the condensation in a dust free chamber was indeed due to charged ions, Wilson performed an experiment with the supersaturated gas chamber in the presence of a strong electric field and found that the amount of condensation was reduced, implying that the electric field had removed the ions and therefore the nucleation sites [22].

In 1911 using the knowledge gained by him and his peers, Wilson developed his “cloud chamber technique” [23] where he was able to photograph tracks left by radiation in a volume of air that was super saturated. The radiation would leave in its wake a trail of ions that would then become nucleation sites for condensation in the gas. The Wilson cloud chamber allowed physicists to visualize the interactions of various radiations that had been discovered only ten years prior, and to almost directly see the world of subatomic particles. Wilson shared the Nobel prize in physics in 1927 for the development of his cloud chamber.

Armed with Wilson’s cloud chamber and more advanced particle detection methods, namely the coincidence circuitry, physicists were ready to uncover the secrets of subatomic particle physics through studying cosmic rays.

1.2.2. THE BEGINNINGS OF THE PARTICLE ZOO. Physicists began to couple the Geiger-Muller counters to cloud chambers such that when the counter registered a particle the

chamber would quickly expand the gas and subsequently take a photograph of the tracks left by the condensation. Implementation of the cloud chamber in the photographing of tracks left by cosmic rays was pioneered by Skobeltzyn [24]. He placed the chambers in magnetic fields that caused the tracks to bend if the particle was charged, and the curvature allowed for the determination of the momentum.

Soon after, other groups began to utilize and build upon Skobeltzyn's methods. Lead plates were placed in the cloud chambers in order to affect the momentum of the particles so to distinguish their direction of travel. Quickly following the seemingly mundane addition of the lead plate physicists noticed that there were almost equal numbers of negatively and positively charged particles traversing the chambers. To that end, Anderson captured a photo of a particle crossing a plate that was positively charged and was determined to have the same mass as an electron, which he called the positive electron, or positron [25]. Figure 1.2 shows the cloud chamber photograph of Anderson's discovery of the positron. For

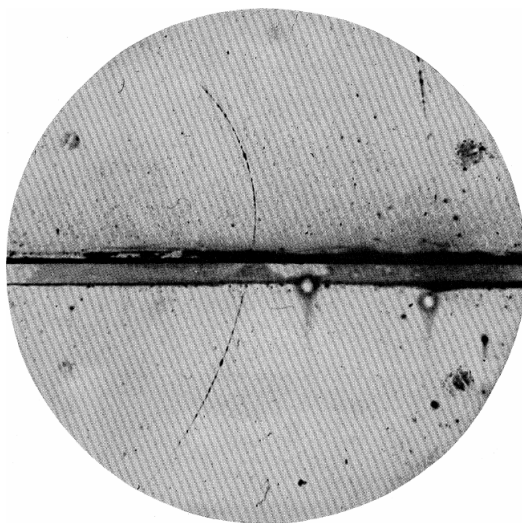


FIGURE 1.2. Cloud chamber photograph of a positron entering the chamber from below, and then losing momentum to the lead plate based on the decrease in the radius of curvature in the track above the plate. The direction of curvature in the track indicates the charge of the particle based on the presence of a magnetic field. Taken from [25].

the discovery of the positron and for the discovery of cosmic rays, which allowed for the new fundamental physics to be uncovered, Anderson and Hess shared the Nobel prize in physics in 1936.

The implications of the positron were far reaching as it was the first antimatter particle to be discovered. Eight years prior, Dirac had theorized that there should exist particles that satisfy the negative energy state solutions to the wave equation in quantum mechanics [26], and the positron did just that for the first generation of spin 1/2 leptons.

The first particle belonging to the second generation of leptons was also discovered using cosmic rays. This time Anderson and Neddermeyer, Street and Stevenson [27, 28] had discovered a particle with a mass between the known electron and proton masses and had a negative charge. The particle, later called a muon, was the highly ionizing particle mainly being seen in detectors at sea level. The muon was the ghostly particle that could traverse hundreds of meters of matter without being stopped was at the time thought to be the mediator of the strong nuclear force theorized by Yukawa [29].

Following World War II detection methods had improved further and photographic emulsion techniques were introduced. It was the latter that allowed physicists to discover the first meson, the pion, after placing their detectors high in the Pyrenees mountains [30]. Rochester and Butler continued the search for new particles using cloud chamber photography, and in 1947 after 5000 photographs they found evidence for a new type of unstable elementary particle, the kaon [31]. The properties of these new particles could not be studied in detail until after the development of particle accelerators in the 1950s, but cosmic rays had opened the door to the bountiful particle zoo physicists relished during the later half of the twentieth century.

1.2.3. AIR SHOWERS AND VERY HIGH ENERGIES. Evidence for particle showers induced by cosmic rays was documented in the 1930s by physicists with the plethora of cloud chamber photographs they had collected. An example of a small shower photographed by Blackett and Occhialini is shown in figure 1.3, notice the particles bending in both directions due to the presence of the magnetic field, implying the presence of both positively and negatively charged particles.

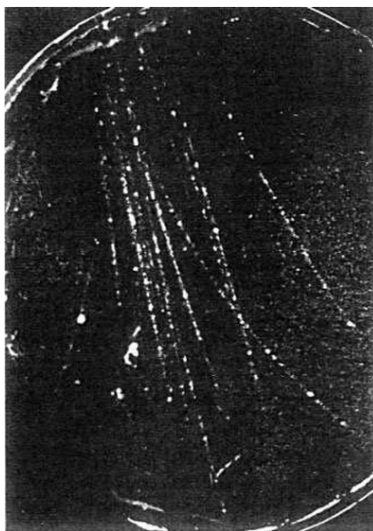


FIGURE 1.3. A cloud chamber photo from [32] showing a small shower of particles that are a part of an atmospheric air shower induced by a cosmic ray. The photo shows the presence of both negatively and positively charged particles based on the directions of the tracks in the magnetic field.

In the late 1930s Auger and others deduced from their coincidence measurements using the Geiger-Muller counters that in order for there to be coincidences between detectors placed far apart, cosmic rays must be inducing large showers of particles in the atmosphere [33]. Using two particle counters and a coincidence algorithm that had a resolving power of $1 \mu\text{s}$, Auger made a measurement of the number of coincidences per hour as a function of separation distance between the counters as shown in figure 1.4, and coincidences were found up to distances of 300 m. The experiment showed disagreement with current air shower theory

as proposed by Euler that expected a decrease to zero coincidence at more than 20 m, the dashed line in figure 1.4 represents this expectation.

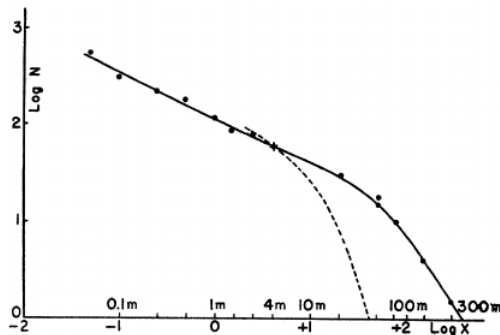


FIGURE 1.4. The main result from [33] where the data are the number of coincidences per hour in two Geiger-Muller counters as a function of distance between the two tubes. The plot is shown on a log scale with a solid line as a fit to the data and the dashed line is the expectation from theory given by Euler. The number of coincidences decrease with distance, but do not become zero, suggesting the presence of large showers of particles initiated by cosmic rays in the atmosphere.

Based on their measurements with the counters, Auger and his collaborators were able to estimate the density of particles between 10 to 100 per square meter, and using the lower end of this estimate along with the surface area bounded by their detectors, about 10^5 m^2 , they derived roughly 10^6 particles present in large showers [33]. With the estimate of a million particles present in the lower atmosphere, a quick calculation of the total energy contained in the air shower can be performed with the assumption that each particle has an energy roughly equivalent with the critical energy of air, or the energy at which ionization and bremsstrahlung rates are equal, 10^8 eV ; leading to an energy of 10^{14} eV contained in a shower. An additional factor of ten is then applied to account for energy lost due to atmospheric absorption so that the primary particle that initiated the shower had an energy of $\sim 10^{15} \text{ eV}$ [33].

With the above energy, and if the primary particle is a proton, then the velocity of the cosmic ray is given by (1.1).

$$E = \gamma m_p c^2 \Rightarrow \frac{v}{c} = \sqrt{1 - \left(\frac{m_p c^2}{E}\right)^2} \Rightarrow v \approx c \left(1 - \frac{1}{2} \left(\frac{m_p c^2}{E}\right)^2\right) = 0.9999999999999996c \quad (1.1)$$

These energies imply that cosmic rays have the highest kinetic energy for massive subatomic particles in the known universe.

1.3. CURRENT UNDERSTANDING OF COSMIC RAYS

After World War II the development of particle accelerators, namely the Cosmotron at Brookhaven National Laboratory and the Bevatron at Berkeley, allowed for laboratory testing of early particle physics theories via accelerating protons to sufficient energies. These machines became the poster children of particle physics, whereas cosmic ray experiments changed their focus from fundamental particle physics to the physics of the ubiquitous high energy cosmic particles.

The mysteries surrounding cosmic rays were, and still are, trivially stated: What is their origin? How are they accelerated to such tremendous energies? What is their composition?

1.3.1. THE EXTENSIVE AIR SHOWER (EAS). An EAS is initiated when a cosmic ray interacts with a nucleus in the upper atmosphere of Earth; depending on the composition of the cosmic ray, the EAS it generates will take on different characteristics. Purely electromagnetic cascades are produced if the incident cosmic ray is a high-energy gamma ray with energies measured up to 10^{17} eV [34], and these are studied in great detail in references [35, 36].

The phenomenology introduced by Heitler [37] describing electromagnetic cascades in the atmosphere is instructive in understanding the development of an EAS. Showers initiated

by a photon undergo repeated two-body splittings such that after n splittings there are 2^n particles in the shower. Once energies of the individual particles, namely the e^\pm pairs, drops below a critical energy value, E_c^γ , where the collision energy losses exceed the radiative energy losses, particle production ceases. The air shower will reach a maximum size when all of the particles reach this critical energy, so an EAS initiated by a photon with an energy E_0 will have a maximum number of particles, N_{max} , when (1.2) is satisfied.

$$E_0 = E_c^\gamma \times N_{max} \quad (1.2)$$

The location in the atmosphere where the shower maximum occurs is a useful quantity, and it is measured in terms of atmospheric depth, where only the density of the atmosphere is important. Atmospheric depth is given in units of g/cm^2 where a path integral of the atmospheric density along the path length of the shower gives the amount of the atmosphere the EAS has traversed. Using this formulation of atmospheric depth, showers with various zenith and azimuthal angles are treated equally and are only parameterized in terms of the amount of atmosphere they plow through. Parameterizing atmospheric depth in g/cm^2 also takes into account the density variation of the atmosphere, where the first sixty kilometers of

$$X_{max}^\gamma = \lambda \ln \left(\frac{E_0}{E_c^\gamma} \right) \quad (1.3)$$

the atmosphere only contribute a $200 g/cm^2$. The depth at which the shower reaches its maximum size, labeled X_{max}^γ , is given by (1.3), where λ is the radiation length for a given medium, the atmosphere in this case.

How X_{max} changes as a function of energy is defined as the elongation rate, which is another crucial quantity used in describing EAS development and discerning cosmic ray measurements.

If the EAS is initiated by a nucleon or a nucleus then the meson interaction channels are available, where in the first interactions pions along with other particles are produced. The neutral pions decay to photons, generating electromagnetic cascades, and the charged pions continue to interact, or decay, until they fall below a critical energy, E_c^π , and subsequently all decay into muons and neutrinos. There are now three components to the EAS if it is initiated by a nuclear primary, the electromagnetic due to the neutral mesons decaying into photons, the muonic due to the decay of the charged mesons, and the hadronic due

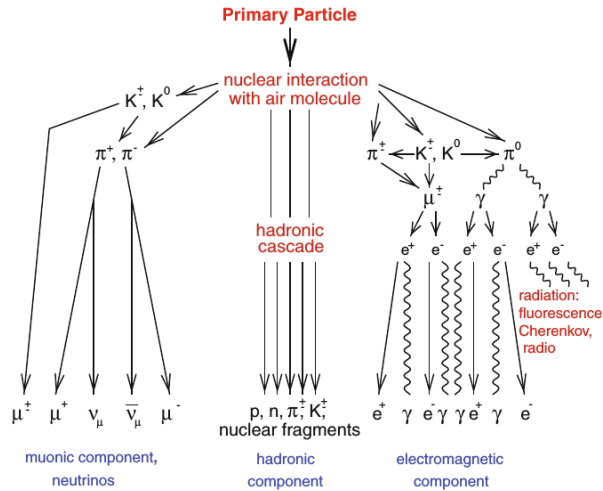


FIGURE 1.5. Schematic showing the three components of an EAS that build simultaneously when initiated by a nuclear primary, from [38].

to the interaction of the charged mesons; these components build simultaneously; figure 1.5 schematically shows these three EAS components.

A detailed treatment of EAS development performed via Monte Carlo methods can be found in [39], but the results presented in [40] illustrate essential relationships for primary energy, E_0^N , and depth of maximum, X_{max}^N for nuclear primaries. For a proton primary with

energy E_0 the first interaction will produce neutral and charged pions, and assuming the neutral pions immediately decay into photons and produce electromagnetic cascades there will be $N_{\pi^\pm}^n$ charged pions with $(2/3)^n \times E_0$ total energy after n interaction lengths in the atmosphere, where the other $(1/3)^n \times E_0$ has gone into the neutral pions. The energy of the primary proton is then divided into two parts shown in (1.4), as all of the neutral pions have initiated electromagnetic showers, and the hadronic cascade has converted all of the charged pions, N_{π^\pm} , to muons, N_μ , through decay.

$$E_0^P = E_c^\gamma \times N_{max} + E_c^\pi \times N_\mu \quad (1.4)$$

Akin to the purely electromagnetic EAS, the depth of shower maximum for a nuclear primary is where the maximum number of photons and electrons occur in the shower development, but now this component of the shower is initiated only by the neutral pions with $(1/3) \times E_0$. X_{max}^P is obtained similar to (1.3) for an electromagnetic shower, but with an energy of $E_0/(3N_{\pi^\pm})$,

$$X_{max}^P = X_0 + \lambda \ln \left(\frac{E_0}{3N_{\pi^\pm} E_c^\gamma} \right) \quad (1.5)$$

where $X_0 = \lambda_p \ln(2)$ is the first interaction depth for the primary proton based on its characteristic interaction length λ_p estimated from the inelastic proton-air cross section [39]. Now using (1.3) for showers initiated by a photon, the above expression (1.5) can be rewritten as follows:

$$X_{max}^P = X_0 + X_{max}^\gamma - \lambda \ln(3N_{\pi^\pm}) \quad (1.6)$$

showing that for proton initiated showers X_{max} is in general shallower in the atmosphere due to the increased multiplicity of hadronic interactions.

Using similar arguments as found in references [41, 42] an EAS initiated by a nucleus can be understood using the superposition model, where a nucleus with an atomic number A and energy E_0^A is modeled as a sum of A proton showers each with initial energy E_0^A/A . This model gives an expression that relates the depth of maximum of this nuclear initiated EAS the atomic number in (1.7).

$$X_{max}^A = X_{max}^P - \lambda \ln(A) \quad (1.7)$$

The variance in a distribution of X_{max} measurements, $\text{RMS}(X_{max})$, of EAS is only influenced by the shower-to-shower fluctuations and decreases with an increasing atomic mass based on the superposition model, thereby making this parameter a powerful observable related to primary composition.

1.3.2. GLIMPSES OF COMPOSITION. Shortly following Auger’s air shower discovery and with the advent of better coincidence methodologies and detector technologies, physicists began to explore the question of the composition of the cosmic particles incident on the atmosphere. Schein arranged a set of particle counters and lead bricks such that if the primary particles were electrons they would initiate electromagnetic showers in the lead bricks and the counters placed to the sides of the bricks would trigger, whereas if the cosmic rays were protons there would not be an accompanying shower produced in the lead. From this work he deduced that for energies less than 10^{12} eV the primary cosmic particles are protons [43].

In 1948 photographic emulsions with silver halide grains were flown to altitudes exceeding 94,000 feet where the primary cosmic ray particles could collide with the heavy silver atoms and expose the film due to the ionization. The silver doped emulsions provided data that

showed a component of the cosmic ray composition were completely ionized nuclei with Z ranging from 20 to 30, and Brandt et al. observed the obliteration of a silver nucleus by a primary with $6 \leq Z \leq 8$ and an energy greater than 3 GeV [44].

These early experiments with cosmic ray composition showed that their makeup was the same as the local universe, from protons to iron nuclei, and that the composition of the highest energy cosmic rays was an amalgam of these nuclei when it had previously been assumed to be dominated by protons.

1.3.3. GROUND ARRAYS. With the success of Auger's work in discovering the phenomena of the air shower the emergence of more sophisticated arrays of particle detectors at ground level began in the 1940s. Ground arrays make indirect measurements about the primary particles striking the top of the atmosphere by measuring the EAS at the ground, or at high elevations.

Detailed work done by Williams [45] using four fast ionization chambers investigated the structure of air showers at elevations between 3000 m and 4000 m. By placing his chambers in four distinct arrangements, he was able to map out the angular distribution, and test the cascade theory [46], proposed years earlier, with twenty-seven events with energies greater than 10^{16} eV. Williams empirically showed that there is a decrease in coincidence with an increase in distance between his detectors that followed a simple power law, just as Auger had also found, and that multiple coulomb scattering was responsible for this lateral spread in air shower particles.

Further study of the structure of air showers reaching sea level was performed by Bassi et al. [47] using liquid scintillators with a lower limit of 5 ns on the ability to measure the delay in the air shower particles with respect to one another. Given their high time resolution, Bassi's group were able to determine several parameters for air showers consisting

of 10^5 to 10^6 particles, including the radius of curvature, the thickness of the shower disk, and the average zenith angle of the shower axis. With these measurements and others, physicists began to piece together a picture of the physics involved in air showers. Air showers were qualitatively understood from the primary interaction with an air molecule to the production of the electromagnetic cascade via the decay or interaction of neutral pions, and the production of muons via the charged pions.

During the 1960s pioneering work was performed by the MIT air shower program [48], which was a succession of ground-based particle detector arrays first at the Agassiz Astronomical Station of Harvard University [49], and then at Volcano Ranch in New Mexico [50]. The Agassiz experiment was the first iteration of the program where they developed detectors made of plastic scintillator coupled to a five inch photomultiplier tube. The fifteen detectors were arranged in interleaved pentagons, where the final one enclosed an area of 460 m. Later, using the same general technique, nineteen similar detectors were placed near Albuquerque at Volcano Ranch on a triangular grid covering an area of 12 km². In 1962 Volcano Ranch recorded an air shower with more than 5×10^{10} particles, which corresponded to a primary particle with an energy of at least 1×10^{20} eV.

The early ground arrays also looked into the arrival directions of the incident primary particle by using the relative timing within the detectors. Innovative work done by Clark in 1961 [51] showed no evidence for anisotropy within the arrival directions of cosmic rays with energies between 10^{16} eV to 10^{18} eV.

Not until work by Krasilnikov in 1974 [52] was there evidence of anisotropy, and this kick-started an argument over the origin of cosmic rays, either from galactic or extragalactic sources, and the implications of the location of these sources on the composition of cosmic

rays. The only measurement available to these early ground arrays that gave information on composition and origin was the energy spectrum.

1.3.4. PARTICLE FLUX AND THE COSMIC RAY ENERGY SPECTRUM. The number of cosmic rays striking a given area on the surface of the earth with a given energy, E , is known as the flux, $J(E)$, and the energy spectrum is how this flux changes as a function of energy. The early ground arrays measured the spectrum of energies of primaries with high enough energies, $E > 10^{14}$ eV, to allow for indirect measurements on the primary cosmic rays through EAS measurements. Balloon flights using electroscopes and photographic plates

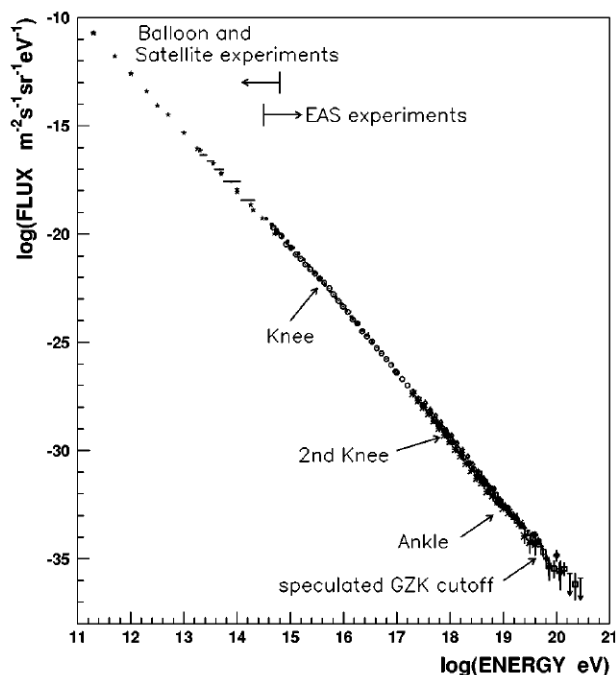


FIGURE 1.6. Energy spectrum, from [56], showing the full measured cosmic ray energy spectrum, energy regions for each direct and EAS measurements, and several spectral features as discussed in the text.

described above in section 1.2 were direct measurements of the cosmic ray flux for energies up to $E \sim 10^{15}$ eV, and much later via space-based detectors such as PAMELA, AMS-02, Fermi, and other satellites [53–55]. Figure 1.6 shows the full energy spectrum of cosmic rays where the flux varies by nearly thirty orders of magnitude and the energy spans over

ten orders of magnitude, and there are several spectral features labeled the figure that will be discussed below. The energy spectrum follows a power law with a spectral index, γ , of ~ 3 , meaning that for every decade in energy, the flux falls off nearly three orders of magnitude. Early ground arrays sought to measure γ for energies up to 10^{18} eV, and find an expression that described the energy spectrum, and in 1961 [51] found a flux satisfying (1.8) with $J_0 = (8.2 \pm 3.1) \times 10^{-11} \text{ cm}^{-2} \text{ s}^{-1} \text{ sr}^{-1}$ and $\gamma = -2.17 \pm 0.1$.

$$J(E) = J_0(10^{15}/E)^\gamma \text{ cm}^{-2} \text{ s}^{-1} \text{ sr}^{-1} \quad (1.8)$$

As mentioned in section 1.3.3, measurement of the cosmic ray energy spectrum and the spectral index was an early handle on composition and origin. By comparing the measured energy spectrum at earth for a range of energies to theorized spectra from various sources, galactic or extragalactic, with various assumed initial compositions conclusions were made in 1974 and 1975 by [57, 58] that protons from extragalactic sources dominated the energy spectrum for 10^{17} eV and above.

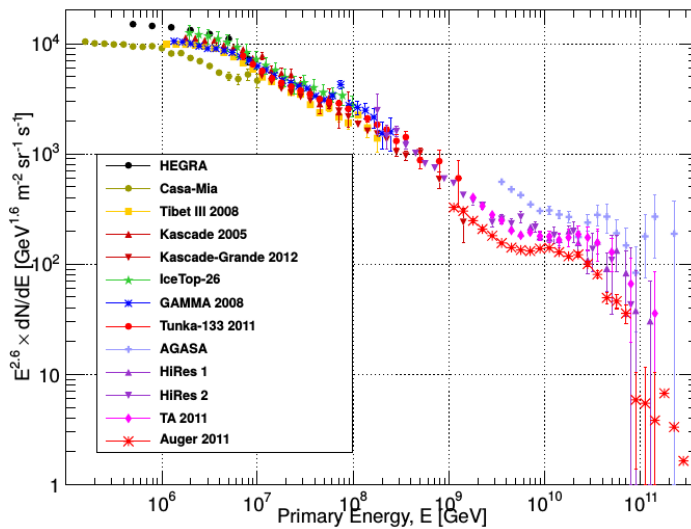


FIGURE 1.7. Energy spectrum from 10^5 GeV to highest energies where the flux has been multiplied by $E^{2.6}$ accentuate spectral features. From [59].

Since then the cosmic ray energy spectrum has been measured by a multitude of experiments all of which show a power law and a few spectral features. Figure 1.7 shows numerous measurements of the energy spectrum for energies greater than 10^6 GeV with the flux multiplied by $E^{2.6}$ to highlight the spectral features. The spectral features known as the “knee” between 10^{15} eV and 10^{16} eV, and the “ankle” starting at $\sim 10^{18}$ eV, represent changes in the slope of the spectrum, either a hardening or softening of the spectral index respectively. The Greisen-Zatespin-Kuzmin (GZK) cutoff at the highest energies will be discussed in section 1.3.6.

1.3.5. ENERGY SPECTRUM AND ACCELERATION MECHANISM HYPOTHESES. The origin and acceleration mechanism(s) of high energy cosmic rays are still not known precisely, but clues to these mysteries are contained within the spectral features mentioned above and in the energy spectrum itself.

As stated above, the cosmic ray energy spectrum has been measured to follow a power law with spectral index ~ 3 for nearly thirty orders of magnitude in energy, and this seems natural since relationships following power laws occur in nature quite often, see section 2 of [60] for interesting examples, ranging from the diameters of craters on the moon to the frequency with which words are used in novels. There are several ways to generate power law distributions, and one that is very attractive to physical systems is the so-called mechanism of critical phenomena, or where a given system is only governed by an overall length-scale [60]. It was fitting then for Fermi to theorize an acceleration mechanism based primarily around the interaction length of protons in interstellar space [61]. In Fermi’s theory charged particles would gain kinetic energy by interacting with magnetic fields within dilute gas clouds, and would gain considerably more kinetic energy in the presence of rapidly varying magnetic fields such as around supernovae remnants (SNRs) where $E_{max} \sim (1-3) \times 10^{15}$ eV for protons [62].

The Fermi acceleration method is able to explain the overall power law of the energy spectrum, and laid the foundation for what is called the “standard model” of galactic cosmic rays, which is able to shed light on the knee feature in the spectrum. The above maximum energy attainable through galactic SNRs is quoted for protons, but this energy is higher by a factor of Z for nuclei with charge Z [62]. A leading explanation for the steepening of the energy spectrum known as the knee is the cutoff of the SNR acceleration for increasing masses of particles [63]. Due to magnetic confinement within the SNR, particles with larger masses and charges leak out of the acceleration region as their energy increases, such that the SNR mechanism cuts out for all species around $26 \times E_{max}$ or $(5-8) \times 10^{16}$ eV, where 26 is the charge for iron nuclei. Re-acceleration models explaining how galactic sources can achieve energies above the iron cutoff to $\sim 10^{17}$ eV are proposed in [64].

Purely based on the magnetic confinement of the cosmic ray particles, with charge Z , within a region of magnetic field, B , as described by the Fermi acceleration method, one can draw conclusions about the possible acceleration sites based on measured astrophysical phenomena. By requiring that the size of the Larmor radius, r_L , not exceed the size of the acceleration region, and including the characteristic velocity of the magnetic scattering centers, βc , one arrives at the “Hillas criterion” (1.9), as argued in [65].

$$E_{max} \sim \beta c Z B r_L \tag{1.9}$$

From the above criterion the Hillas plot in figure 1.8 shows various possible astrophysical sites of cosmic ray particle acceleration. One can see from the plot that very few sites are capable of producing cosmic rays with measured energies above 10^{20} eV, including active galaxies, GRBs, and neutron stars. Other than neutron stars, the other possible sources outlined by the Hillas criterion are extragalactic and are the leading hypothesis explaining

the ankle feature of the energy spectrum [66–68]. The transition from a spectrum of galactic sources cutting out to a spectrum of extragalactic sources explains the slight increase in the spectral index above $10^{18.5}$ eV. The Hillas criterion placed limits on types of phenomena capable of accelerating cosmic rays to such high energies, and with a previous cosmological discovery there was now a limit to how far away these sources could be.

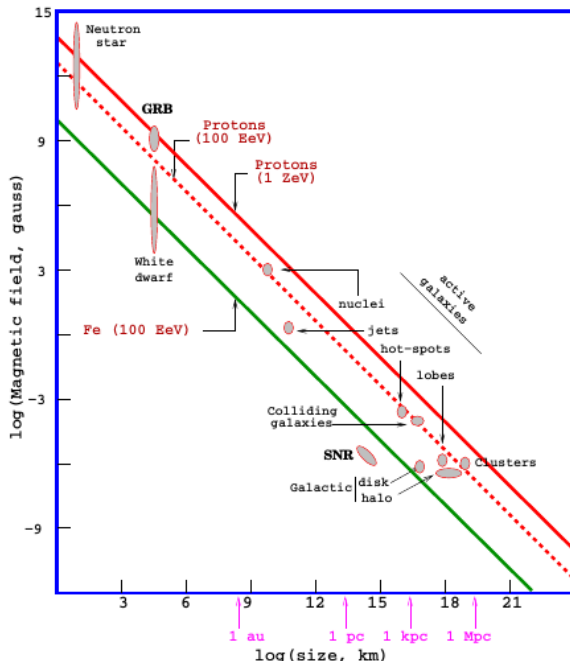


FIGURE 1.8. A Hillas plot showing the size and magnetic field strength for possible cosmic ray acceleration sites, where objects below the diagonal lines cannot accelerate protons above 10^{21} eV, 10^{20} eV, and iron nuclei above 10^{20} eV, respectively, with $\beta=1$. Taken from [69].

1.3.6. THE COSMIC MICROWAVE BACKGROUND AND ITS IMPLICATIONS. In 1965 Penzias and Wilson serendipitously discovered the Cosmic Microwave Background (CMB) radiation that pervades the universe while attempting to break-in a new radio-telescope at Bell Labs. While trying to account for all backgrounds in the new six meter horn antenna, Penzias and Wilson detected a faint noise at 4080 Mc/s that covered the whole sky and did not emanate from a source; they found it to have a wavelength of ~ 7.35 cm and temperature

3.5±1.0 K [70]. The CMB is effectively a photon gas with a density of ~ 550 photons/cm³ assuming a mean temperature of 3 K.

The year after the discovery of the CMB three physicists, Greisen [71], Zatespin and Kuzmin [72], independently made predictions about the effects this pervading photon gas would have on ultra-high energy cosmic rays. CMB photons have an energy of $\sim 6 \times 10^{-4}$ eV, and for cosmic rays consisting of protons an interaction with the photons due to a delta (Δ^+) resonance will take place as shown in 1.10



where the energy of the proton in the final state has been reduced by nearly 20% [72]. The energy threshold for the proton in this reaction follows from (1.11) where the Lorentz invariants are set equal to each other, the proton mass is neglected in this highly relativistic scenario, and the collision is head-on.

$$(\mathbf{p}_p + \mathbf{p}_\gamma)^2 = \mathbf{p}_\Delta^2$$

$$m_p^2 + 2\vec{p}_p \cdot \vec{p}_\gamma = m_\Delta^2$$

$$\text{Where : } \vec{p}_p \cdot \vec{p}_\gamma \simeq E_p E_\gamma (1 - \cos \theta)$$

$$m_p^2 + 2E_p E_\gamma (1 - \cos \theta) = m_\Delta^2 \quad (1.11)$$

$$\text{Where : } \theta = \pi$$

$$\therefore E_p = \frac{m_\Delta^2 - m_p^2}{4E_\gamma}$$

$$E_p = \frac{(1232 \text{ MeV})^2 - (0.938 \text{ MeV})^2}{4 * 0.6 \text{ meV}} \simeq 5 \times 10^{20} \text{ eV}$$

The mean free path for this interaction is on the order of 4×10^{25} cm, or about 50 million light years [71], thereby effectively putting a limit on how far the sources of ultra-high energy cosmic rays can be. The cutoff in the ultra-high energy proton spectrum is also very sharp as the proton energies approach 10^{20} eV due to the steepness of the Planck distribution; the reduction factor exceeds several hundred for energies $> 2 \times 10^{20}$ eV [71]. The so-called

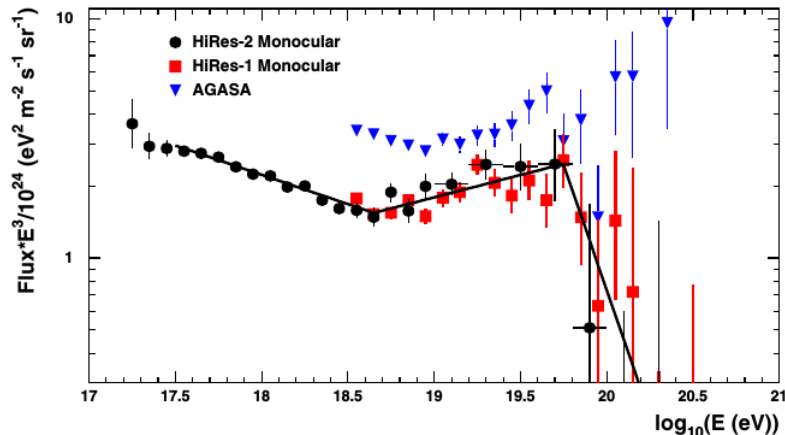


FIGURE 1.9. The energy spectrum as measured with the two detectors in the HiRes experiment, HiRes-I is shown as squares and HiRes-II is shown as circles, where each are the independently reconstructed. The unbroken spectrum extending to highest energies from AGASA is shown as triangles [73]. Taken from [74].

GZK effect also puts limits on cosmic rays consisting of heavy nuclei via photodisintegration, where the threshold for the interaction with CMB photons is 5×10^{18} eV/nucleon [71], and the mean free path is $\sim 2 \times 10^{22}$ cm, or 20,000 light years. Heavy nuclei are therefore confined to regions of space smaller than the size of galaxies. The suppression in the cosmic ray flux at the highest energies predicted by Greisen, Zatespin and Kuzmin, was first observed with 5σ significance by HiRes [74], after previous experiments reported an unbroken spectrum beyond the predicted GZK cutoff [75, 73]. Shown in figure 1.9 is the spectrum measured by HiRes showing the suppression above 6×10^{19} eV as well as the “ankle” region around 4×10^{18} eV. Since the HiRes result other experiments have observed a suppression [76–78].

One of the experiments is the Pierre Auger Observatory, which has the largest dataset on ultra-high energy cosmic rays because it is the largest cosmic ray observatory in the world.

CHAPTER 2

THE PIERRE AUGER OBSERVATORY

The Pierre Auger Observatory is located near Malargüe, Mendoza, Argentina, and is designed to detect extensive air showers (EAS) initiated by cosmic rays with energies greater than 10^{18} eV and to study the origin and nature of these ultra-high-energy particles. At this location in the southern hemisphere the Auger Observatory field of view includes the galactic center and Centaurus A, which is one of the closest radio galaxies to Earth. The observatory began taking data in 2004 while it was under construction and has been fully

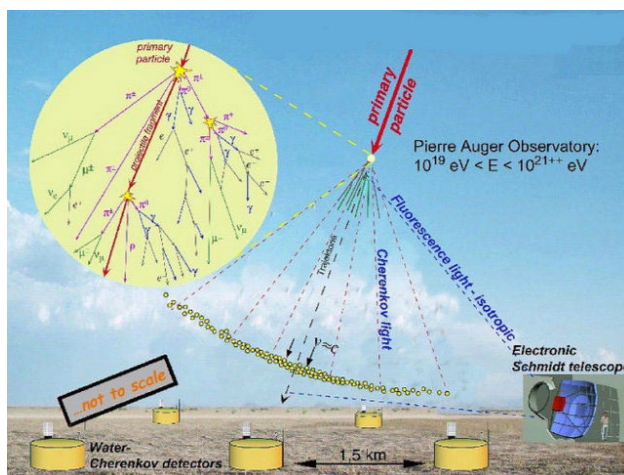


FIGURE 2.1. A figure of the Pierre Auger Observatory schematically showing the two detection techniques used by the Observatory to study extensive air showers. Note that it is not to scale, the water tanks are 3.6 m in diameter and 1.85 m in height, the fluorescence detector(s) are located on the periphery of the 3000 km^2 water tank array and do not operate during daytime. Adapted from [79].

operational since 2007. It is a hybrid cosmic ray observatory in that it uses two different complementary techniques to observe EAS. The first measurement technique uses an array of water Cherenkov detectors on the ground that record information from the secondary charged particles reaching ground-level, and the second uses air fluorescence initiated by the EAS as it passes through the atmosphere to study the longitudinal development of the EAS.

These two methods have been used previously [80–85], but the Pierre Auger Observatory is the first to use them in conjunction. Figure 2.1 schematically depicts the two detection techniques the Pierre Auger Observatory uses.

2.1. THE SURFACE DETECTOR

The surface detector (SD) is an array of over 1600 water Cherenkov detectors (WCD) set on a 1.5 km triangular grid covering 3000 km². Each WCD detects the charged particles that reach the ground from an EAS. Covering an area of 3000 km², the Pierre Auger Observatory is the largest cosmic ray observatory in the world and allows for the highest statistics on cosmic rays with energies greater than 10¹⁸ eV. A typical 10¹⁸ eV event will generate an EAS with a shower front covering several square kilometers at the ground, thus hitting several water tanks. Figure 2.2 is a photograph of one of the WCDs, and it shows the various parts of the tank system.

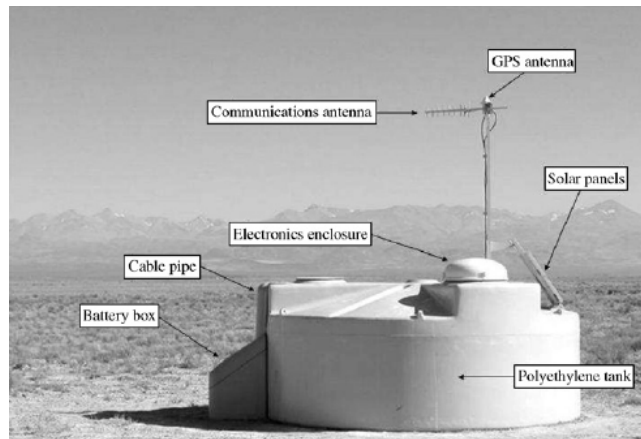


FIGURE 2.2. A photograph of the ~ 2 m tall and 3.6 m diameter water Cherenkov detector used in the field showing the main components of the system [86].

Each tank is 3.6 m in diameter and contains 1.2×10^5 liters of purified water, which equates to 10 m² water surface area with an active height of 1.2 m. The water is housed

inside a reflective liner made of Tyvek inside the tank. The Cherenkov light produced by the charged particles in the water reflects off the liner and is collected by three nine-inch diameter photomultiplier tubes (PMTs) that are symmetrically distributed at a distance of 1.2 m from the center of the tank and face downwards viewing the water through windows of clear polyethylene.

A solar panel provides power for all of the components in the tank system, including the PMTs, and all the electronics for data collection. Each triggered PMT provides signals that are digitized at 40 MHz using 10-bit flash analog to digital converters (FADCs) and have a large enough dynamic range to cover the signals near the shower core, nearly 1000 particles per μs to those far from the core ~ 1 per μs . Each FADC bin corresponds to 25 ns. The electronics package has a GPS antenna that time stamps the recorded events and another antenna communicates the event data to the radio tower located at the closest FD building [87], and the data are then sent to the central data acquisition system (CDAS) located in Malargüe.

Before discussing how the triggering scheme for the SD works, the signal that the WCD reports must be elaborated. The signal unit is defined by the automatic calibration of the detector using the measurement of the average charge collected by a PMT from Cherenkov light produced by a vertical and central through-going muon, Q_{VEM} . The WCD cannot distinguish vertical muons only, but the distribution of light from atmospheric muons has a peak in the charge distribution, Q_{VEM}^{peak} , as well as a peak in the pulse height, I_{VEM}^{peak} , and these are proportional to those produced by vertical through-going muons [88]. This calibration is performed every 60 seconds and is reported with every event to CDAS.

Due to the high rate of atmospheric muons that pass through each WCD, 3 kHz, that are not necessarily from a high-energy EAS, the triggering scheme has a hierarchal form where

at each level this rate is reduced by more and more strict background discrimination [88]. The first level, T1, takes place at each WCD and has two different modes. The first T1 mode is a basic threshold trigger where it looks for a coincidence between the three PMTs of the WCD with a signal greater than $1.75 I_{VEM}^{peak}$, this reduces the rate from 3 kHz to ~ 100 Hz. The second T1 mode is a time-over-threshold (ToT) trigger where PMTs in coincidence must maintain $0.2 I_{VEM}^{peak}$ for 12 bins within a $3 \mu s$ window. The ToT trigger uses the spread in the shower front as a discrimination method and is therefore sensitive to low energy showers that land nearby a WCD or higher energy showers that land further away.

The second level trigger, T2, acts to reduce the rate of events coming from a single WCD to 20 Hz so as to not to overload the communication system of the detector. All of the T1-ToT pass the T2 trigger, whereas T2 sets a higher threshold on the T1 threshold triggers. The third trigger, T3 is based on spatial and temporal combinations of the T2 triggers among neighboring tanks and activates data acquisition from the array. For further details about the fiducial triggering details see reference [86].

The SD array becomes fully efficient, where more than 97% of simulated events result in a trigger of the detector around an energy of 3×10^{18} eV for all shower zenith angles up to 60° . This efficiency is a function of layout of the WCDs and of how the hierarchal triggering is constructed; the SD array was designed to be fully efficient for the highest energy cosmic rays with energies greater than 3×10^{18} eV.

Typically one measures the signal from an EAS as the fall off in signal size as a function of distance from the shower core using an array of WCDs. By using the relative arrival times and the deposited signal in the array the shower core and other geometrical quantities about the shower are determined. The signals from the triggered WCDs are plotted as a function of distance, and the lateral distribution function (LDF) is fitted to these points [89].

From the LDF the signal at a certain distance is used to calculate the energy of the cosmic ray event. For the Pierre Auger Observatory this distance is 1000 m [90], and the signal measured at 1000 m is called $S(1000)$. The energy is then estimated by comparing the amount of signal at 1000 m for a given event with Monte-Carlo data. Using simulations to calibrate the SD energy estimation leads to a strong model dependence, but the use of the fluorescence detector allows for an independent measurement of the energy that is then used to calibrate the SD. It is these two independent measurements of the EAS energy that make the Pierre Auger Observatory such a unique experiment: the calorimetric energy measurement made by the fluorescence detector, described in the next section, is used to calibrate the SD measurement, as shown in figure 2.3, thereby allowing use of the events observed by the SD only with very little model dependence. The work presented in this

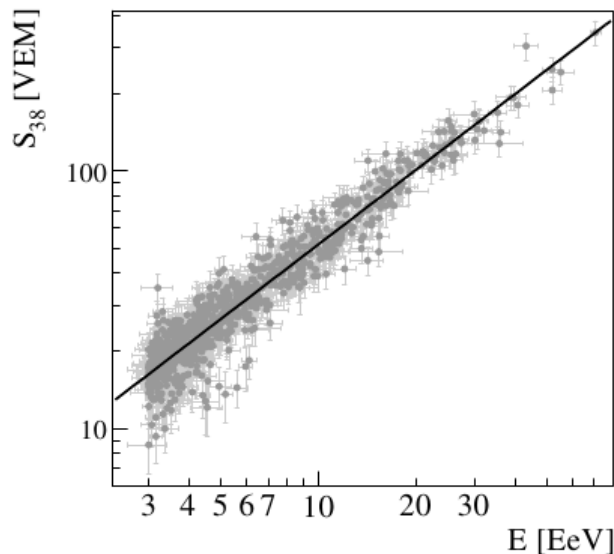


FIGURE 2.3. The correlation between the FD energy and SD energy for 839 events observed by both the SD and FD. $S(38)$ is a normalization of the $S(1000)$ value by the CIC method [91] with a median angle of 38° zenith angle. The solid line is a single power-law fit. Taken from [92].

this thesis deals with the calibration of the fluorescence detectors, and given that the Auger SD

energy scale is calibrated by the fluorescence energy measurement, the fluorescence detector calibration is vitally important.

2.2. THE FLUORESCENCE DETECTOR

The second detector consists of twenty-seven specialized telescopes that overlook the SD and detect the nitrogen fluorescence caused as the EAS traverses the atmosphere. The 27 telescopes are located at five sites, four buildings that are along the perimeter of the SD with six telescopes each, where the six telescopes together cover 180° in azimuth, and one site with three telescopes discussed in section 2.3. The four buildings with six telescopes are named: Los Leones, Los Morados, Loma Amarilla, and Coihueco, see figure 2.4 for their locations within the observatory.

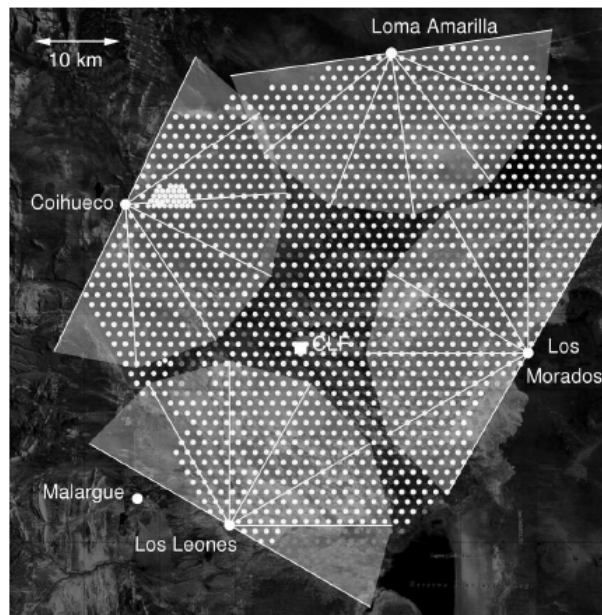
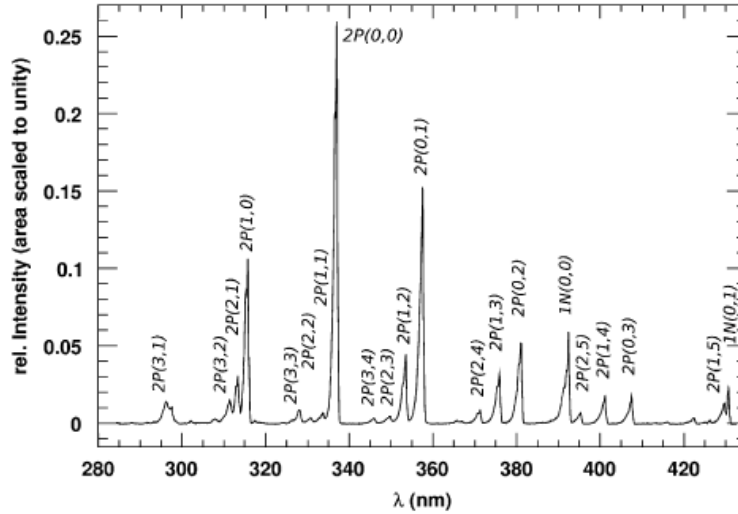
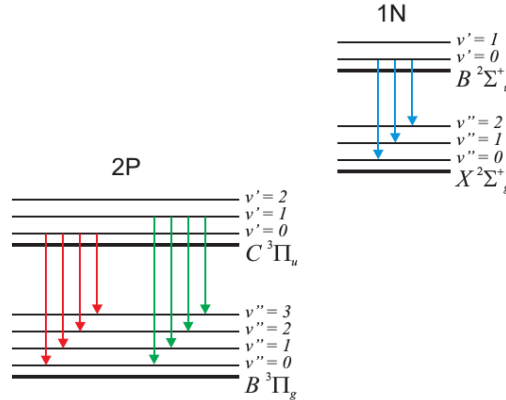


FIGURE 2.4. The FD building sites on the periphery of the SD, which overlook the SD array. Each building has six individual telescopes with a 30° azimuth and $\sim 30^\circ$ in elevation, field of view, represented by the triangular gray regions. The dots are the ~ 1600 water tanks, from [93].

2.2.1. FLUORESCENCE LIGHT DETECTION. As the EAS propagates through the atmosphere the secondary electrons excite the nitrogen molecules, and when the nitrogen relaxes fluorescence light is emitted in the 300-450 nm wavelength range, see figure 2.5a for the complete emission spectrum. The other atmospheric constituents, namely argon, contribute



(A) Nitrogen fluorescence spectrum measured at the Argonne Chemistry Can de Graaff facility at 800hPa and 293K. Labels indicate 21 major transitions. See [98] for details.



(B) A schematic showing the energy states of the 1N and 2P electronic-vibrational band systems of N_2 and N_2^+ , from [97].

FIGURE 2.5. Upper figure is the measured nitrogen fluorescence spectrum, and the lower figure is a band structure for the major peaks in the spectrum.

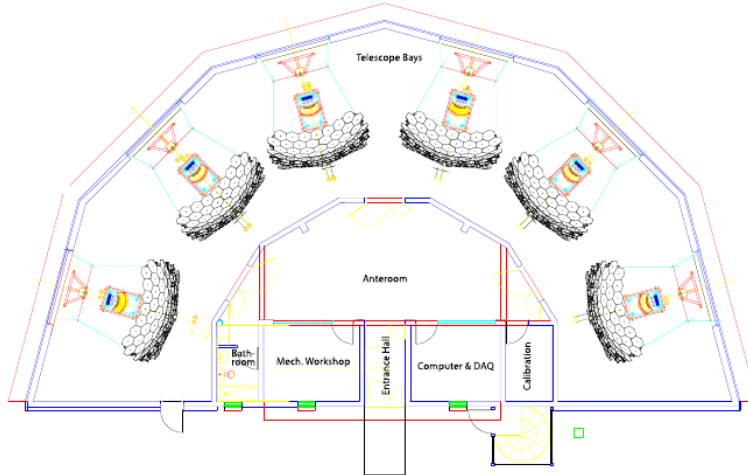
a negligible amount of light at atmospheric pressures [94, 95], and oxygen was also shown to

be negligible [96]. The nitrogen fluorescence is caused by the excitation of the rotational and vibrational modes, which are split into the substructure as shown in figure 2.5b, for details see [97].

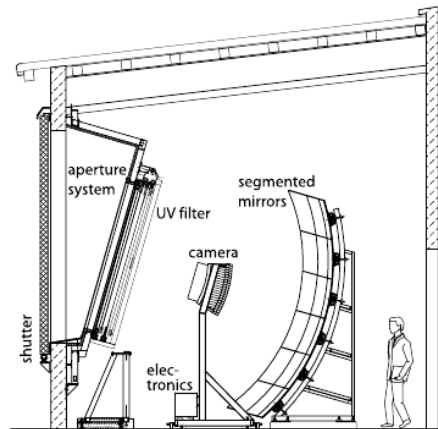
The number of emitted photons is proportional to the energy deposited into the atmosphere by the EAS; the atmosphere acts as a calorimeter for the air showers. The fluorescence detector measures the energy deposited in the atmosphere as a function of atmospheric slant depth X , in g/cm^2 , and this is called the longitudinal development profile dE/dX . Then the integral of the longitudinal profile over the slant depth the shower traversed is the total electromagnetic energy of the cosmic ray, which is about 90% of the total energy [99]. The other 10% of the energy contained in the primary particle is lost to production of high-energy muons, and neutrinos [100]. HiRes and Fly's Eye [83] pioneered this air fluorescence technique, but these experiments only used a fluorescence detector and therefore did not have the high geometrical accuracy the Auger Observatory achieves through hybrid measurements.

2.2.2. THE PIERRE AUGER OBSERVATORY FLUORESCENCE TELESCOPE. The telescopes in the Observatory are a highly specialized light detection system designed to observe the very faint fluorescence light from an EAS over a distance of more than 30 km. Its camera system is similar to the HiRes and Fly's Eye design with an array of PMTs used to detect the light, but the aperture system, building enclosures and electronics are unique to the Pierre Auger Observatory experiment.

Each building houses six telescopes as shown in figure 2.6a, where each telescope bay is isolated by black cloth. The building itself is climate controlled and the bays are kept clean with air filtration and weather sealing. Each telescope bay houses the components to the telescope system: an aperture with a UV filter, a corrector ring, a large segmented mirror and the camera made up of 440 PMTs; this general setup is shown schematically in figure



(A) Schematic layout of one of the building housing six fluorescence telescopes



(B) A schematic of an individual fluorescence telescope with its components labeled. Each building has six of these setups. The person is just for scale.

FIGURE 2.6. A schematic of the buildings that house the fluorescence telescopes on the top and the telescope on the bottom. Both taken from [93].

2.6b. The layout of the telescope is a modified Schmidt-Cassegrain design. The UV filter was manufactured by Schott glass [101] and is of the BK7 variety that has a transmission range of ~ 285 nm up to ~ 440 nm, which bounds the nitrogen fluorescence spectrum, see figure 2.7 for a measurement of its transmission as a function of wavelength.

The upper and lower edges of the transmission of the UV filter severely affect the multi-wavelength response of the whole telescope; any unknown degradation leads to an over

estimation of the cosmic ray energy as will be explained in Chapter 4. Past the filter there is a corrector ring that alleviates spherical aberration within the Schmidt geometry and

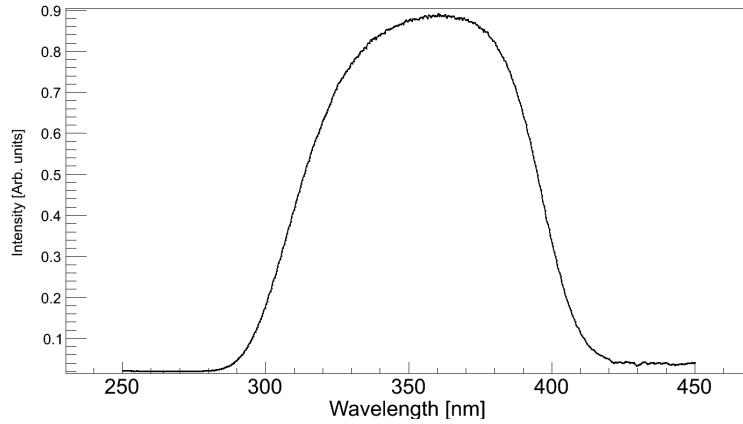


FIGURE 2.7. Measurement of the transmission as a function of wavelength of the UV filter made at CSU, where the transmission is in arbitrary units.

enhances the aperture of the telescope by a factor of ~ 2 . The large, 13 m^2 , mirror is made of segments to keep its weight and cost down. Two segmentation patterns are used within the 27 telescopes, shown in figure 2.8, but both maintain the same radius of curvature of 3400 mm, however there are two types of material used as the reflective surface. The twelve

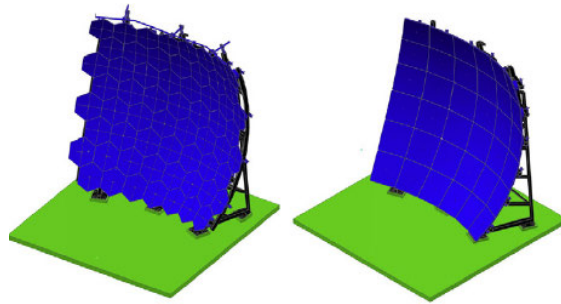


FIGURE 2.8. The spherical mirror used in the telescopes, showing the different methods by which the large area is segmented, from [93].

telescopes at the Los Leones and Los Morados FD buildings use a mirror with a sheet of 2 mm AlMgSiO_5 as the reflecting surface and twelve telescopes at the Coihueco and Loma Amarilla buildings use a borosilicate PYREX glass with a polished Al layer as the reflecting surface with a layer of deposited SiO_2 . Two collaborating countries supplied the mirrors,

which led to the different types for the different FD telescopes. The differences in material used for reflection may affect the multi-wavelength response between these buildings. Both types of mirrors are highly reflective, more than 90%, but over time dust and other debris has collected onto them, even with periodic cleaning of a few times a year, and affected their reflectivity, possibly as a function of wavelength.

2.2.3. THE FD CAMERA. The mirror focuses the fluorescence light onto a focal surface that contains the camera body, see figure 2.9, where an array of 440 hexagonal Photonis XP3062 PMTs are housed. The 22 row \times 20 column matrix of PMTs corresponds to a field of view of 30° in azimuth and 28.1° in elevation, and each PMT or pixel has an angular size of 1.5° , for details see [102]. As can be seen in figure 2.9 there is a significant amount of

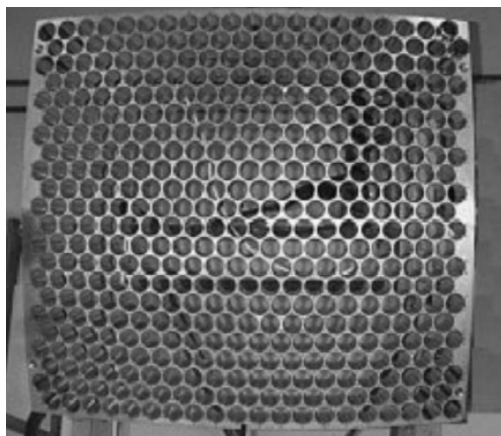
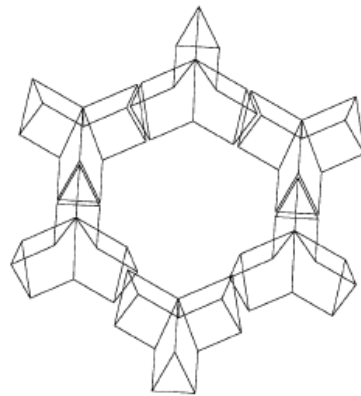


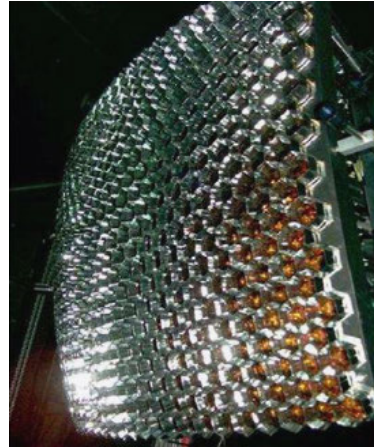
FIGURE 2.9. A picture of the camera body without any PMTs. Made from a single piece of aluminum with precision drilled 40 mm holes for each PMT. Taken from [102].

dead space between the active pixels; to improve the light collection of the pixels, they are aided by light collectors. These light collectors are similar to Winston cones, but match the geometry of the hexagonal PMTs and therefore are a combination of six Mercedes stars as shown in 2.10a. With the Mercedes in place Monte-Carlo ray tracing shows that the light collection efficiency of the camera is 94%, and without the light collectors that efficiency

drops to 70% [102]. Due to the camera being positioned on a spherical surface to match the



(A) The six Mercedes stars that surround the hexagonal PMT in the center, which define the pixel area in the camera.



(B) A fully instrumented camera with the PMTs and the aluminized mylar Mercedes in place around the PMTs.

FIGURE 2.10. A schematic of the six Mercedes stars that define the pixel of the camera on the left and a picture of an actual camera with the PMTs and Mercedes mounted in the camera body, [102].

focal surface of the telescope, the pixels do not maintain a regular hexagonal area across the camera, their effective area varies over the focal surface. The pixels in the center column of the camera have the largest effective area and as one steps out to either edge, this area decreases by 3.5% and must be taken into account in the absolute calibration as will be discussed in Chapter 3.

2.2.4. THE PMT AND TRIGGERING SCHEMES. The PMTs are hexagonal and have a bialkaline photocathode that measures 40 mm side to side. This photocathode has a typical bialkaline quantum efficiency (QE) with a peak in the high UV and a tail that extends above 500 nm, the whole curve is shown in figure 2.11. The PMT QE in the 300 nm to 400 nm range is the largest contributing factor to the multi-wavelength response of the telescope, and as the PMTs age this efficiency changes and affects the whole experiment if it is not taken

into account. The high voltages for the PMTs are set individually as part of a calibration procedure and are ~ 900 V, resulting in a gain of $\sim 5 \times 10^4$.

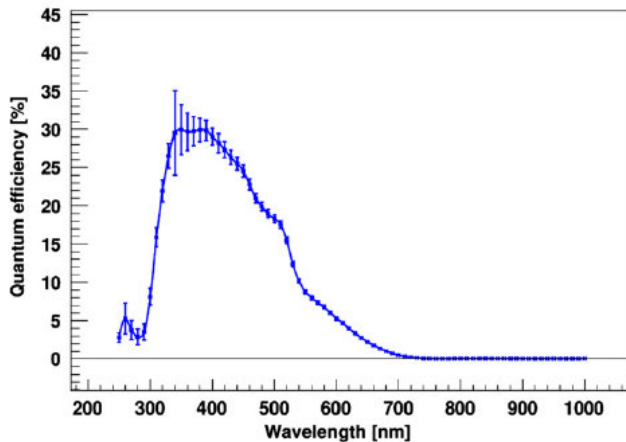


FIGURE 2.11. The measured quantum efficiency of the Photonis XP3062 FD PMT, taken from [93].

The triggering scheme for the FD is divided into three levels. The First Level Trigger (FLT) processes data from a column of 22 pixels using a 12-bit ADC, which digitizes the signal at a rate of 10 MHz that corresponds to a 100 ns time bin. A Field Programmable Gate Array (FPGA) generates the FLT when the integrated ADC signal passes a threshold, where this threshold is dynamically adjusted to maintain a pixel trigger rate of 100 Hz. The FLT also counts the number of pixel triggers generated for a given 22 pixel column across the whole camera within the 100 ns window; these multiplicities are passed to the Second Level Trigger (SLT).

The SLT algorithm searches the FLT's for straight track segments of at least 5 pixels. Straight segments are defined by the patterns shown in figure 2.12 or reflections or rotations of these. Permutations of these patterns result in 108 different combinations, and across the 20×22 camera matrix this results in 37163 combinations in total. In order to deal with such a large number of patterns, the SLT scans 20×5 subsets of the full camera every 100 ns.

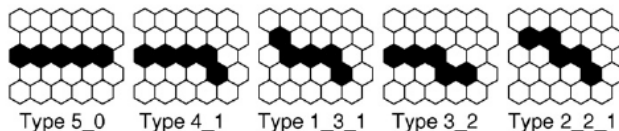


FIGURE 2.12. The fundamental types of tracks the Second Level Trigger algorithm looks for in the First Level Trigger multiplicities [93].

A trigger is generated if during a $1 \mu\text{s}$ full scan of the camera, one of the 108 patterns is detected.

Finally, the Third Level Trigger, TLT, is a software algorithm designed to reject noisy events that pass the lower level triggers, specifically events caused by lightning, muon impacts with the camera and randomly triggered pixels. Events in each telescope that pass the TLT are examined by an event builder program on a local computer and events in coincidence across adjacent telescopes are merged. In addition to the events being merged, the computer also sends a hybrid trigger called a T3 to the CDAS in Malargüe that serves as an external trigger for the SD. The main purpose of the hybrid trigger is to collect SD data for low energy, less than 3×10^{18} eV, events that would not normally trigger the SD but will trigger the FD due to their close proximity to the telescope, at less than 20 km. Usually these showers only will trigger one or two water tanks, but this along with the FD information is enough information to pinpoint the geometry of the shower and led to a high-quality event reconstruction, with a core resolution of 50 m, an angular resolution of 0.6° , and a resolution on depth of shower maximum, X_{max} , to less than 20 g/cm^2 [103].

2.2.5. MONITORING AND CALIBRATION. The FD is a very sensitive instrument that can only be operated during moonless nights with low wind, and reliable data can only be recorded when the atmosphere is relatively clear. These prerequisites for operation mean that a robust monitoring system must be in place in order to assure quality data-taking and

keep the environment from harming the detector, and the atmosphere must be monitored and calibrated.

The monitoring system keeps track of the environment in and around the FD buildings including wind, light, and precipitation [104]. Safety measures are in place to prevent damage to the telescope. If any of these environmental factors exceed certain limits, i.e. wind speed, any light in the aperture or telescope bays or any precipitation, operation of the FD ceases and the shifters are immediately notified. The bay doors on the outside of the building quickly and automatically shut and the high voltages on the PMTs are turned off. Temperature is also monitored in and around the FD buildings. While the temperature outside is important to the atmospheric calibration, the temperature inside the building is critical for the stability of the cameras because of the strong temperature sensitivity of PMTs. The typical anode sensitivity for PMTs similar to those used in the FD camera is -0.4% per °C [105]. All of the monitoring data are stored in MySQL databases and are available to shifters on a real-time basis via a web interface.

In addition to the nightly environmental monitoring there are also calibrations performed on the FD telescopes, and atmospheric calibrations used to characterize the scattering of the fluorescence light. The calibrations of the FD are broken into three types, absolute [107], multi-wavelength [108], and relative [106]. Both the absolute and multi-wavelength use a large diameter light source, affectionately named the “drum” due to its appearance, to fill the entire telescope aperture and perform an end-to-end measurement of all detector components. Typically the absolute calibration is performed once a year due to the logistics of hauling the drum to all telescopes and the precise work needed to calibrate the drum itself, and the multi-wavelength calibration is performed every few years. Chapter 3 will discuss the FD and drum calibration methods in detail. The hardware dealing with the

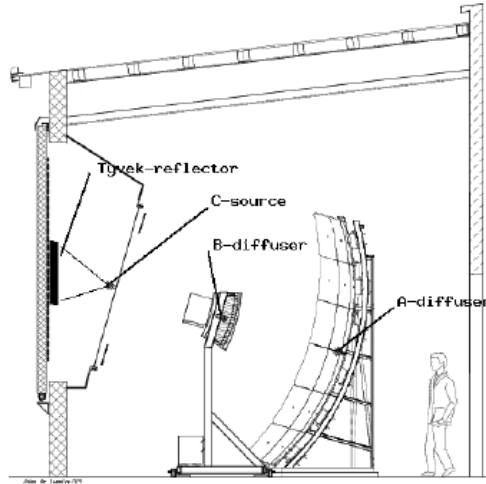


FIGURE 2.13. A schematic showing the positions of the relative calibration light sources. The Cal A source is located at the center of the mirror, the B source is mounted on the camera and shines on the mirror into the camera, and the C source is in the aperture box and illuminates a piece of Tyvek that reflects the light onto the mirror and into the camera. Taken from [106].

three relative calibrations, A, B, and C is housed in each telescope bay, see figure 2.13, and these calibrations are performed nightly during data-taking.

Every data-taking night calibration A (Cal A) records the response of the camera to a $57 \mu\text{s}$ long pulse of a stable light source at the beginning and end of data-taking, as shown in figure 2.14. Initially a 475 nm LED was used as the light source for Cal A, but in 2011 the LED was swapped for a 365 nm wavelength; the reasoning for the swap and the effects will be discussed in Chapter 3. The LED is located in a separate room and is fed into an optical fiber and then is split into seven fibers, one fiber for each telescope, and the seventh is coupled to a monitoring photodiode. The optical fiber for each telescope is mounted into the center of the mirror and coupled to a Teflon diffusor, see figure 2.13. Cal A measures the drift in camera response over the course of a night and through a two week data-taking period, and calibration constants generated from the integral of the responses are used to track the response of the camera between absolute calibrations with the drum. Calibrations

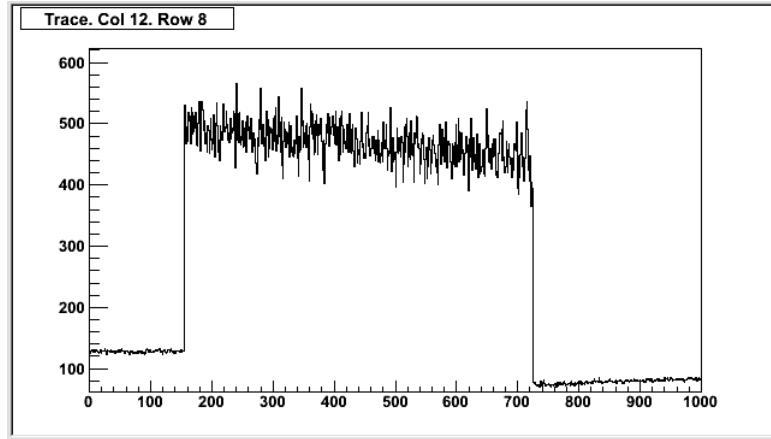


FIGURE 2.14. A typical calibration A pulse recorded by Los Leones telescope 3 from April 2013. The horizontal axis is time bins, each corresponding to 100 ns and the vertical axis is ADC counts.

B and C move progressively through the components that make up the FD telescope and use a xenon flasher [109] as their light source; located in the same room as the Cal A LED. Cal B has two optical fibers with 1 mm Teflon diffusors mounted on either side of the camera and are directed toward the mirror and therefore include the effect of the mirror in the calibration. The optical fibers for Cal C are fed into ports on the sides of the aperture and direct the light onto a reflective Tyvek sheet mounted on the inside of the aperture doors; the light bounces off the Tyvek and travels through the UV filter, the corrector ring, to the mirror and then into the camera.

Atmospheric calibration and monitoring are performed using various instruments from several locations all over the observatory, see figure 2.15. Each FD building site is equipped with a Lidar station that scans the nearby sky every hour of a data-taking night. The Lidar system measures the local aerosol scattering and absorption properties, and the cloud coverage and opacity [110]. These measured parameters are stored in databases and used to calculate the atmospheric attenuation of the fluorescence light on an event-by-event basis. In addition to the Lidar system, there is also the Central Laser Facility or CLF [112], which

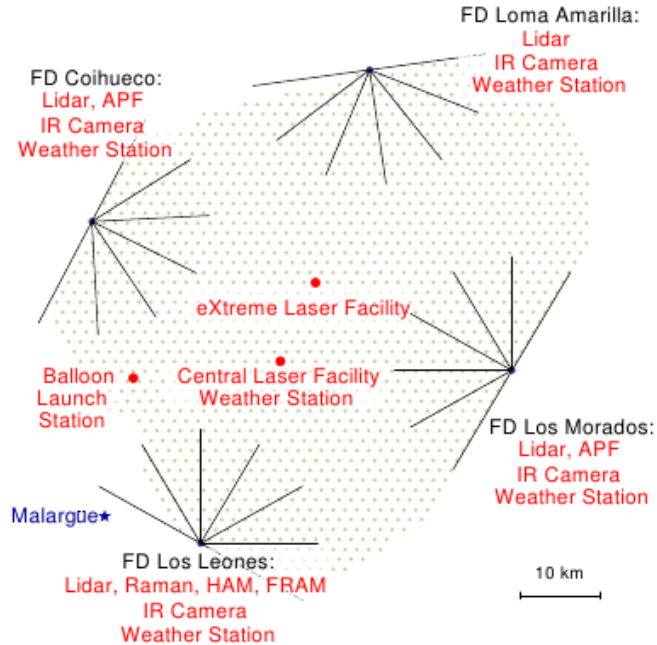


FIGURE 2.15. The locations of the various atmospheric monitoring and calibration devices used throughout the Observatory [111].

is located near the center of the SD array, and the eXtreme Laser Facility (XLF) located further north than the CLF. The CLF and XLF use a pulsed 355 nm UV laser with an average 6.5 mJ per pulse energy that serves as a test beam that can be observed by all FD telescopes and provides a crosscheck on the absolute calibration measured with the drum. Vertical laser shots are performed every hour and are also used to derive the atmospheric clarity [113]. The CLF and XLF are useful in monitoring the horizontal uniformity of the atmosphere above the whole array since together they can be viewed by all four FD sites.

Recently the Observatory has expanded upon its atmospheric monitoring systems by including an outside source of information, the Global Data Assimilation System (GDAS) [114]. GDAS is a global atmospheric model that provides publicly available data containing major state variables including temperature, pressure and humidity as a function of altitude with a time resolution of three hours. Data provided by the GDAS system for the atmosphere surrounding the Observatory are in good agreement with the local weather and atmospheric

monitoring stations [114]. The atmospheric monitoring is critical to the proper reconstruction of the air showers and thus the observables such as the energy of the primary cosmic ray and the location of X_{max} along the shower development.

2.3. RECENT EXTENSIONS OF THE OBSERVATORY

In the energy region between $\sim 10^{17}$ eV and $\sim 10^{18}$ eV there is a predicted transition from galactic to extragalactic dominated flux of high-energy cosmic rays that is hinted at by the 2nd knee feature [99], but this energy region is below the energy threshold for full efficiency for the original Pierre Auger Observatory, which is 3×10^{18} eV. In order to extend the reach of the hybrid measurement capabilities of the Observatory, enhancements have been introduced in both the SD and the FD. A small infill array of water tanks with 750 m spacing was added and placed in the field of view of three specialized FD telescopes that can be elevated by 30° , both of which extend the energy spectrum measurement to lower energies, see figure 2.16, and give a comparison to other experiments [115, 74].

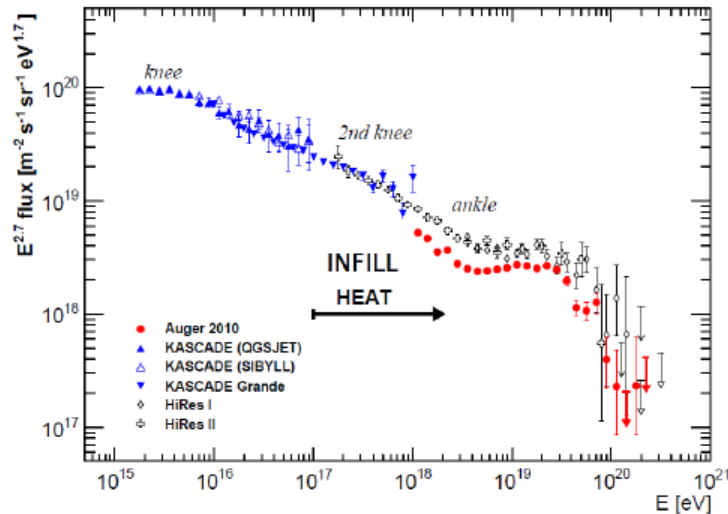


FIGURE 2.16. The cosmic ray energy spectrum scaled by $E^{2.7}$ to show features in the spectrum. The infill (AMIGA) and elevated telescopes (HEAT, see text for details) extend the Auger data to the tail of the arrow. Taken from [116]

2.3.1. HEAT AND AMIGA. The High Elevation Auger Telescope (HEAT) [117] is located near the Coihueco FD building and is composed of three individual buildings that house a standard FD telescope. When combined with Coihueco, HEAT extends the field of view of the Coihueco+HEAT telescope from the horizon to 60° in elevation and observes the longitudinal development of EAS that are of lower energy and interact earlier in the atmosphere and also extends the field of view to include the X_{max} of showers that would normally be out of the field of view of the FD as shown in figure 2.17. The change in eleva-

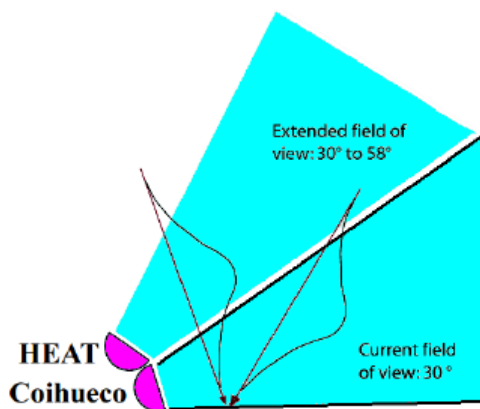


FIGURE 2.17. Extended field of view provided by elevating the HEAT telescopes an additional 30° above the Coihueco FD telescopes. The X_{max} of the closer shower is only visible with the addition of HEAT, taken from [116]

tion is accomplished by physically tilting the buildings that house the telescopes by 30° using hydraulics. Maintenance and calibrations are performed on the telescopes in the horizontal position. While horizontal the field of view of HEAT overlaps four of the telescopes of Coihueco and allows for the possibility of crosschecking with Coihueco by observing an event simultaneously. The data acquisition system (DAQ) for HEAT is an updated version of the one found on the other 24 telescopes with faster FPGAs and a higher sampling rate of 20 MHz instead of 10 MHz, so each time bin is 50 ns.

Complimenting the ability of HEAT to extend the FD energy range to lower energies an SD enhancement called AMIGA, (Auger Muons and Infill for the Ground Array) [118] was

placed near the Coihueco and HEAT detectors as shown in figure 2.18. The infill array covers an area of 23.5 km² with the water tanks set on a 750 m hexagonal grid. In addition to the

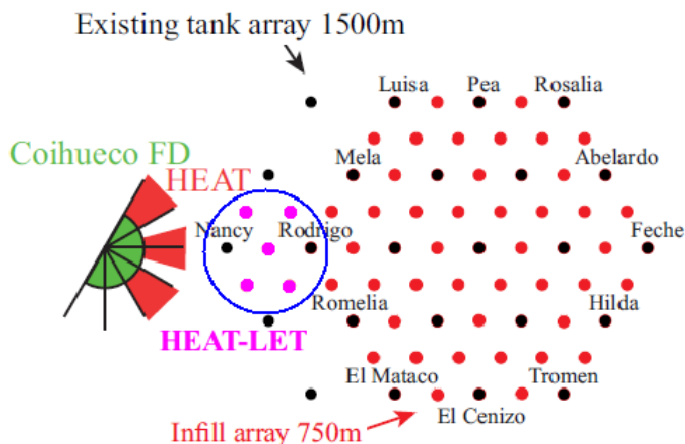


FIGURE 2.18. A schematic of the location of the AMIGA detector in relation to HEAT and Coihueco. The additional infill stations are in red (light gray) and the original array is in black. HEATLET was an initial hybrid trigger array used for commissioning HEAT. Taken from [116].

infill of water tanks, AMIGA is complimented by an associated set of muon detectors. The muon detectors are two 10 m² scintillator modules and two smaller 5 m² modules buried close to the infill tanks under 2.3 m of soil. These muon detectors will give valuable information on the muon content of EAS, which is sensitive to primary composition [103]. The water tanks used in the infill are the same design as those that make up the main SD so many of the strategies used for the regular array are incorporated into the infill event selection and reconstruction. The triggering and energy measurement based on LDF techniques are all based on those developed for the main SD.

HEAT and the infill array have been taking data since June 2010 and have improved on the energy spectrum measured by the Observatory down to 3×10^{17} eV as shown in figure 2.19.

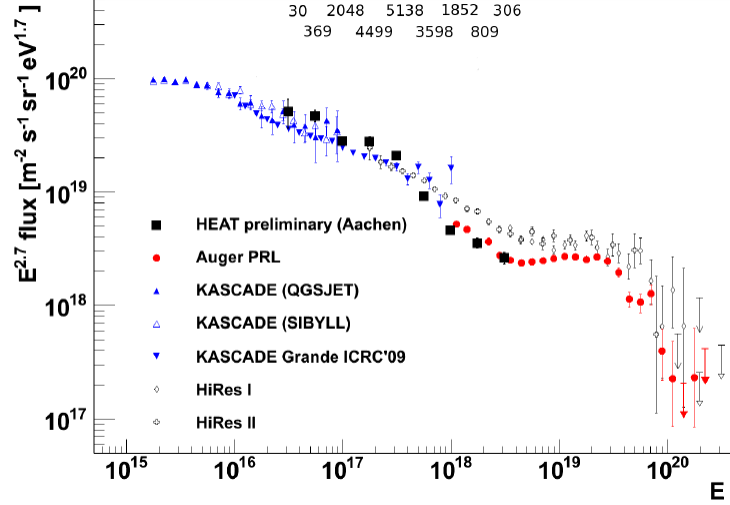


FIGURE 2.19. A preliminary energy spectrum showing the low energy enhancement of HEAT and AMIGA. The Auger energy spectrum now extends to at least 10^{17} eV. Taken from [119].

2.4. OVERVIEW OF RESULTS

There are recent results put out by the Pierre Auger collaboration that are susceptible to a change in FD calibration and may be affected by a better measurement of the multi-wavelength efficiencies of the telescopes; these results include the energy scale, energy spectrum, and composition of the primary particles as derived from X_{max} measurements from the FD.

2.4.1. ENERGY SPECTRUM. The energy spectrum of cosmic rays has been measured across more than 10 orders of magnitude in energy and more than 30 orders of magnitude in flux as was described in Chapter 1. One of the main purposes of the Pierre Auger Observatory is to measure the highest energies, greater than 10^{18} eV, with enough data to observe the GZK suppression and other features within the spectrum mentioned in Chapter 1. To that end, the most recent energy spectrum measured by the Observatory is shown in figure 2.20 with the addition of two types of functions fit to the data where the data have been multiplied by E^3 to enhance spectral features. Data above 2×10^{18} eV in the spectrum are derived from

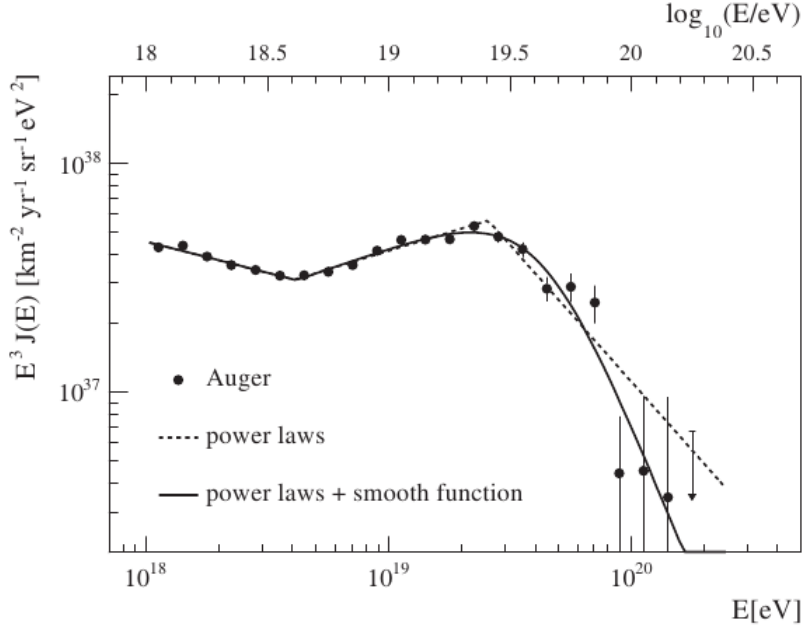


FIGURE 2.20. The energy spectrum measured by the Pierre Auger Observatory. The dashed line is a three power-law fit and the solid line is a power-law plus a smooth function. Uncertainties shown are statistical only and the systematic uncertainty in the energy scale is 22%. Taken from [120].

SD data that use the SD-FD energy calibration shown in figure 2.3 that means any change in the FD energy estimation from a different calibration will affect the spectrum above 2×10^{18} eV. A break in the spectrum named the “ankle” is observed at $\sim 10^{18.6}$ eV along with a suppression in the flux at energies greater than 4×10^{19} eV, which may indicate the GZK effect [92, 120, 121].

The overall systematic uncertainty in the energy scale at the time of this measurement was 22% with the dominant factor being the absolute fluorescence yield uncertainty of 14% [92]. Since then, improvements have been made to the fluorescence yield measurement [98, 122] used within the Auger collaboration and now the fluorescence yield uncertainty is 4%. With the new fluorescence yield measurement and other improvements the systematic uncertainty on the energy scale has been reduced to 14% with one of the largest factors being the FD calibration [103]. Within the FD calibration uncertainties are the systematics in the

absolute calibration and the multi-wavelength calibration. Previously the uncertainty in the absolute calibration was 9% [107], but as reported in [123] progress has been made and this uncertainty is now 4%. In addition, the uncertainties associated with the multi-wavelength measurement are reported in this work and have been reduced to 3.5%. Along with the improvement to the systematic on the energy scale there was also a 15.6% change to the energy of a shower at 10^{18} eV [103], which includes a 4.3% increase due to the change in multi-wavelength calibration detailed in [108]. This work presented here will show that the latest measurement of the multi-wavelength calibration of the FD will lead to a $1 \pm 0.03\%$ change in the energy of showers at 10^{18} eV.

2.4.2. COMPOSITION. Measurement of the chemical composition of cosmic rays can give clues to their origin and propagation, and the Pierre Auger Observatory aims to shed more light on this mystery. The Observatory is a great instrument for gaining more insight on the composition of cosmic rays for energies greater than 10^{18} eV because of its use of the fluorescence light detection method. The Heitler model of EAS [37] as described in Chapter 1 section 1.3.1 shows that the maximum number of particles in an EAS, N_{max} , is related to the natural log of the mass of the primary particle. The FD directly observes the atmospheric depth at which N_{max} occurs, X_{max} , because the amount of light given off by an EAS is related to the number of particles in the EAS; this X_{max} measurement is the primary means by which the Observatory makes a measurement on the chemical composition.

Recently there have been several studies [124–128] into how X_{max} changes as a function of energy, along with spread in X_{max} distributions for increasing energy bins that have given hints on cosmic ray composition. Shown in figure 2.21 is the average value of X_{max} , $\langle X_{max} \rangle$, as a function of energy for 6744 events that passed strict data quality cuts described in [126, 127] using 18 bins of $\Delta \log(E/\text{eV}) = 0.1$. The data are not described well by a single

fit, but as can be seen in the figure using two slopes with a change at $\log(E/\text{eV}) = 18.38^{+0.07}_{-0.17}$ yields a much better description of the data, see [127] for details. The solid and dashed lines above and below the data are simulations using various hadronic interaction models [129] predicting the value of X_{max} for proton and iron primary particles respectively. In addition,

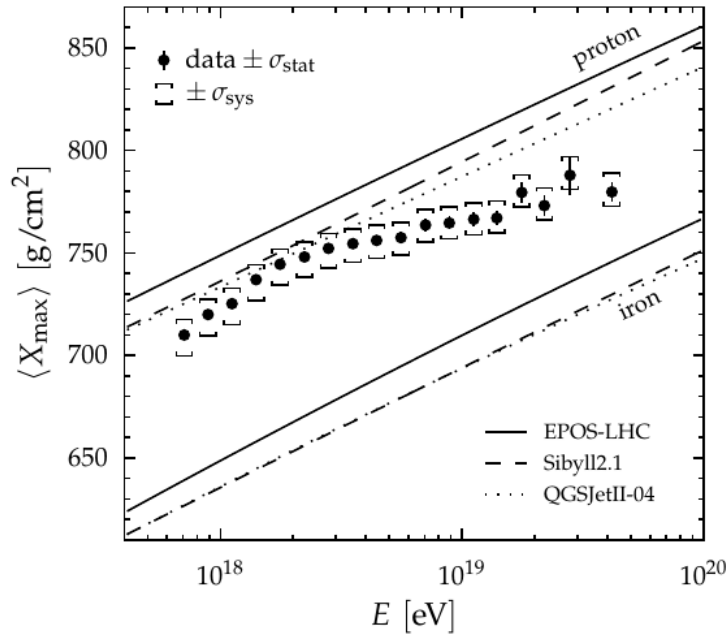


FIGURE 2.21. $\langle X_{max} \rangle$ as a function of energy compared to various hadronic interaction model predictions. Numbers below the data are the number of events in that energy bin and the brackets are the systematic uncertainties at each energy bin. Taken from [128].

the one-sigma widths of the eighteen energy bin distributions are shown in figure 2.22.

In the two figures 2.21 and 2.22, the X_{max} data are showing a change in composition in primary particles with an increase in energy. The $\langle X_{max} \rangle$ definitively shows that there is a change in slope of the elongation rate. If the hadronic models can be trusted at these extrapolated energies, then figure 2.21 shows an increase in mass at higher energies and that at the highest energies shown it is a mixture of masses, with fractions of proton and iron, or other nuclei, contributing. More data are needed to extend this measurement to the highest energies, greater than 3×10^{19} eV.

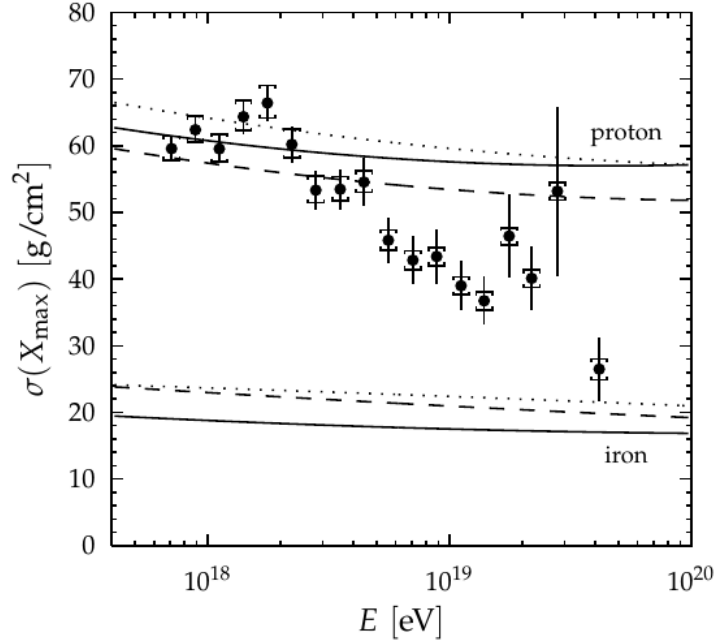


FIGURE 2.22. $\text{RMS}(\langle X_{max} \rangle)$ as a function of energy plotted similarly to figure 2.21 and also taken from [128].

The more compelling measurement is the spread on these $\langle X_{max} \rangle$ distributions, or the $\text{RMS}(\langle X_{max} \rangle)$. As was discussed in Chapter 1 section 1.3.1 the superposition model predicts that for more massive primaries the spread in X_{max} will be smaller than that of less-massive ones. Figure 2.22 shows for an increase in energy $\text{RMS}(\langle X_{max} \rangle)$ is decreasing, which is indicative of a change from low mass to high mass primaries according to the superposition argument. The $\text{RMS}(\langle X_{max} \rangle)$ decreases from $55 \frac{g}{cm^2}$ to $26 \frac{g}{cm^2}$ and the decrease with energy becomes steeper around the change in slope measured in the $\langle X_{max} \rangle$ measurement.

The Auger Observatory X_{max} data are controversial due to the trend toward higher masses at the highest energies, which is opposite what a previous experiment have measured [130]. In addition to disagreeing with previous experiments, this result also means that at the highest energies cosmic rays would be dominantly high mass particles such as an iron nucleus, which are far more susceptible to magnetic fields, leading to an inability to correlate arrival directions of cosmic rays with their sources, see the appendices of [131].

The effects due to a change in multi-wavelength calibration on the X_{max} measurement are more subtle than their effect on the energy estimation. Whereas measuring the energy of the cosmic ray using the FD depends on the total amount of light detected and therefore any change in the efficiency of the telescope will affect this measurement; the X_{max} measurement depends on how the fluorescence light is produced and attenuated.

CHAPTER 3

CALIBRATION

Calibration is a vital part of any experiment, it relates the response of a detector to a known physical process from which relationships can be deduced and the underlying physics can be understood. It is very important in a particle physics experiment, where the response of the detector is the only tangible evidence of the physics taking place.

Calibration within the Pierre Auger Observatory uses the same principle for both the SD and the FD, it connects the signal to the number of particles present in the detector, but how this relationship is determined is drastically different for each detector. For the FD, the number of particles it detects is closely related to the energy contained in a cosmic ray, but for the SD the relationship between detected particles and energy is more complicated. With each detector calibrated, the Auger Observatory utilizes its hybrid design and the FD energy is used to calibrate the the SD energy measurement allowing for use of the large SD dataset in a model-independent way.

3.1. SURFACE DETECTOR CALIBRATION

The surface detector has nearly a 100% duty factor and therefore must be calibrated in such a way not to interfere with its data taking, and due to the remote locations of the 1600 water tanks the calibration must be performed autonomously. Calibration is performed by using the low energy muons that pervade our atmosphere and penetrate the water tanks at nearly 2.5 kHz. The charge resulting from the Cherenkov light in the PMTs produced by the atmospheric muons is converted into a unit of signal produced by a vertical and central through-going (VCT) muon [132]. Once the charge has been converted, the lateral distribution function (LDF) that describes the EAS particle density versus distance at the

ground is parameterized in these units, and the signal produced by particles passing through a station at 1000 meters from the core, $S(1000)$, is used to derive the shower energy. $S(1000)$ is calibrated using simulations and models that calculate the expected number of VCT units for the electromagnetic component of the shower at that distance from the shower core. These simulations are checked by a subset of events that are observed by both SD and at least one FD, known as hybrid events, where the calorimetric energy measurement of the cosmic ray obtained from the FD is used to calibrate $S(1000)$.

3.1.1. THE VERTICAL-EQUIVALENT MUON. The charge generated in the PMTs due to Cherenkov light from extensive air showers is parameterized in units of charge as would result from a VCT muon, the unit is named the vertical-equivalent muon (VEM). Signals recorded by the SD stations are converted into these units, and then the shower characteristics are parameterized in terms of VEMs. The SD calibration must then convert the water tank response, namely integrated ADC channels, into VEMs.

The nearly constant flux of low energy muons is a perfect handle for determining the charged deposition for a VCT, but the water tanks cannot distinguish a VCT from any other muon. The distribution of the light in the water tanks detected by the three PMTs

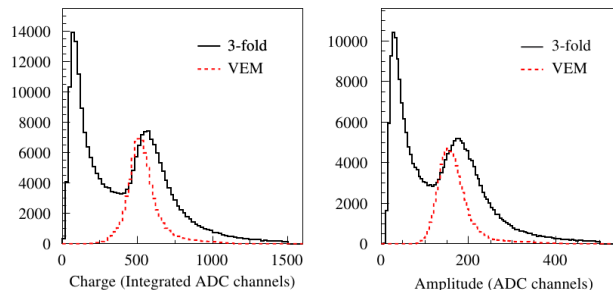


FIGURE 3.1. Charge and pulse amplitude from a water tank, triggered by a 3-fold coincidence between all 3 PMTs. The red dashed line is produced by an external muon telescope providing the trigger to select only VCT muons. Taken from [134].

has a peak in its charge distribution [133], which is measured to be 1.09 VEM for the sum of the three PMTs and 1.03 ± 0.02 VEM for each PMT [134], as shown in figure 3.1. As described in Chapter 2 section 2.1, the peaks are labeled Q_{VEM}^{peak} and I_{VEM}^{peak} for the charge peak and amplitude peak respectively. The procedure for the on-the-fly calibration of each water tank in the SD is described in detail in [134], but the relationship between Q_{VEM}^{peak} to one VEM is used as the conversion from integrated PMT ADC channels to VEM units.

With the signal from the water tanks calibrated in terms of VEMs, the signal measured in a tank at an optimal distance away from the shower core, $S(r_{opt})$, is then linked to the energy of a primary particle [89]. The choice of $S(r_{opt})$ depends only on the geometry of the array. Previously Havarah Park used 600 m as the optimal distance [89] where the detector spacing varied but covered an area of 12 km². The spacing of the Auger-SD array being 1.5 km and the geometry of the water tanks meant the distance of $S(r_{opt})$ had to be increased. Work done in [90] varied the distance at which to measure the shower size, and showed that the signal measured at 1000 m for an array with spacing of 1.5 km gave an optimal average LDF, where the optimal distance showed the least dependence on an assumed LDF. Within the Auger Observatory the signal at 1000 m, $S(1000)$ is used to estimate the shower size, and therefore the shower energy.

The Pierre Auger Observatory uses hybrid events to link this signal, $S(1000)$, measured by the SD to the energy measured by the FD. All previous ground array cosmic ray experiments had to rely on models to predict the number of particles at a given distance from the shower core and then relate the number of particles to the expected signal in a detector as a function of distance and finally the signal at an optimal distance $S(r_{opt})$. The events used in the Auger SD energy calibration analysis are known as golden events, where the FD and SD have been triggered independently by the same EAS. Several data-quality and field of view cuts [135] are

placed on the golden events such that a small subset of the events pass. Shown in figure 3.2

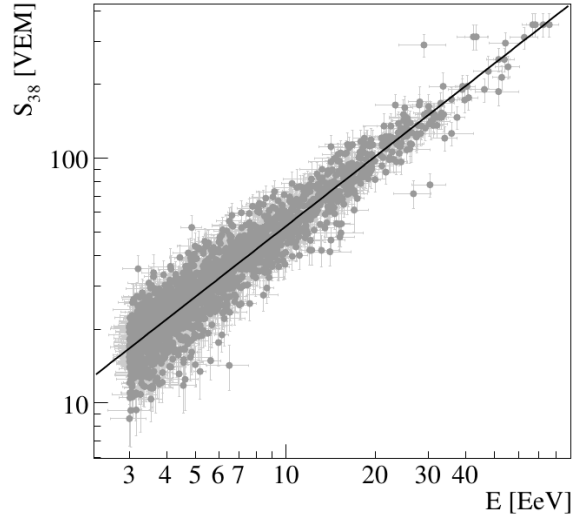


FIGURE 3.2. Correlation between SD measured shower size, S_{38} , and measured FD energy for 839 selected golden hybrid events. Taken from [103].

is the most recent calibration of the SD energy estimation with the energy measurement of the FD. The signal size parameter shown on the y-axis in figure 3.2, S_{38} , is related to $S(1000)$ by (3.1)

$$S_{38} \equiv S(1000)/f_{CIC}(\theta) \quad (3.1)$$

where $f_{CIC}(\theta)$ is determined via the Constant Intensity Cut (CIC) method [91]. The CIC removes the zenith dependence of $S(1000)$ due to the attenuation of the shower particles and geometrical effects, by assuming an isotropic flux of primary cosmic rays at the top of the atmosphere and fitting an attenuation curve to the data. The attenuation curve is a third degree polynomial satisfying (3.2).

$$f_{CIC}(\theta) = 1 + ax + bx^2 + cx^3$$

$$\textit{Where :} \quad (3.2)$$

$$x = \cos^2(\theta) - \cos^2(\bar{\theta})$$

The parameters in (3.2) are $a = 0.98 \pm 0.004$, $b = -1.68 \pm 0.01$, $c = -1.30 \pm 0.45$ [103], and $\bar{\theta} = 38^\circ$.

The relationship between the two energy measurements is given by a simple power law, $E_{FD} = A \times (S_{38})^B$, and for the most recent hybrid energy calibration the values A and B are $0.190 \pm 0.005 \times 10^{18}$ eV and 1.025 ± 0.007 respectively [103].

The hybrid nature of the SD energy calibration means that the FD energy measurement must be very robust since the Auger SD has nearly a 100% duty cycle and measures the highest energy events. The cosmic ray events measured by the Auger Observatory depend greatly on the FD energy measurement and therefore the FD calibration is critical to the experiment.

3.2. FLUORESCENCE DETECTOR CALIBRATION

The fluorescence detector directly measures the amount of light given off by an EAS in the form of nitrogen fluorescence, which is related to the amount of electromagnetic energy deposited into the atmosphere. Fluorescence detector calibration must relate the signal measured in number of FADC, (flash ADC) counts, n_{FADC} , to the amount of light incident on the telescope aperture. The relationship is shown in (3.3) as defined in [104]

$$n_{FADC} = \frac{dE}{dX} \times Y_\gamma \times \Delta X \times \tau \times \frac{A}{4\pi r^2} \times C^{Abs} \quad (3.3)$$

where dE/dX is the rate at which energy is deposited for the track length ΔX , Y_γ is the precise measurement of the fluorescence yield [136], τ is the atmospheric attenuation factor, A is the telescope aperture area, r is the light path from the EAS to the telescope, and C^{Abs} is the absolute calibration factor. Precise measurements of the calibration factor in the above expression along with the fluorescence yield are all that is needed to determine the amount

of energy deposited into the atmosphere. The work presented in sections 3.3 and 3.4 deal with determining C^{Abs} for a single wavelength, and then relating this calibration constant over the nitrogen fluorescence spectrum by measuring the FD efficiency as a function of wavelength. The first step in energy calibration is understanding the calorimeter, which for the Auger Observatory is the atmosphere.

3.2.1. **ATMOSPHERIC CALIBRATION.** Nitrogen fluorescence light is emitted isotropically near the core of an EAS and then travels several kilometers through the atmosphere before being detected by one of the fluorescence telescopes at the periphery of the SD array. During the passage through the atmosphere the fluorescence light attenuates due to the presence of air molecules and aerosols. Knowing the amount of attenuation is required to determine the total amount of light emitted at the shower for the correct energy measurement for the FD. In addition, the atmospheric conditions also affect the nitrogen fluorescence production at the shower, Y_γ [137], and thereby alter the amount of energy needed to produce a given number of fluorescence photons.

The Pierre Auger Observatory actively monitors the atmosphere above the observatory, including aerosol content and other atmospheric parameters (pressure, temperature, etc.) using various techniques summarized in [104]. Weather stations located at all of the FD sites and one in the Central Laser Facility (CLF) [112] measure the temperature, pressure, and humidity every five minutes. The weather data are used for calculating atmospheric effects on the nitrogen fluorescence production along with effects on the SD signal [138].

Understanding the attenuation of the fluorescence light is needed for a proper calorimetric measurement of the energy deposited into the atmosphere, and to that end, the aerosol content of the atmosphere is monitored with several detectors every night of FD data-taking. Hourly measurements are made of aerosols by the FDs observing vertical UV laser shots

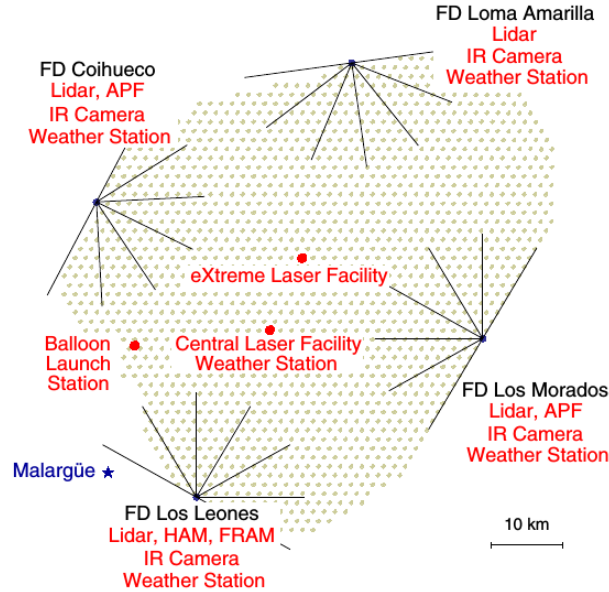


FIGURE 3.3. Map of the locations of atmospheric monitoring equipment and facilities throughout the Observatory, from [139].

performed by two laser facilities located near the center of the SD array, the CLF [112] and the eXtreme Laser Facility XLF [139]. The CLF has recently been upgraded to include a Raman backscattering telescope to allow for an independent measurement of the aerosol optical depth and other atmospheric properties, and an improved laser calibration system [104, 140]. Near each FD building site there are LIDAR stations that measure the atmosphere near the fluorescence telescopes [110]. Cloud cameras are also in place at two of the FD buildings to monitor the cloud coverage and provide a veto for the FD shower data that were observed during overcast nights, or when a cloud was in the field of view for a given event [141]. Figure 3.3 shows the locations of the various atmospheric monitor devices and facilities. Recently the aerosol content above the observatory has been tracked using satellite databases of paths taken by aerosols during seasonal weather patterns, and periods of good air quality were determined in addition to the local monitoring at the observatory [114, 142].

The attenuation of the fluorescence light is dominated by Rayleigh scattering, which has a strong wavelength dependence, following the λ^{-4} Rayleigh law as shown in [143], meaning

the shorter wavelengths in the nitrogen spectrum are more strongly scattered the further the EAS is from the FD. The effect on the shorter wavelengths will be an important factor when combined with the multi-wavelength calibration and any changes in the FD efficiency as a function of time.

3.2.2. RELATIVE CALIBRATION. Tracking the short term behavior of the FDs is accomplished using the relative calibration systems in place for each telescope. There are three optical calibration systems, Cal A, Cal B, and Cal C, that monitor and track the response of different parts of the optics throughout the telescope. The relative calibration monitors the variation of the telescopes between the absolute calibrations as described in section 3.3.

Shown in figure 3.4 are the locations of the three relative calibration light sources within the geometry of the fluorescence telescope. Cal B and C use a xenon flasher, where in each

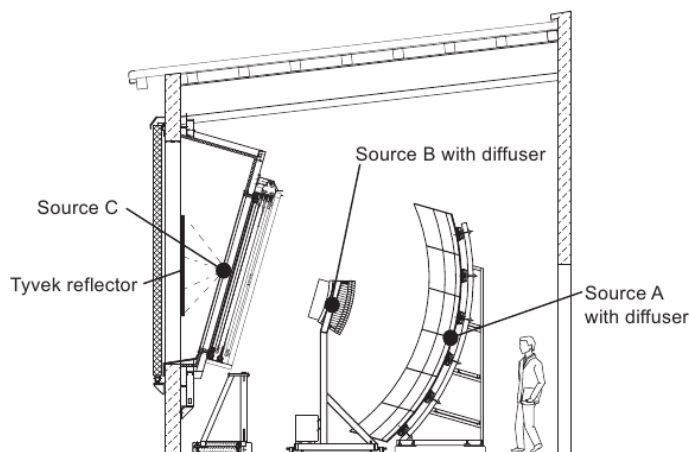


FIGURE 3.4. Locations of the output of the three relative calibrations schematically shown within an FD telescope bay, from [144].

system the output of a different flasher is fed into a 1:7 optical fiber splitter and the six fibers go into their respective telescopes and the seventh leads into a monitoring photodiode. For Cal B the output fiber is split and mounted on either side of the camera where the light passes through a 1 mm Teflon diffuser. The light illuminates the mirror and is then reflected

into the camera. The purpose of Cal B is to monitor the reflectivity of the mirror and track possible changes due to accumulating dust or other deposits on the mirror such as white dielectrics.

The output of Cal C is split in two and routed to either side of the telescope aperture external to the filter window where the fibers are aimed at a sheet of Tyvek mounted on the inside of the shutter doors such that the light then diffusively reflects back through the UV filter and through the whole optical system of the telescope. Cal C is intended to monitor the transmission of the UV filter and corrector ring when compared to Cal B.

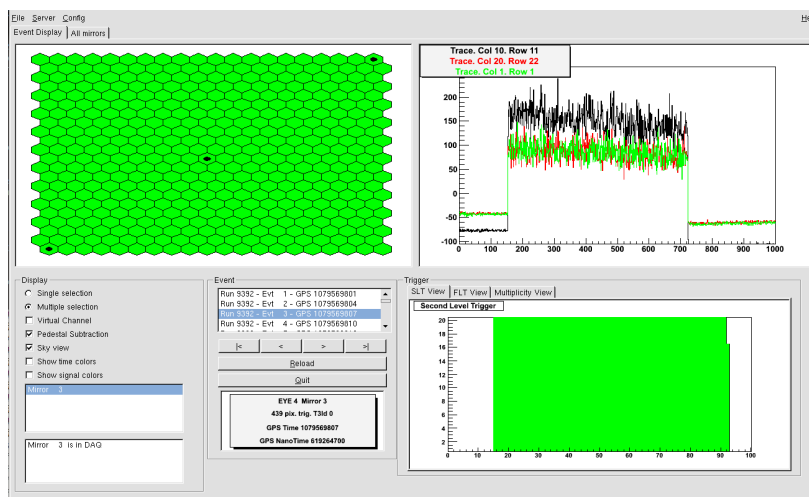


FIGURE 3.5. The response of three pixels to a $57 \mu\text{s}$ Cal A light pulse from March 2014. The upper left portion of the figure shows three selected pixels within the camera, and their response is shown in the plot to the right; note variation between the response of the pixels is normal.

While all three relative calibrations are performed at the beginning and end of every FD data-taking night, the framework for the Cal A system is such that it is used to track the response of every PMT in all the FDs between absolute calibrations performed with the drum, for details see [104]. The light source for Cal A is an LED, originally 475 nm, but in 2011 a conversion was made to a 365 nm LED, fed into an optical fiber setup similar to Cal B and C. The main reason for the switch to a 365 nm LED was to align the wavelengths of

the Cal A calibration with the drum calibration, and this was only possible recently due to the availability of reliable high-power 365 nm LEDs. The end of the fiber is located at the center of the mirror with a 1 mm Teflon diffuser as shown in figure 3.4. Cal A illuminates the whole camera with a $57 \mu\text{s}$ square light pulse. Figure 3.5 shows the response of three pixels to a Cal A pulse taken during an absolute calibration campaign.

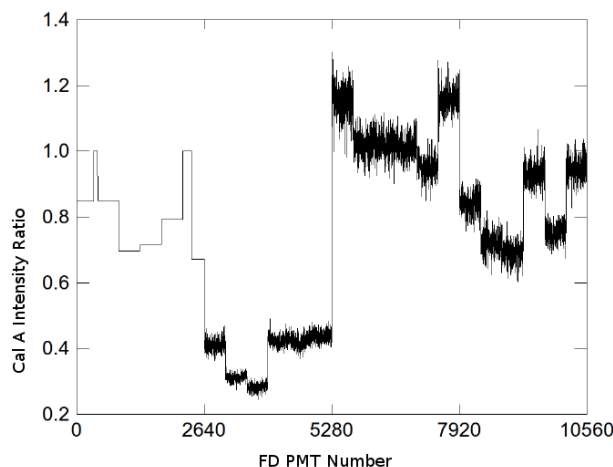


FIGURE 3.6. Cal A intensity offsets due to the swap from a 475 nm to 365 nm LED. Camera averages were used for PMTs at Los Leones due to there being no good before/after Cal A runs.

The intensity difference between the 475 nm and 365 nm LEDs was taken into account at the FDs by taking Cal A runs before and after the swap such that a ratio could be determined and an offset applied to the calibration constants for every PMT. During the April 2013 calibration campaign, we analyzed the before and after LED swap Cal A data, and applied the ratio of intensities to each of the nearly 11000 PMTs within the Observatory, except for those at Los Leones due to there not being good before/after Cal A runs. The ratio for the PMTs at Los Leones were calculated using camera averages. Figure 3.6 shows the ratio in intensities for the LED swap on Cal A. For a detailed analysis of the relative calibration data see [144].

3.3. ABSOLUTE CALIBRATION AND THE “DRUM” LIGHT SOURCE

Absolute and multi-wavelength calibrations of the fluorescence telescopes are performed using a low-intensity uniform light source that fills the entire aperture of the telescope; it is 2.5 m in diameter and resembles a drum in appearance and is lovingly referred to as the “drum”. The advantage of the large drum light source is that it allows for an end-to-end measurement of all detector components thereby calibrating the combined effect of each component in a single measurement. Absolute calibration is a single-wavelength measurement where the absolute flux of photons being emitted from the drum is calibrated and the response of each pixel in the telescope camera is measured, giving the calibration, C^{Abs} for each pixel. Multi-wavelength calibration, also using the drum, measures the relative response of the FD telescope to a broad UV source covering the nitrogen fluorescence spectrum so that the response as a function of wavelength is calibrated relative to the absolute calibration.

3.3.1. THE DRUM AND ITS CALIBRATION. As mentioned earlier, in order to efficiently calibrate each FD telescope, a portable light source was developed that uniformly illuminates all 440 PMTs simultaneously with a calibrated photon flux.

3.3.1.1. *The Drum.* The drum is a hollow cylinder 1.4 m deep and 2.5 m in diameter, and to keep its weight low it is constructed in sections of laminated honeycomb cardboard with an aluminum shell. Tyvek lines the interior surfaces of the drum, and a 0.38 mm thick sheet of Teflon is stretched over the opening, these materials are diffusively reflecting and transmitting in the UV. The drum itself is illuminated using a stable UV LED [145] with a peak at 365 nm that shines through a cylindrical Teflon diffuser and is mounted on the front face of the drum. On the inside of the Teflon face where the LED protrudes into the interior there is a reflector cup lined with Tyvek with a geometry such that photons exiting

the Teflon diffuser make at least one bounce before reflecting into the drum. The drum set up is shown in figure 3.7. All of the diffusive materials ensure that the drum is Lambertian

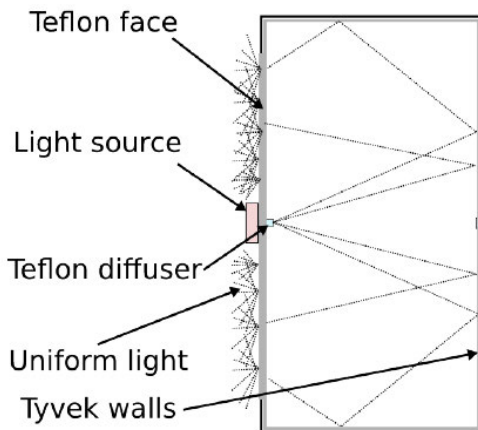


FIGURE 3.7. A schematic of the drum showing the diffusively reflecting Tyvek on the interior and the diffusively transmitting Teflon on the face. The UV LED is mounted on the front in the center of the Teflon face illuminating the interior of the drum.

and uniformly illuminates the FD camera [146].

A Lambertian emitter is such that the light intensity emitted from any surface element, A , per unit solid angle only depends on the viewing angle, following $I(\theta) = I_0 A \cos(\theta)$. When

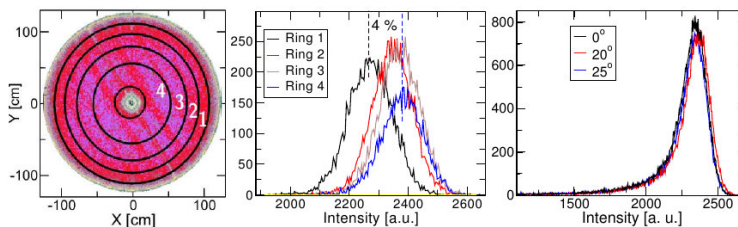


FIGURE 3.8. Drum uniformity measurements made by determining the variation across the face of the drum via the arbitrary intensity found in four concentric rings. Shown in the rightmost plot is the lack of intensity dependence on angle, proving that the drum is a Lambertian emitter. Taken from [146].

measuring the drum at an angle its surface area goes as $\cos(\theta)$, so the measured intensity is then independent of the viewing angle. Imaging studies were performed on the drum using a CCD at a distance of 14.40 m, where the Teflon face was imaged at 0° , 20° , and 25° . The

right plot in figure 3.8 shows the measured CCD intensities for three angles and they show very little difference, proving that the drum is a Lambertian emitter. Each PMT in the camera of the FD observes a different solid angle of the aperture, where the center PMT has the largest and the ones in the corners have the smallest, but since the drum is Lambertian they all receive the same intensity of photons. The head on image was used for a uniformity study where the response of the CCD was divided up into 4 annular regions, shown on the left in figure 3.8, and the average intensities varied by 4% across the Teflon face.

As mentioned above, the drum was constructed to be light enough to be portable so it could be transported to the FD buildings across the 3000 km² observatory and placed into the telescope apertures as easily as possible. The drum is mounted in a custom steel dolly with hydraulic scissor jacks on either side that are used to elevate the drum to the height of FD apertures. Shown in figure 3.9a is a picture of the CSU calibration group standing next to the drum and dolly at an FD building. Positioning the drum in the aperture at the correct angle is done using two sets of screw jacks. The first set are mounted on either side of the drum and must be manually turned in sync, as is shown in figure 3.9b, and the second rotates the drum into the aperture such that the Teflon face covers the UV window and makes contact around the circumference of the drum. The drum is transported across the observatory in a custom trailer towed by a truck, see figure 3.9c, inside the trailer the drum is secured into place with several ratchet straps, and the prayers of the calibration group.

3.3.1.2. *The LED Light Source and Electronics.* The LED and associated controlling electronics are housed in a small aluminum box, 8" on a side, which is mounted at the center of the Teflon face with the LED illuminating the interior of the drum, see figure 3.10 for a schematic of the light source and its electronics enclosure. The LED is mounted on a Peltier unit with a fan coupled to a radiator. The electronics control the Peltier current to provide



(A) Calibration group standing next to the drum and dolly at an FD building site.



(B) The drum being positioned into an aperture with the scissor jacks extended.



(C) The trailer housing the drum being towed with an Auger Observatory truck over the dirt road.

FIGURE 3.9. Pictures showing the logistics of transporting the drum across the arid terrain at the observatory site in the custom trailer and the custom dolly that is used to position the drum into apertures at FDs.

temperature control of $22 \pm 0.5^\circ\text{C}$ for the LED that keeps the peak emission wavelength of the LED at $365 \text{ nm} \pm 0.1\%$ measured over five days when run in pulsed mode [123]. Previous iterations of the LED unit did not have temperature control and a 10 nm drift in the peak emission wavelength was measured when the LED was operated in DC mode, leading to an unknown uncertainty in absolute photon flux [146]. The measured drift without the Peltier in the peak of the LED emission spectrum is shown in figure 3.11, note that the LED was operated within the manufacturer guidelines.

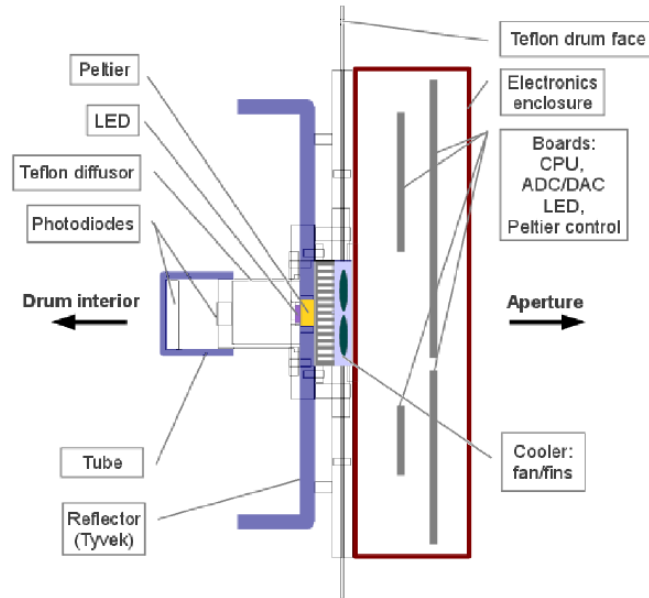


FIGURE 3.10. A schematic of the LED light source and accompanying controlling electronics housed in an aluminum box mounted on the Teflon face of the drum, taken from [123].

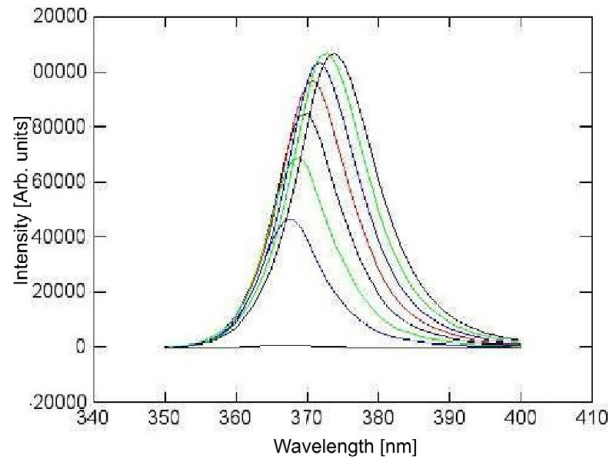


FIGURE 3.11. Measurements showing the ~ 10 nm drift in the LED spectrum while the LED was run in DC mode within the manufacturer specified limits. The current calibration uses active temperature control via a Peltier unit and runs the LED in pulsed mode to achieve 0.1% variation in the LED spectrum.

Covering the LED is a Teflon diffuser that comes in two variations. When used in the drum, the diffuser is cylindrical and photons are emitted radially, bouncing off the reflector cup at least once before diffusing into the drum. A cap can screw down on the Teflon diffuser and change the photon flux emitted, and within the Teflon diffuser there is a small

photodiode that is used to monitor the LED on a pulse by pulse basis. The other diffuser configuration is used during the drum calibration, as described in section 3.3.1.3.

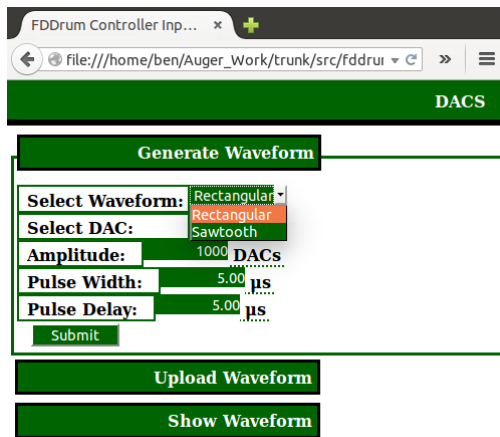
The electronics package that runs the LED, its temperature stability, and the data acquisition from two sensors was developed at CSU and is highly customizable. There are two main electronics boards, one is for data acquisition with a Xilinx Spartan3A programmable logic device that is controlled via the other board with a 600 MHz BlackFin BF537 processor running a version of μ Clinux [147]. The acquisition board holds four 12-bit DACs, one of which controls the LED current and two 12-bit ADCs for reading in signals from either a PMT or monitoring photodiodes at a rate of $100 \frac{MS}{s}$.

Customization of the LED pulse or triggering for data acquisition is achieved with a web page interface that uses cgi code written, compiled, and then stored in the on board memory of the electronics package, see figures 3.12. The LED pulse amplitude and shape can be varied from typical square pulse to any shape that can be described by an analytical function, such as a sawtooth or Gaussian, and the pulse rate and or trigger rate can also be varied. The pulse widths can vary from $0.1 \mu s$ to $40 \mu s$, and the amplitude maxes out at 4096 “DAC”

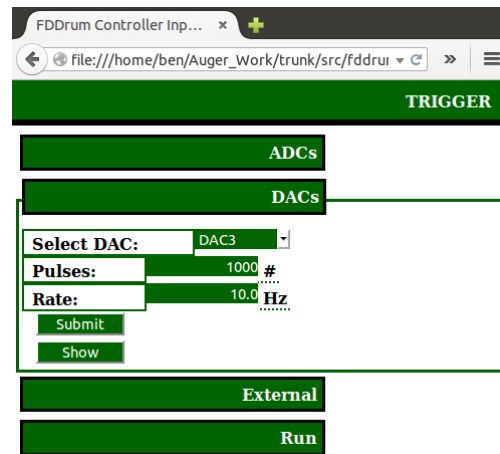
units, which are a conversion from the voltage put on the DAC. The light pulse shaping information is set on the webpage shown in figure 3.12a. After setting the pulse information, the trigger rate and number of pulses for the particular DAC is set on the webpage shown in figure 3.12b. On the same triggering webpage, the ADC(s) that are connected to either a photodiode or PMT can be set to trigger off of the internal DAC(s), from an external source, or set to trigger if their signal goes above a set threshold, as displayed in figure 3.12c.

For measurements made with the NIST calibrated photodiode, as explained in the following section, the webpage controlling the Keithley electrometer is shown in figure 3.12d.

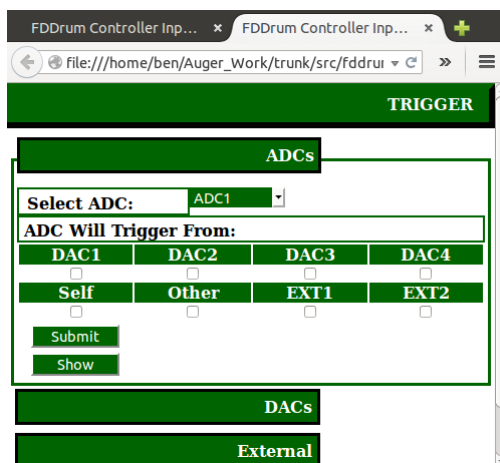
The electrometer mode is set, typically as an ammeter, and then a measurement can be taken of the charge generated by the NIST photodiode. The data are read in through cat



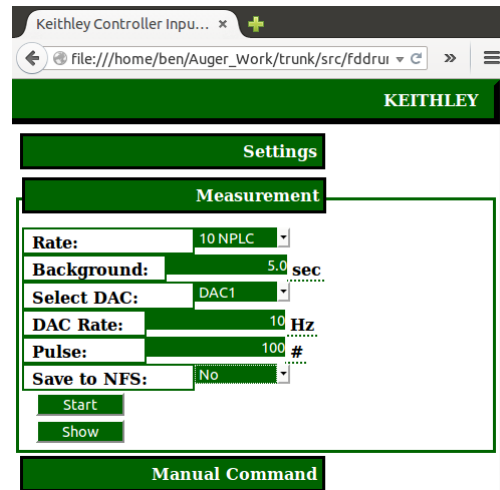
(A) Web page for selecting pulse shape, amplitude, and width.



(B) Once the light pulse has been selected, the number of pulses and trigger rate are set with this web page.



(C) The ADC that read in either a photodiode or PMT can be triggered from the various DACS, externally, or internally via a threshold.



(D) The Keithley electrometer is controlled and read in when using the NIST photodiode, see text for details.

FIGURE 3.12. The various webpage interfaces used for the Absolute drum calibration, see text for details about each one.

5 cables after the signals from the PMT or photodiode have been amplified and converted to a differential signal on a front-end board, and then are stored on the 32 Mb on board memory; from there the signals are transferred to a laptop over a wireless LAN. The wireless

communication of the drum LED electronics allows remote operation of the drum from inside an FD building while performing calibration on a given telescope.

3.3.1.3. *Absolute Calibration of the Drum.* Before heading out into the field and calibrating the FD telescopes, the drum must be calibrated such that the absolute photon flux being emitted from the Teflon face is known. The drum is designed to approximate the EAS initiated fluorescence light intensity at the aperture, but this intensity region is a “no-man’s-land” in terms of determining absolute photon flux using the conventional methods. The drum intensity is too high for single photon counting using a PMT, and it is too low and the drum is too large for direct measurements with a calibrated photodiode, but for simplicity and ease-of-use reasons our calibration standard is a UV photodiode calibrated at NIST [148]. The calibration group has developed methods to overcome this calibration conundrum.

The general method has been to transfer the calibration of a NIST calibrated photodiode to the response of a PMT, which can be accomplished in four steps. The first step is to measure the response of a PMT to the drum illuminated by the LED light source, where this is typically a 5 μ s wide pulse of amplitude to mimic an EAS signal in the FD, and viewed at a large enough distance, 15 m, so that photons incident on the PMT face have an angle of incidence less than five degrees, which can be trivially worked out from the length of the dark hall used in Malargüe, and radius of the drum. It is important for the photon angle of incidence to be near normal for achieving nominal photoemission [149], and non-normal light may reflect off internal structures and strike a photoemissive surface within the PMT, leading to an increased signal [150]. Next the response of the PMT to a light source is measured, and the intensity of the light source is adjusted such that the PMT gives the same response as it did when measuring the drum setup. Ensuring the two responses from

the PMT are the same implies that the photon flux reaching the PMT is the same as it was with the drum. Then PMT is replaced with the NIST calibrated photodiode and the light source is moved closer, and the current, I_{PD} , is measured from the increased photon flux. Now using the calibrated spectral response of the photodiode, which is in units of $[\frac{A}{W}]$, the number of photons is calculated using a similar relationship to what is shown in (3.4), where the NIST calibration, $CAL_{NIST}(\lambda)$ is wavelength dependent and the energy per photon, $E(\lambda)$, is dependent on the LED wavelength.

$$N_{\gamma} \propto \frac{I_{PD}}{CAL_{NIST}(\lambda) E(\lambda)} \quad (3.4)$$

After the number of photons, N_{γ} , is calculated the measured attenuation factor is applied and the photon flux being emitted from the drum is known.

Previously, neutral density filters, NDFs, were used in conjunction with measuring the response of the PMT to a light source after the drum measurement. The NDFs had an attenuation factor of ~ 5000 to overcome the difference in sensitivities of the PMT and photodiode, which is on the order of 10^5 as described in [151]. Problems with the NDF technique arose out of the diffuse nature of the light sources that led to a large uncertainty in the attenuation applied by the NDF. Also the calibration electronics were not as sophisticated as they are now, specifically the temperature control of the LED. Local junction heating caused by running the LED in DC mode caused a shift in its peak emission wavelength, which affects the calculation of the photon flux due to the wavelength dependence seen in (3.4). At that time the best uncertainty on the drum calibration was 6% [146], which affects the overall Auger Observatory energy.

Recently a new technique using $\frac{1}{R^2}$ attenuation of light has been implemented along with the more developed electronics described in section 3.3.1.1, and the uncertainty in the drum

calibration has been reduced to 2.1% [123]. In order to reproduce the attenuation given by the NDFs using the $\frac{1}{R^2}$ attenuation of light means having a distance change factor of about 70. The factor of 70 in distance is attainable in the 17 m long calibration dark hall located at the Pierre Auger Observatory campus in Argentina by moving the LED light source from a distance of 15 m to 20 cm.

The $\frac{1}{R^2}$ calibration technique was put into practice recently due to acquiring new lab space at the Auger Observatory campus in 2009. The space included an office with an adjoining wall to the 17 m long dark hall. The calibration group cut a 0.3 m diameter hole in the adjoining wall and setup the darkbox such that the PMT could view the drum positioned at the far end of the hall; this setup is schematically shown in figure 3.13. From within the office the LED and associated data acquisition electronics are controlled over a local wifi network similar to how the drum calibration is performed at the FDs. A light baffle

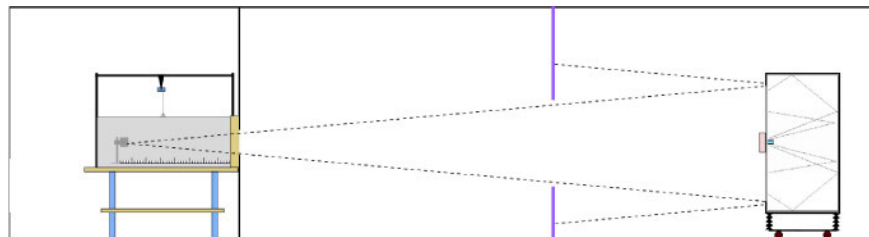


FIGURE 3.13. A schematic of the calibration space at the Auger Observatory campus showing the office housing the darkbox on the left and the adjoining 17m long dark hall housing the drum. The purple lines represent the reflection baffle placed halfway along the hall; the hole in the wall also serves as a baffle. Adapted from [123].

is positioned at the point of specular reflection in the dark hall to eliminate any reflections off the floor, ceiling and side walls seen by the PMT, and the hole in the adjoining wall also serves as a baffle. The reflections would cause a non $\frac{1}{R^2}$ attenuation.

The $\frac{1}{R^2}$ calibration procedure follows similar steps as what are outlined above. In the configuration shown in figure 3.13, the average response of the PMT to 5 μ s light pulses

from the drum at the large distance, ~ 16 m, is measured in units of ADC counts, H_{Drum} , represented by the blue square above the line in figure 3.17. Next, the LED light source is removed from the drum and the cylindrical Teflon diffuser is replaced with a 2 mm circular Teflon diffuser; this diffuser snout ensures that the LED is point-like to about 10 cm. With the 2 mm snout in place the LED is now in the “rail” light source configuration because it is now mounted on a rail setup, as shown in figure 3.14 where the centers of the drum, rail light source and the PMT are all on axis. Again the average response of the PMT to

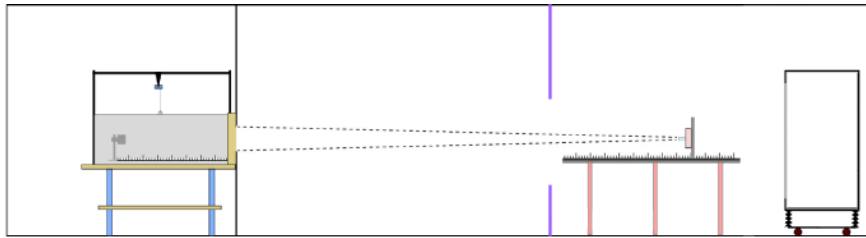


FIGURE 3.14. Schematic of the rail setup used in measuring the rail light source at varying distances from the PMT. From [123].

$5 \mu\text{s}$ light pulses from the rail light source are measured, but now the distance is varied from 15.25 m to 10.75 m, corresponding to six averages, H_i^{Rail} at six distances r_i ; these points are the red squares on the line in figure 3.17. The intensity of the rail light source is adjusted so that the six measurements span the drum measurement; this is done because the rail light source can not be setup at the drum distance because the drum is physically in the way, but more importantly it is a check on whether the drum intensity is within the linear response region of the PMT detection system. If the rail measurements are not within the linear response region there would be deviations from $\frac{1}{R^2}$, and as shown in the lower plot of figure 3.17 within uncertainties this is not the case.

Now the rail light source is moved into the darkbox and the PMT is replaced with the NIST calibrated photodiode, and the charge per pulse, Q_i , is measured using a Keithley 6514 electrometer at various distances, r_j from the photodiode. From the Keithley webpage

interface as shown above, the electrometer is set into “Q” mode where it samples the charge

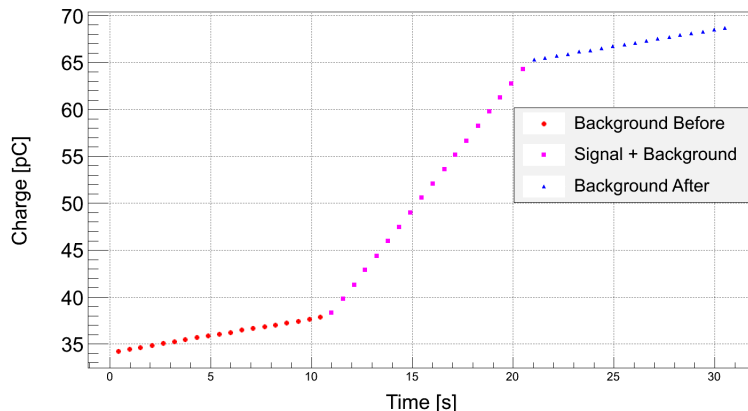


FIGURE 3.15. Example of how the NIST PD is measured with the Keithley. The charge is sampled at a specified rate, the background is measured for a given time, the red points, then the LED begins to flash and the charge builds up more quickly, the pink squares, and finally the background is measured again, the blue triangles.

on the calibrated photodiode at a given rate, and the measurement proceeds in three steps as shown in figure 3.15. The background charge is measured for a specified time, shown as the red circles in the plot, then the LED begins to flash and the electrometer continues to sample the charge from the photodiode, the pink squares, then finally the background is measured again, the blue triangles. The signal is calculated by subtracting off the background measured after the LED flashes, and then dividing the accumulated charge by the number of pulses from the LED. The LED is flashed with the exact same parameters (amplitude and width) as on the rail. The darkbox setup is shown schematically in figure 3.16. Inside the darkbox the light source is moved remotely using linear actuators that are accurate to 0.01 mm, and the average charge per pulse at the six distances are the black circles in figure 3.17 and are in absolute units of $[\frac{pC}{pulse}]$.

With the measurements described above, the drum radiant intensity, I_0^{Drum} , can be calculated in units of $[\frac{photons}{sr \times pulse}]$ using (3.5), where N_E^{Drum} and N_E^{Rail} are the total number of

photons emitted by the drum and rail light sources respectively, I_0^{Rail} is the radiant intensity

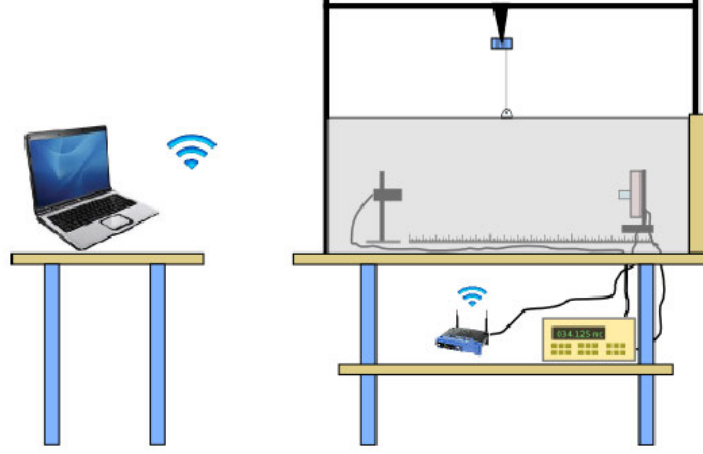


FIGURE 3.16. The darkbox configuration for the NIST photodiode measurements. The light source is mounted on linear actuators and can be positioned 10cm to 1m away from the photodiode. Taken from [123].

of the rail light source, and A_{PD} is the area of the photodiode mask provided by NIST. The omegas are where the wavelength dependencies of the detector responses and the emission spectra of the drum, and rail light source are integrated together.

$$I_0^{Drum} = \frac{N_E^{Drum}}{N_E^{Rail}} I_0^{Rail} = \frac{\langle Q_j \times r_j^2 \rangle}{\langle H_i^{Rail} \times r_i^2 \rangle} \times \frac{H^{Drum} \times r_D^2}{A_{PD} \times \Omega_{PD}^{Rail}} \times \frac{\Omega_{PMT}^{Rail}}{\Omega_{PMT}^{Drum}} \quad (3.5)$$

One can see that several factors of $(Response) \times (Distance)^2$ appear in (3.5) for each detector and source combination; these are constants for sources exhibiting $\frac{1}{R^2}$ behavior where the angled brackets indicate averages of these constants over the different distances. The $\frac{\langle Q_j \times r_j^2 \rangle}{\langle H_i^{Rail} \times r_i^2 \rangle}$ term is a ratio of photodiode response to the PMT response and is in units of $[\frac{C}{ADC_{counts}}]$, and serves a conversion factor for all PMT measurements in units of $[ADC_{counts}]$ to the absolute response of the photodiode in $[C]$. The factor is applied to every PMT response and causes the rail measurements to fall on the $\frac{1}{R^2}$ fit in figure 3.17 and the blue square drum measurement to be now in units of $[\frac{C}{pulse}]$. Note that the $\frac{1}{R^2}$ fit is applied to

the photodiode measurements, the black circles, only, and that the error bars in the lower plot are the statistical uncertainties associated with the data on the log-log plot and are not related to the fit.

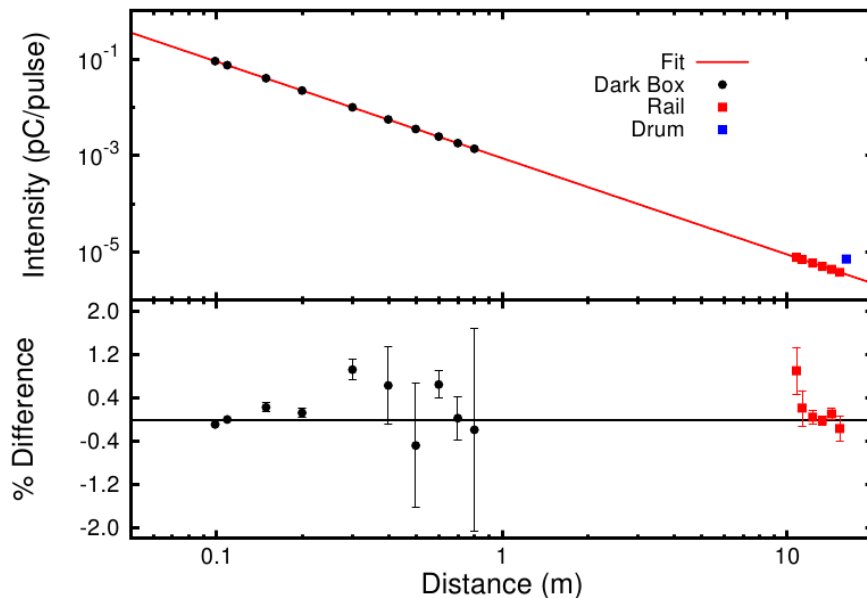


FIGURE 3.17. Responses from the PMT and photodiode to the drum and rail light sources, and percent differences from a $\frac{1}{R^2}$ fit applied to the black points only. The red points are the PMT response to the rail light source after being normalized and the blue point is the PMT response to the drum after being normalized. The lower plot shows the residuals from the fit, in percent, along with the statistical uncertainties associated with the points on the log-log plot; these error bars have nothing to do with the fit.

The omegas are defined as the integrals where the wavelength dependencies in the responses of the detectors and the emission spectra of the drum, and rail light sources are multiplied together. Ω_{PD}^{Rail} is the NIST calibrated response of the photodiode convolved with our measured emission spectrum of the rail light source. The ratio of the two integrals involving the response of the PMT and the PMT quantum efficiency, should equal 1 assuming that the emission spectra of the drum and the rail light source are the same. The ratio of these convolutions was calculated using the measured quantum efficiency of the PMT and the measure emission spectra of the drum, and rail light source and found to be 1.001.

Data shown in figure 3.17 are from 2013, and these values when used in (3.5) give $I_0^{Drum} = 5.70 \pm 0.12 \times 10^8$ [$\frac{\text{photons}}{\text{sr} \times \text{pulse}}$]. The uncertainties arising from the absolute calibration of the drum using the $\frac{1}{R^2}$ technique described above are described in detail in section 6 of [123] and are calculated to be 2.1%. Once the drum has been calibrated in the lab and the flux of emitted photons is known, the drum is then transported to the FD telescopes and the absolute calibration is performed.

3.3.2. ABSOLUTE CALIBRATION OF THE FLUORESCENCE DETECTORS. Absolute calibration of the fluorescence detectors relates a known number of photons incident on the aperture of the telescope to the output signal. The signal is measured in integrated ADC counts for each PMT in the FD camera that is triggered during a cosmic ray event.

There are two main methods for absolute calibration. The primary calibration is performed using the calibrated drum at each telescope, and the second method uses nitrogen laser mounted in the bed of a truck that is fired vertically from locations within the SD array [152].

Ideally, the drum calibration is performed once a year due to the logistics of calibrating the drum, and then transporting it to the 27 FD telescopes in the observatory. The procedure for the FD drum calibration is relatively simple. Once the absolute photon flux from the drum face is known, the drum is mounted into each telescope aperture, as shown in figure 3.9b, and the response of the telescope to 400, 5 μs drum light pulses is measured. Prior to the drum measurement, a relative Cal A is performed to measure the response of the camera before the absolute calibration, such that the drum calibration can be tracked over time using the Cal A system. Due to triggering the entire camera and reading out 440 traces for every drum pulse, the rate for the drum calibration pulses is limited to 1 Hz. Each telescope at a given FD building takes about twenty minutes to calibrate, and that time along with

the fifteen minutes it takes to reposition the drum in each aperture, means that in one night all six telescopes can be calibrated.

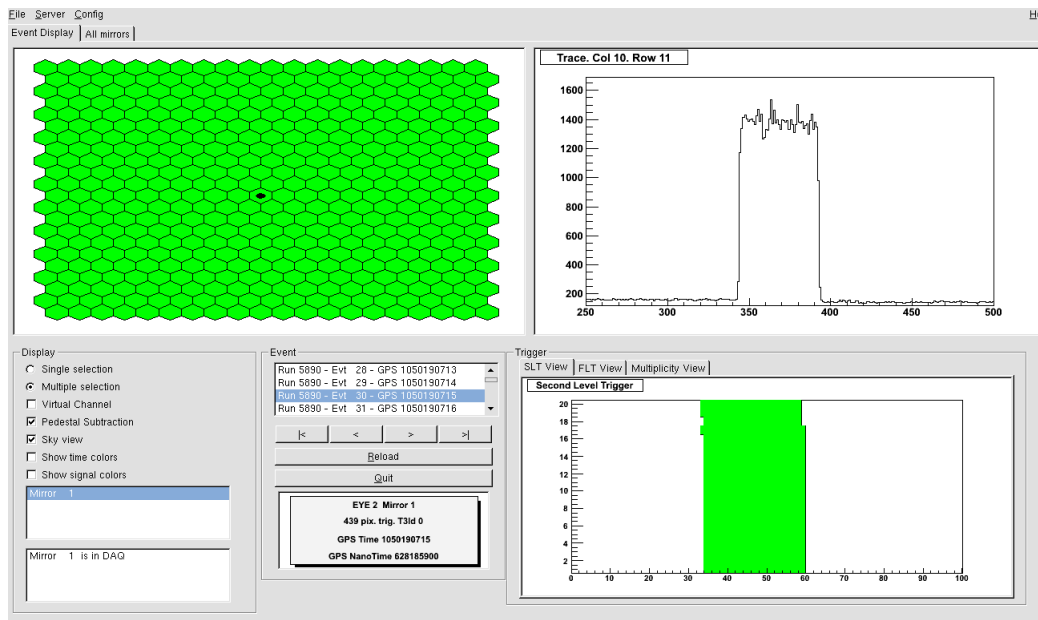


FIGURE 3.18. Response of one pixel in an FD camera to a $5 \mu\text{s}$ drum pulse.

Figure 3.18 is an event display showing the response of one telescope to a single $5 \mu\text{s}$ drum light pulse. A single pixel in the center of the camera is selected and the plot on the right of the figure shows the ADC count as a function of time bin, where each time bin is 100 ns.

Figure 3.19 shows the response of a telescope to a laser shot where the green pixels in the camera are the only ones to trigger, and typically these pixels will only be in a single column. The low number of pixels that are triggered is why it is infeasible to perform an absolute calibration using a vertical laser only, and why these laser calibrations are used as a cross check on the drum calibration. When using the laser as a calibration method the number of photons reaching the telescope aperture is derived from calculating the atmospheric attenuation on the side-scattered light using measured atmospheric profiles, and this leads to a 5.2% uncertainty in the laser calibration, for details, see [112, 153].

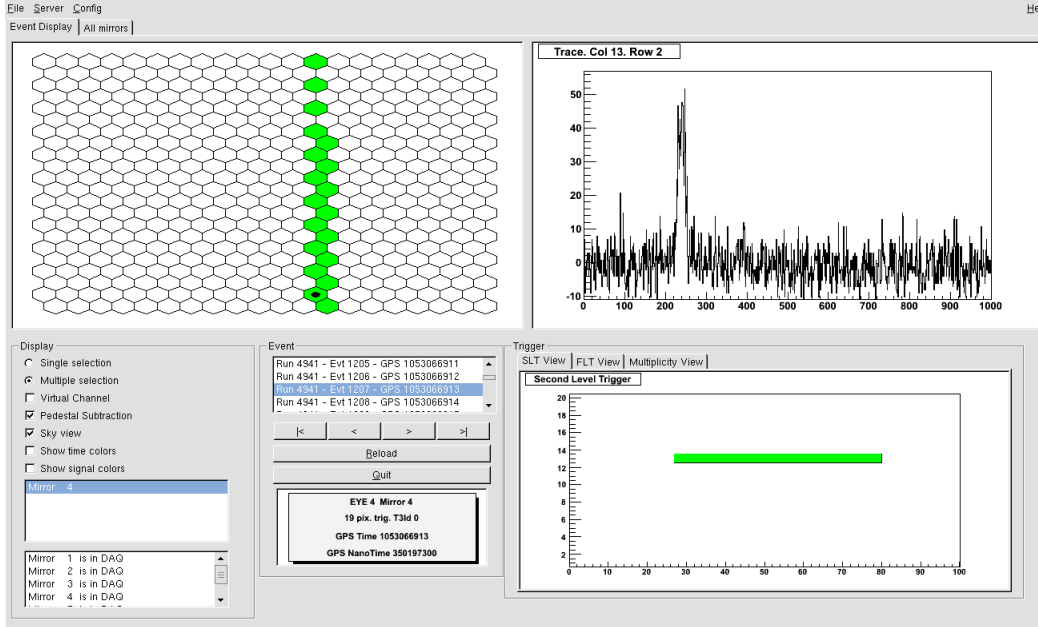


FIGURE 3.19. Response of an FD to a laser pulse, with one pixel selected showing its response.

The most recent absolute drum calibration campaign was performed in April 2013 after a catastrophic failure of the monochromator setup described in section 3.4. Prior to 2013, the last drum calibration was completed in June 2010 and a calibration constant of $\sim 4.5 \left[\frac{\text{photon}}{\text{ADC}} \right]$ was set for 24 telescopes, and since then the Cal A tracking of the June measurement was used to track the overall calibration of the FDs. The purpose of the April 2013 calibration was to test the tracking of the response of telescopes over a long-term, three year, period, and the predicted response of the 24 measured telescopes from the tracking was within 1% of the actual response measured from the drum calibration.

3.3.3. REDUCTION OF UNCERTAINTIES. The uncertainties associated with the absolute drum calibration directly affect the overall energy scale of the Auger Observatory measurements, and therefore reducing them is paramount to the success of the Observatory. Reducing the uncertainties by over a factor of two over the past ten years has been the main achievement of the calibration task, and was accomplished via two fronts, the absolute

calibration of the drum itself, and improvements of the DAQ and analysis of FD calibration data.

As detailed in [146], the uncertainties associated with the drum calibration totaled 6%, and the main contribution to this estimate arose out of transferring the response of the PMT with a 0.5 cm² mask to the response if there were no mask in place. The size of this region was dictated by the need to calibrate the beam using the 1 cm diameter NIST-calibrated photodiode. The LED drift mentioned in section 3.3.1.2 was not known at this time, and contributed an unknown systematic to the calibration. Section 3.3.1.3 outlines the improved drum calibration procedure that removed the need to transfer the photodiode effective area to the PMT photocathode due to the diffuse nature of all the light sources involved in the so-called $\frac{1}{R^2}$ calibration. This procedure also removed operating the LED in DC mode to diminish the LED drift, and the active temperature control within the updated electronics added further LED stability. In addition to these hardware improvements, the software used in analyzing the drum and FD calibration data, namely the analysis of the PMT traces, has been updated to account for after pulsing and AC-coupling effects.

With these improvements to the absolute drum and FD calibration, the uncertainty associated with the drum is now 2.1% [123], and the total uncertainty on the absolute FD calibration is 4%, a reduction from 9.5%.

3.4. THE MULTI-WAVELENGTH CALIBRATION

The nitrogen fluorescence induced by an EAS in the atmosphere covers a broad range of ultra-violet wavelengths from 250 nm to 450 nm with several prominent peaks from the 2P orbital and vibrational transition modes. Figure 3.20 shows the nitrogen fluorescence spectrum as measured by AIRFLY [136]. This spectrum is emitted isotropically near the

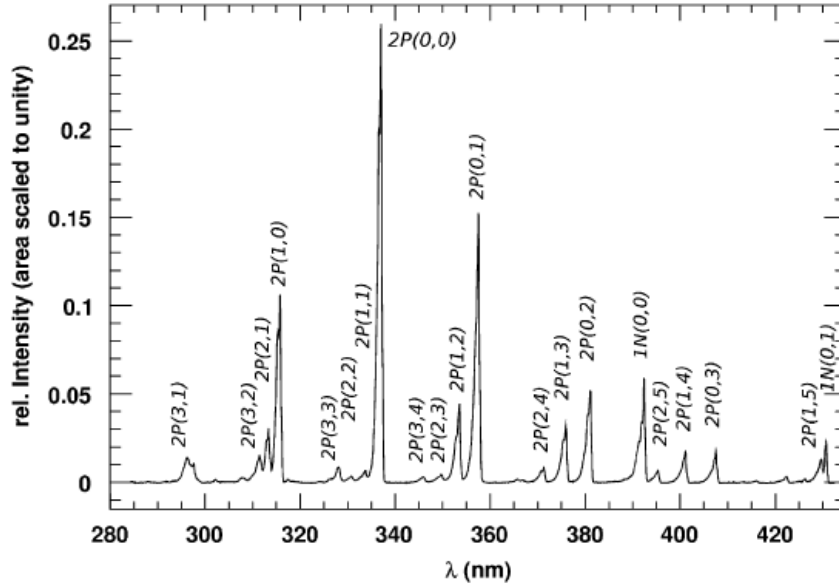


FIGURE 3.20. The nitrogen fluorescence spectrum as measured by AIR-FLY [136], where the peaks are shown with their transitions.

shower core, and travels through the atmosphere, attenuating as it travels. The purpose of the multi-wavelength calibration is to relate the signal measured by the FD to the spectrum of fluorescence light at its aperture. The multi-wavelength calibration measures the acceptance of the telescope as a function of wavelength and gives the efficiency across the broad nitrogen fluorescence spectrum.

As will be described in detail in Chapter 4, relating the number of nitrogen fluorescence photons at the telescope aperture to the signal from the telescope through the measurement of the telescope efficiency is needed for proper event reconstruction. Any change in the measured telescope efficiency will directly affect the measured energy in a given EAS because the efficiency is used to determine the number of photons incident on the telescope aperture per 100 ns time bin.

3.4.1. HISTORY OF THE MULTI-WAVELENGTH CALIBRATION. Initially the telescope efficiency was estimated from the convolution of individual components that make up the

telescope; this included the UV filter transmission, corrector ring transmission, mirror reflectivity, and the PMT quantum efficiency. The curve generated from this convolution gave the telescope efficiency as a function of wavelength and is shown in figure 3.21 as the black points near the bottom of the plot. Some data incorporated into this curve were measured

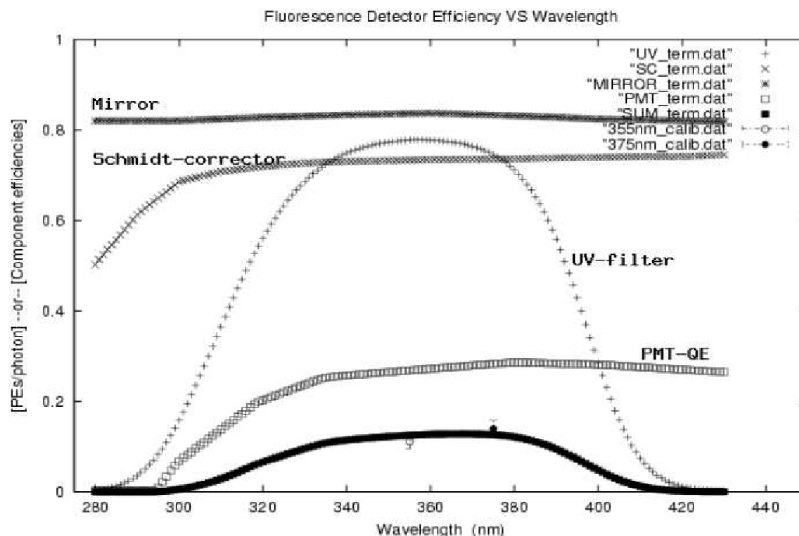


FIGURE 3.21. The initial estimate of the telescope efficiencies taken as the multiplication of the individual detector transmission and reflection efficiencies and the PMT QE referred to as the “piece-wise” curve, taken from [154].

by Auger collaboration members [154], others were the manufacturers’ nominal values, and this led to little or no information about the uncertainties associated with these data. The curve given by this multiplication method was named the “piece-wise” curve due to it being pieced together from the individual components, and it was the initial estimate of the telescope efficiency until an end-to-end measurement was performed. The piece-wise curve was implemented as the FD telescope response for every telescope in the array, all 27.

The first end-to-end measurement of the telescope efficiency was performed by the calibration group in 2006 using a modified drum setup that now used a xenon flasher as a broad UV light source. The same xenon flasher is used in the relative Cal B and C systems at the FD buildings. Five notch filters were used in a filter wheel mounted in front

of the flasher to select out wavelengths across the FD acceptance; then the light traveled into the drum via a light pipe and diffused throughout the drum uniformly illuminating the Teflon face. From this work [108] came the first end-to-end spectral measurement of the telescope efficiency, referred to as the “five-point” measurement, shown as the solid line in figure 3.22 compared to the piece-wise curve, where the FD efficiencies are relative to the efficiency at 380 nm. The efficiencies are taken relative to 380 nm because that was close to the absolute calibration wavelength, 375 nm, used at that time. The measured efficiency

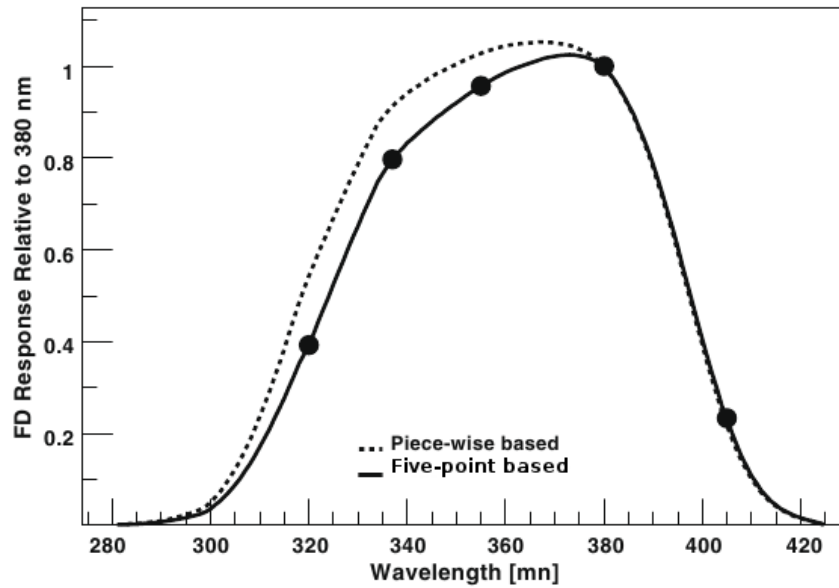


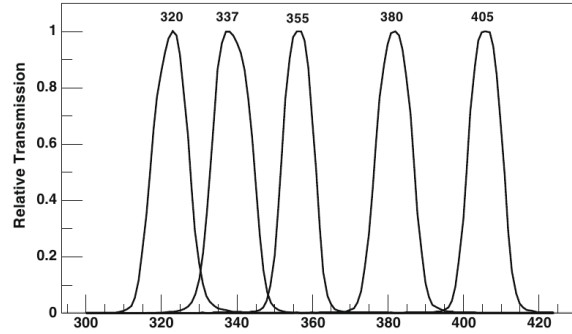
FIGURE 3.22. The initial piece-wise curve compared to the points measured in [108] in 2006, both are relative to the response at 380 nm.

showed a decrease in sensitivity below 380 nm, relative to 380 nm, than what was predicted by the piece-wise curve. The solid curve was realized after a complicated fitting procedure that used the piece-wise curve as a starting point and where the curve was constrained to go through the five measured points and assumed to go to zero at 285 nm and 425 nm. The description of implementing of the solid curve into the event reconstruction will be discussed in Chapter 4 along with its effects on measurements.

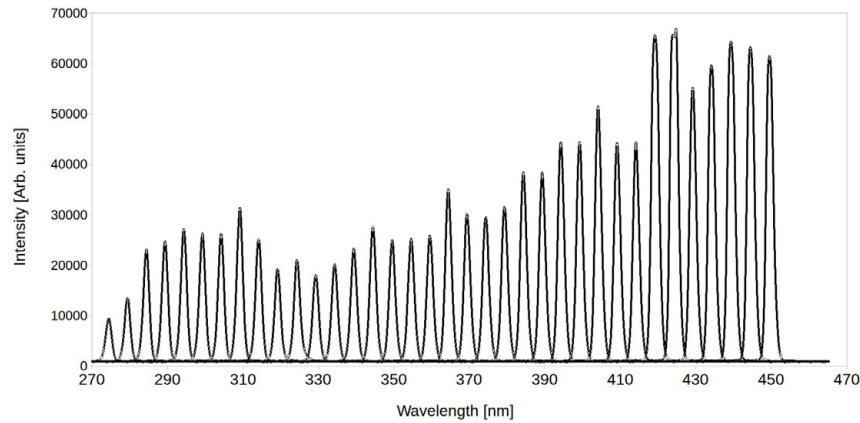
3.4.2. MONOCHROMATOR-BASED MULTI-WAVELENGTH CALIBRATION. While the notch filter measurement with the drum was the first end-to-end multi-wavelength calibration of the FD telescopes, it depended on the piece-wise curve for its initial guess for fitting based on the five points. The notch filters also had a wide spectral width, ~ 15 nm FWHM as shown in figure 3.23a, that complicated the deconvolution of these spectral widths on the falling and leading edges of the efficiency curve, as discussed in section 5.1 of [108]. There was also no measurement of where the FD response went to zero, it was assumed that below 280 nm and above 425 nm that it went to zero and the curve was constrained to meet these conditions.

These reasons are the motivation for using a monochromator [155] to select the wavelengths out of a UV spectrum. A monochromator allows for a high resolution probe across the FD acceptance, and a completely independent and far more detailed measurement can be performed. Figure 3.23b shows the xenon spectrum in 5 nm steps from 270 nm to 450 nm measured at the output of the monochromator, and shows the spectral output with a ~ 2 nm FWHM. A monochromator output width of approximately 2 nm was chosen, providing a reasonable compromise between wavelength resolution and the required drum intensity for use at the FDs, at most wavelengths.

The procedure for the calibration using the monochromator is similar to that of the measurement made with the notch filters, the FD responses to a number of flashes from the drum are averaged at 5 nm steps across the acceptance of the telescope, and then these points are normalized by a measured drum emission spectrum. While the procedure using the monochromator is simple, it does not depend on any previous work and gives the telescope response without complicated interpolation.



(A) Measured spectral output wavelengths of the five notch filters used in the first end-to-end multi-wavelength calibration, each normalized to one at their respective maximum intensity.



(B) The measured output wavelengths of the monochromator setup in 5 nm steps.

FIGURE 3.23. The selection of wavelengths compared for the notch filters above, and the monochromator below.

In order to make a more detailed multi-wavelength calibration using a monochromator, the drum must be modified for the monochromator based multi-wavelength calibration so that a temperature controlled box housing the monochromator and xenon light source can be mounted on the rear of the drum. To secure the environmental box to the drum, a mount was riveted onto the rear of the drum for supporting the monochromator setup. An Exelitas PAX-10 [156] pulsed Xenon light source was used as the input to the monochromator, and figure 3.24 shows the spectrum emitted by the flasher as measured with an Ocean Optics USB2000+ VIS/UV spectrometer [157].

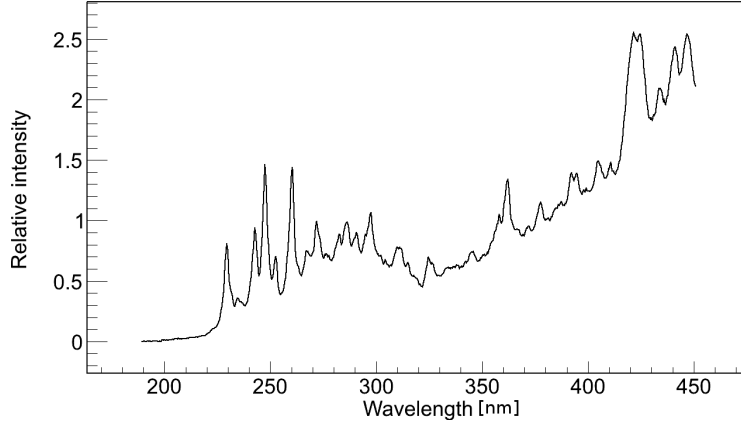


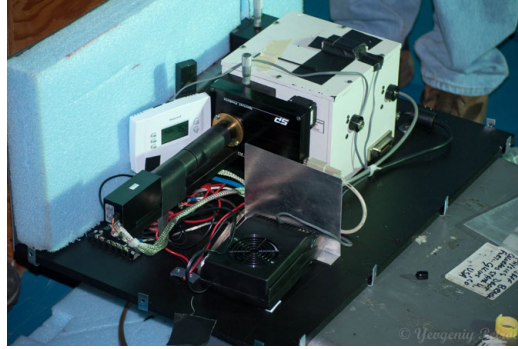
FIGURE 3.24. PAX-10 pulsed Xenon flasher emission spectrum, measured with an Ocean Optics USB2000+ VIS/UV spectrometer [157]. Intensities are normalized to one at 365nm

The light from the xenon lamp was focused onto the input slit of the monochromator using the same F/4 optics as the monochromator. We varied the input slit of the monochromator between $10\ \mu\text{m}$ and fully open at $3000\ \mu\text{m}$ to achieve a bright enough intensity for the PMT in the lab; the output slit was set to $200\ \mu\text{m}$ in order to achieve the narrowest spectral output at a given wavelength, $\sim 2\ \text{nm}$ FWHM, see figure 3.23b.

This whole setup was housed in an insulated box with a small heater with a temperature control circuit that monitored and kept the temperature inside the box at $20 \pm 2\ \text{°C}$, even with ambient temperatures near $0\ \text{°C}$. The box was installed onto the back of the drum with the output of the monochromator fitted with a custom 1" diameter aluminum snout that protruded into the interior of the drum, and on the end of the snout we attached a thin, 0.009" Teflon diffuser, see figure 3.25c for a picture of the snout and diffuser.

We then tested the face of the drum to ensure uniform illumination using the monochromator setup. We took several long exposure, ~ 10 minutes, CCD images of the front Teflon face and found it to be uniformly emitting.

The monochromator and xenon flasher are controlled with the same CSU-developed cgi-based web page interface and calibration electronics that have been used with success in the



(A) Components inside the box: heater, thermostat, monochromator, xenon flasher and optics.



(B) Environmental box mounted on the rear of the drum.



(C) Snout that is inserted into drum, Teflon diffuser mounted on end

FIGURE 3.25. The monochromator environmental box setup and placement on the rear of the drum

absolute drum calibration. Scanning of the monochromator, triggering of the flasher, and data acquisition from monitoring devices and the FD are all fully automated using cgi code and cURL [158] scripts over the wireless LAN used for drum calibrations.

After the initial monochromator-based multi-wavelength calibration campaign in August 2011, the FD efficiencies we measured at Los Leones bay three and four had nearly a 40% drop from 390 nm to 340 nm compared to the five-point measurement. During this time it was assumed that the drum had no large effect on the output spectrum of the monochromator since previous measurements of the reflection and transmission of the drum materials, Tyvek

and Teflon, showed little dependence on wavelength. The anomalous efficiencies we measured at the FDs meant a re-examination of these materials looking for wavelength dependencies, but all measurements made at CSU showed no large wavelength dependent effects. In November 2011 the transmission and reflection properties of the drum itself in Malargue were measured and we discovered what had led to the changed FD efficiency measurement. The reflectivity of the Tyvek from the interior of the drum had a large decrease below 390 nm, roughly 40% as shown in figure 3.26.

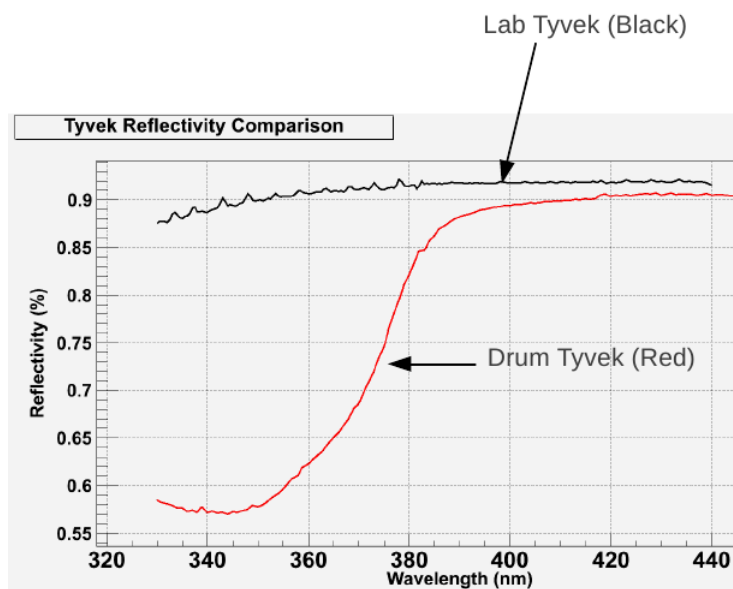


FIGURE 3.26. A relative plot of the Tyvek reflectivity. The black curve is a measurement performed on the very same Tyvek that was initially used to construct the drum. The red curve is a measurement of a piece of Tyvek removed from the interior of the drum. The y-axis is relative as each measurement was performed using a different technique, the main thrust of the plot is the drastic decrease below 380 nm of the red curve.

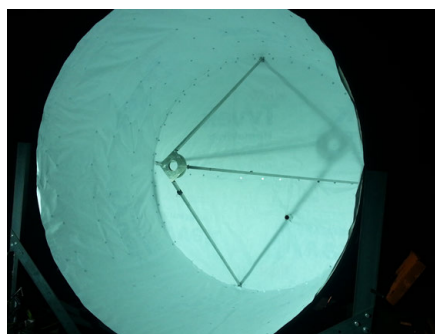
This decrease in reflectivity had not been noticed before because the absolute calibration is performed at a single wavelength, 365 nm, and the drum is calibrated at this wavelength just prior to an FD calibration. In the previous multi-wavelength calibration the relative intensity of the drum was measured at the five notch filter wavelengths, and these intensities were divided out of the FD responses. The relative intensities of the drum in August 2011

were not measured because the monochromator control and data acquisition were not yet automated, and thereby precluding a measurement of the relative drum spectrum in a timely and reliable fashion. With an unknown relative drum emission spectrum nothing could be done with the FD efficiencies measured in 2011.

The next attempt at the multi-wavelength calibration took place in April 2013. To remedy the Tyvek reflectivity problem we relined the interior of the drum Tyvek using rivets to attach it instead of glue as shown in figure 3.27. In addition the software controlling the



(A) New Tyvek secured with rivets on the top half of the rear wall of the drum.



(B) Interior of the drum fully lined with new Tyvek.

FIGURE 3.27. Interior of the drum being relined with new Tyvek in April 2013 using rivets

monochromator had been improved such that everything was fully automated, and we could measure the relative drum emission spectrum in the dark hall prior to the FD calibration, and then use this spectrum in the efficiency calculation. The automated relative intensity measurement of the drum as a function of wavelength would account for any further change that may take place with the spectral output of drum.

Shortly into the April 2013 calibration, after taking data at Los Leones bays three and four, the monochromator suffered a hardware failure, and we could not continue with the multi-wavelength measurements. After the monochromator failure the most recent absolute calibration described in section 3.3 was performed.

Since the attempt in April, 2013, we replaced the monochromator with an upgraded model of the same type and further improved the data acquisition and analysis. We also improved the hardware reliability such that we would have redundant monitoring of the monochromator output and drum spectrum using a monitoring photodiode (PD) just downstream of the monochromator output and a PMT observing the interior of the drum called the Drum PMT. In March, 2014 we performed the multi-wavelength calibration at eight FD telescopes using the new monochromator and the updated data acquisition and monitoring.

3.4.3. THE MULTI-WAVELENGTH DRUM EMISSION SPECTRUM. With the automated scanning of the monochromator and data acquisition we were able to take several measurements of the relative drum emission spectrum as viewed by the monitoring devices and our calibration Lab PMT. The setup for these measurements had the drum at the far end of the dark hall and the Lab PMT inside the darkbox in the calibration room, about 16 m away from the Teflon face of the drum, similar to the first measurement in the drum calibration explained in section 3.3.1.3. Additionally, see [123] for a detailed description of the dark hall calibration setup. The monitoring detectors were located as described above. Our data acquisition system can only read in two detectors at once, so we would switch between reading one of the two PMTs, the Drum PMT or the Lab PMT, while continuously reading in the PD.

The average response of the Lab PMT to 100 pulses of the drum was recorded as a function of an integer wavelength from 250 nm to 450 nm. The statistical uncertainty in the average for a given wavelength was calculated as the standard deviation of the mean. Over the course of our time in Malargüe during March 2014 we measured four drum spectra in this fashion, and an example of one of these is shown in figure 3.28. The four spectra were measured over a week, two prior to any field work at the FDs and then after calibration at

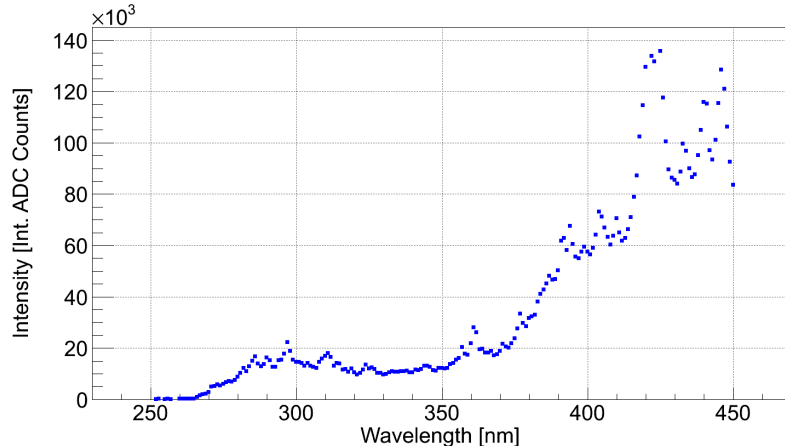


FIGURE 3.28. A measured drum emission spectrum taken with our Lab PMT prior to any field work on March 19th. Each point is the average response of the PMT to 100 pulses at that wavelength and the error bars, which are not visible on the plot, are the $\frac{\sigma_{Drum}}{\sqrt{100}}$ for those measurements.

Los Morados and again after calibration of Los Leones on the final day in Malargüe.

In the end we took averages of these four spectra at each wavelength as the final measurement of the drum spectrum because this approach would average out any changes that may have occurred during calibration at the FDs, and took the uncertainty for a given wavelength as the standard deviation in the four measurements over the square root of four. Using the average also allowed us to estimate the systematic uncertainty on the drum spectrum. The averaged spectrum is shown in figure 3.29, where this final spectrum was evaluated in steps of 5 nm corresponding to the step size used when calibrating the FDs, and the data at four intermediate wavelengths are ignored. For wavelengths between 320 nm and 390 nm, the spread in the four measurements was statistically consistent where the statistical uncertainty was calculated as the spread of the 100 measurements for each separate calibration at that wavelength, but for wavelengths at the low and high ends of the spectrum there was disagreement; section 3.4.5 explains how we introduce a systematic uncertainty to account for this disagreement.

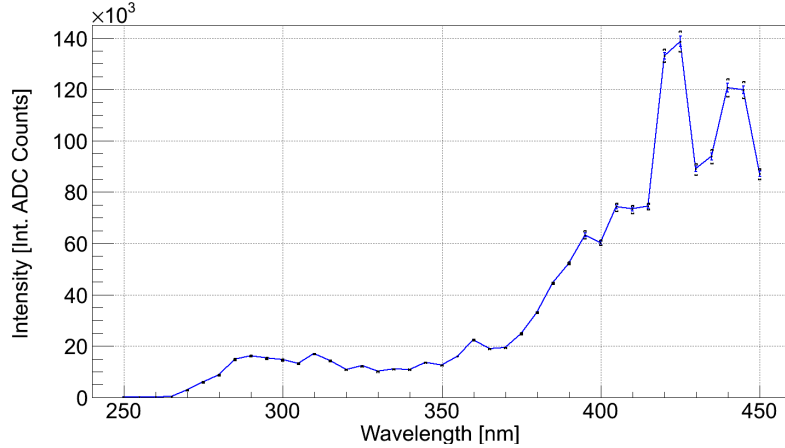


FIGURE 3.29. The averaged drum spectrum as measured using the Lab PMT throughout the calibration campaign. The spectrum is shown in steps of 5 nm as this is what is used to measure the FD responses. The uncertainties are calculated for a given wavelength as the $\frac{\sigma_{Drum}^{Avg}}{\sqrt{4}}$ for the four independent spectra, and the brackets are the systematic uncertainties.

For each of these four spectra measured with the Lab PMT we have data from the monitoring PD. The monitoring PD data were handled in the same way, where we made an average of the four spectra recorded by the PD and an associated error based on the spread of the four measurements; these data are shown in figure 3.30. We also used the PD

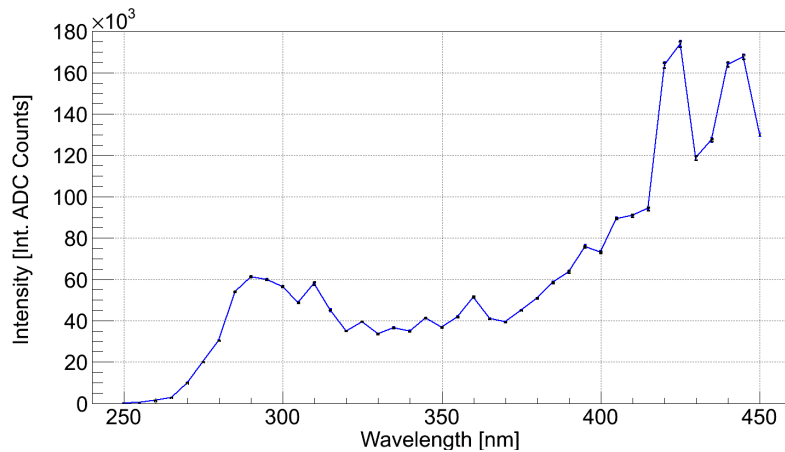


FIGURE 3.30. Average spectrum from four monitoring PD spectra measured at the same time as the Lab PMT spectra were taken. Statistical and systematic error bars are shown at each point, but are too small to see at this scale.

spectra to normalize the Lab PMT measurements to further account for any changes in the spectrum. The black brackets that are barely visible in the Lab PMT and PD spectra are the estimated systematic uncertainties for each wavelength.

The spectra in the above plots look different for the Lab PMT and PD because these data do not have the individual detector responses unfolded from the measurements. We measured the quantum efficiency of the Lab PMT along with its associated uncertainty, and these are divided out in the final calculation of the FD efficiency as described in section 3.5.

These measured spectra from the different detectors, the Lab PMT and the monitoring PD, are used in the calculation of the FD efficiency, and the uncertainties associated with these measurements are described below.

3.4.4. LAB PMT QUANTUM EFFICIENCY. Measurement of the PMT quantum efficiency (QE) for the Lab PMT used to measure the relative drum emission spectrum was performed at CSU prior to the multi-wavelength calibration campaign. The method was similar to what was done previously [108], except we used the xenon flasher as the UV light source for the monochromator in order to utilize the DAQ software and data analysis that have been developed for the multi-wavelength calibration.

The PMT QE measurement benefited greatly from the software developed for the absolute and multi-wavelength calibrations. The Keithley measurements, as explained in section 3.3.1.3, are much more accurate than the methods used previously. In order to use them with the QE measurement they had to be automated such that the monochromator could scan through the wavelengths and the Keithley could measure the charge per pulse of the xenon flasher at each wavelength. Implementing the Keithley scanning was straightforward using cURL scripts. Then, with a fully operational electronics package, one could read in the Lab PMT and a monitoring photodiode simultaneously, and then the NIST photodiode

(via the Keitley), in a scan through the specified wavelength range. An example of one of the numerous PMT QE measurements is shown in figure 3.31, where the scan was over 200 wavelengths from 250 nm to 450 nm, with 500 pulses at each wavelength, and the Lab PMT, the red triangles, and monitoring photodiode, the blue squares, were read in simultaneously.

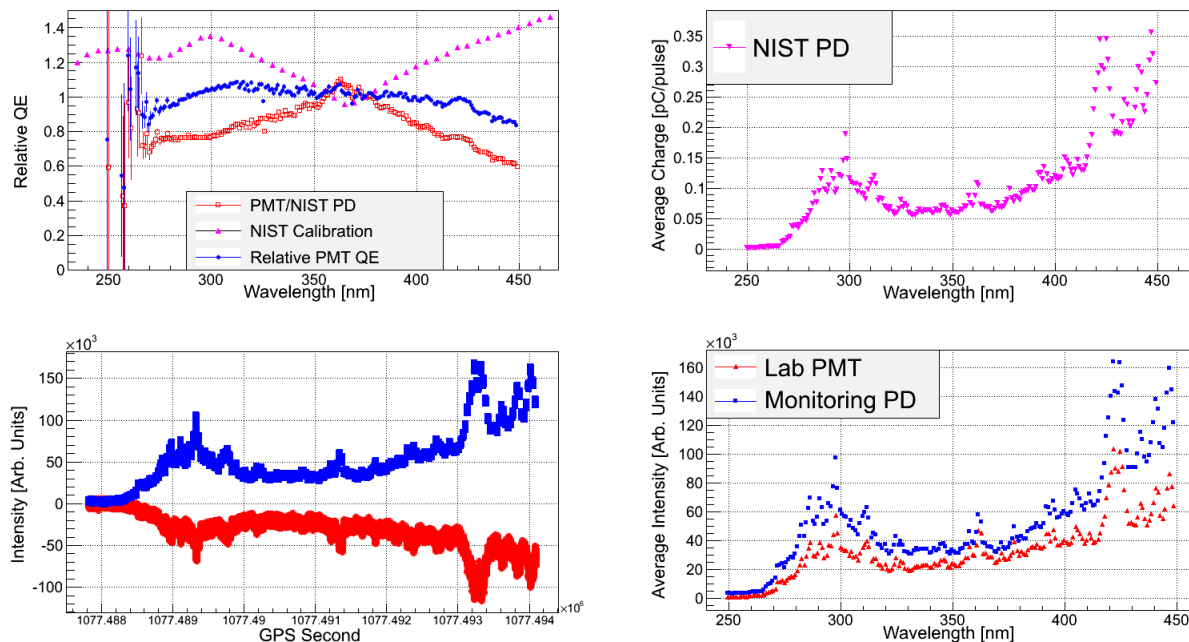


FIGURE 3.31. An example of data taken during a relative QE measurement. The lower plots are the responses of the Lab PMT as red triangles, and a monitoring photodiode as blue square to 500 pulses of the xenon flasher at each wavelength. The upper right plot is the charge per pulse as measured by the NIST calibrated photodiode viewing the same number of flashes. The upper left plot shows the calculation of the QE, shown as blue circles, where the Lab PMT data are divided by the NIST charge per pulse then divided by the NIST calibration, all as a function of wavelength.

Data from the NIST photodiode, the pink data, were taken shortly after using the same number of pulses at each wavelength. The relative QE is then calculated as a function of wavelength by taking the Lab PMT data and dividing it by the NIST photodiode data, these ratios for each wavelength are the red squares in the upper left plot, then taking these data and dividing them by the NIST calibration data, shown as pink triangles in the same plot,

giving the relative QE shown as blue circles. All of these data are normalized relative to their values at 375 nm, since we only required to have a relative QE curve.

With these changes and improvements we found a QE that was within one sigma of the previously published work [108]. For our purposes of using the Lab PMT to measure the relative drum emission spectrum, we only needed a relative measurement of the QE, and so certain uncertainties associated with an absolute QE measurement are not included in this work.

Several measurements of the Lab PMT QE were performed prior to and after the March 2014 multi-wavelength calibration campaign, and all of the measurements yielded data consistent with the black squares shown in figure 3.32. The error bars are the statistical un-

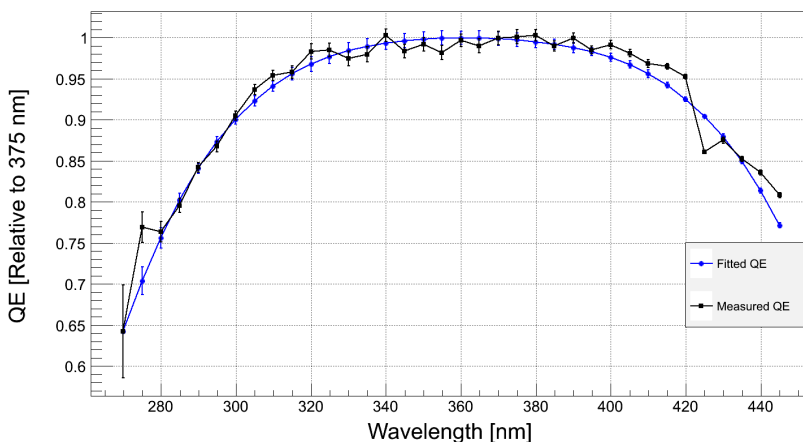


FIGURE 3.32. Shown in black is the measured relative Lab PMT QE where the measurement was performed at CSU using the same xenon flash lamp and monochromator as used in the multi-wavelength drum. The error bars are the statistical uncertainty associated with the distribution of the response of the PMT at each wavelength. The blue curve is a fourth order polynomial fit to the data that serves to smooth out the measurement.

certainty associated with the spread in the response of the PMT to 100 pulses at each wavelength. The measured variations in the curve are due to the variations in the intensity of the xenon flash lamp coupled with the peaks in the xenon spectrum at those wavelengths, and in an attempt to remove these peaks, we fit the PMT QE curve with a fourth order

polynomial shown as the blue circles in the figure. The error bars in the fit are the relative statistical uncertainty for a given wavelength applied to the interpolated values in the fit.

3.4.5. UNCERTAINTIES IN LAB MEASUREMENTS IN MALARGÜE. The uncertainties associated with the lab measurements were estimated using the statistics from the distributions of detector responses at each wavelength, and then systematics were evaluated by comparing the measured drum emission spectra.

3.4.5.1. *Statistical Uncertainties.* The estimate of the statistical uncertainties for the various response distributions to the xenon flasher are taken as the standard deviation of the mean. Figure 3.33 shows the response distribution of the Lab PMT to 100 flashes of the drum where $\delta_{PMTStat}^{Drum}(\lambda) = \frac{\sigma(\lambda)}{\sqrt{N}} \approx 1\%$. The intensity at the monochromator output is known to be stable through the monitoring PD spectra taken at the same time as the

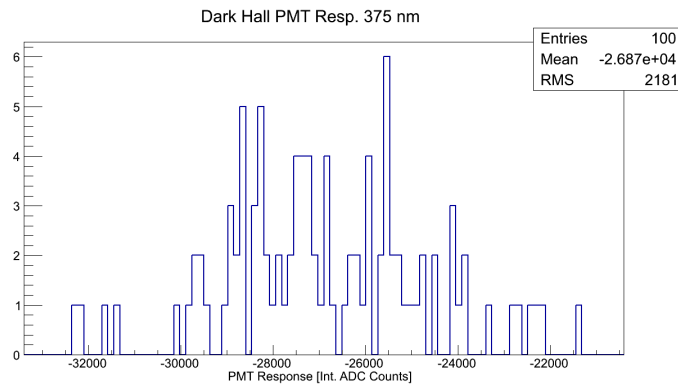


FIGURE 3.33. Distribution of the response of the Lab PMT to 100 flashes of the drum at 375 nm.

Lab PMT; the $\delta_{PMTStat}^{Drum}(\lambda)$ are independent uncertainties associated with the Lab PMT. A similar distribution was produced for each wavelength in the Lab PMT QE measurement and gives $\delta_{PMTQE}^{Drum}(\lambda) \approx 1\%$.

3.4.5.2. *Systematic Uncertainties in Lab Measurements.* Estimating the systematic uncertainties associated with the relative drum emission spectrum measurement is done by

comparing the different drum emission spectra measured by the Lab PMT over the course of more than a week. Shown in the top of figure 3.34 are the four spectra measured by the Lab PMT that are used to calculate an average spectrum of the drum, and the middle plot shows the residuals from the average in percent as a function of wavelength.

Over most of the wavelength region where the FD efficiency is nonzero, 300 nm to 420 nm, the residuals plotted in the middle plot of figure 3.34 agree with each other within the statistical uncertainties, but they do differ. To estimate the systematic at each wavelength we introduce an additive parameter, $\varepsilon_{Syst}^{Drum}(\lambda)$, such that minimizing a χ^2 comparison of the Lab PMT response at a given wavelength, $S^{Drum}(\lambda)$ and its associated statistical uncertainty, $\delta_{PMTStat}^{Drum}(\lambda)$, to the average spectrum, $\overline{S^{Drum}}(\lambda)$ and its associated statistical uncertainty based on the spread in the four Lab PMT measurements, $\delta_{Stat}^{\overline{Drum}}(\lambda)$, gives $\chi_{ndf}^2 \leq 1$, and then this parameter is taken as the systematic uncertainty, as calculated via (3.6).

$$\chi_{ndf}^2(\lambda) = \sum_{n=1}^4 \frac{(S^{Drum}(\lambda)_n - \overline{S^{Drum}}(\lambda))^2}{(\delta_{PMTStat}^{Drum}(\lambda)_n)^2 + (\varepsilon_{Syst}^{Drum}(\lambda))^2} \leq 1 \quad (3.6)$$

Prior to the comparison, the Lab PMT data are normalized by the contemporaneous PD data at each wavelength to account for changes in the monochromator emission spectrum. We do not use the data collected by the Drum PMT for normalizations because the PD data are much more consistent as a function of time. The drum PMT suffered from poor grounding on its power supply while in the field, and this led to the data having noisy and inconsistent baselines that made analysis of the traces prohibitively difficult. The PD spectra are treated with a similar evaluation of a systematic at each wavelength, and these systematics are the black brackets shown in figures 3.29 and 3.30, but are not visible for

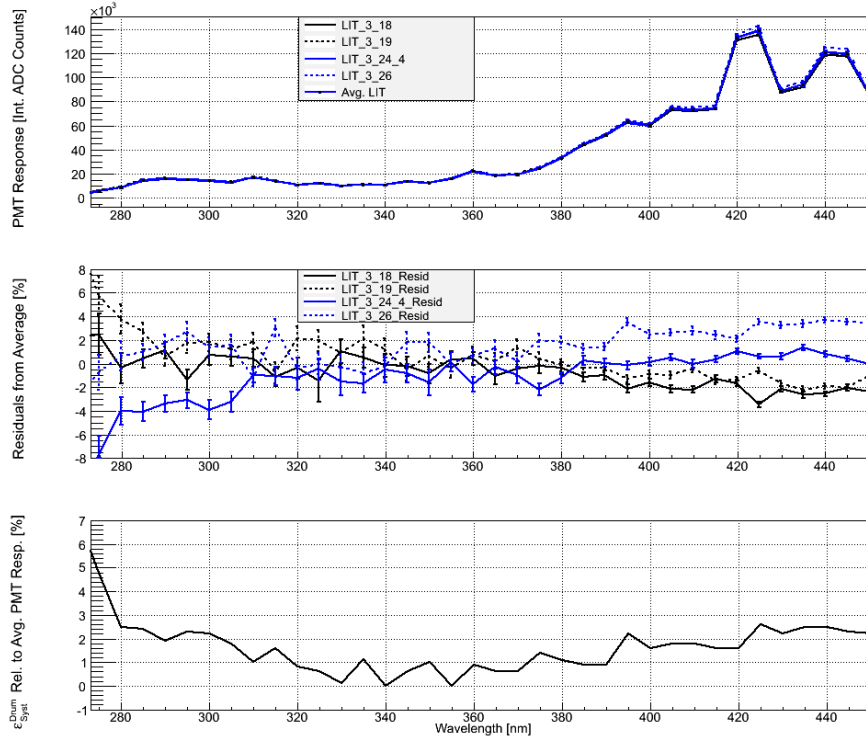


FIGURE 3.34. Plots of the four drum emission spectra as measured by the Lab PMT and the residuals from the average in percent, then a plot of $\epsilon_{Syst}^{Drum}(\lambda)$ shown as the size of the PMT response at a given wavelength in percent.

most of the data. The non-zero Lab PMT systematics vary from $< 1\%$ to $\approx 3\%$ and those for the PD are all $\lesssim 1\%$.

3.4.6. MULTI-WAVELENGTH CALIBRATION OF THE FLUORESCENCE DETECTORS. As described in Chapter 2 the Auger Observatory fluorescence detectors have two types of mirrors, but there are also two types of glass used in the corrector rings. Schott Glass [159] manufactured both types of corrector rings, Borofloat 33 [160], and P-BK7 [161]. The four different types of detector components means that there are four possible combinations of mirrors and corrector rings that make up all the FD telescopes. The multi-wavelength calibration should be performed on all the combinations due to the different possible wavelength dependencies associated with each component, but even with the automation of the monochromator and data acquisition, we were able to measure only two bays at an FD

building in a night. With the aim to measure all possible combinations of components, we selected a subset of the FD telescopes that would accomplish this; table 3.1 shows the eight telescopes with their associated mirror and corrector ring type. We measured the response

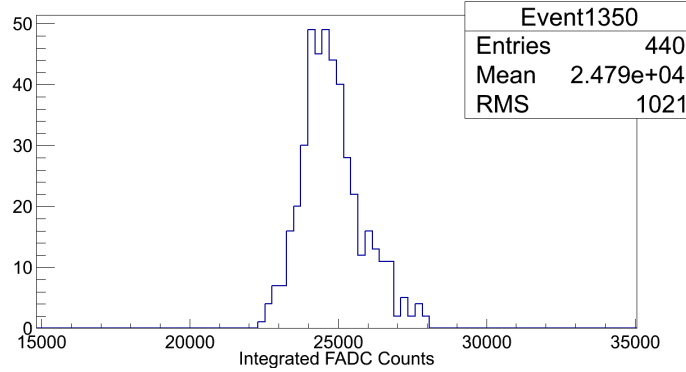
TABLE 3.1. Table of the FDs visited during the March, 2014 multi-wavelength calibration, and their respective components.

FD	Mirror Type	Corrector Ring
Coihueco 2	Glass	BK7
Coihueco 3	Glass	BK7
Coihueco 4	Glass	Borofloat 33
Coihueco 5	Glass	Borofloat 33
Los Morados 4	Aluminum	Borofloat 33
Los Morados 5	Aluminum	Borofloat 33
Los Leones 3	Aluminum	BK7
Los Leones 4	Aluminum	BK7

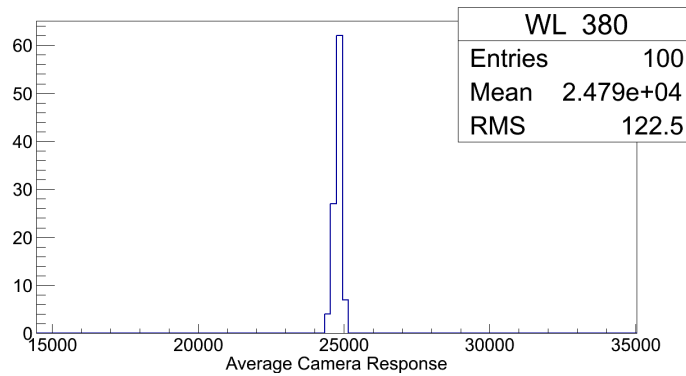
of these eight telescopes over the course of five days, with checks on the drum emission spectrum in the dark hall after the third day, and after the final day at Los Leones.

3.4.7. UNCERTAINTIES IN FD MEASUREMENTS. Similar to the lab work, the statistical uncertainties are estimated from the distributions of camera pixel responses, then the average of the camera response. Unlike the lab work, we did not have multiple measurements to examine for systematics, but we developed a comparison between the similarly constructed telescopes and derive a systematic.

3.4.7.1. *Statistical Uncertainties.* The procedure for measuring the telescope response to the multi-wavelength drum was to first scan from 255 nm to 445 nm in steps of 10 nm, and then scan from 250 nm to 450 nm in steps of 10 nm. A full telescope response would then be an interleaving of these scans where each scan nominally took about an hour to complete. At each wavelength a series of 100 pulses from the drum was recorded by the FD DAQ in calibration mode at a rate of 1 Hz. A histogram of the response of the 440 pixels to one flash of the drum at 380 nm is shown in figure 3.35a, and figure 3.35b is a



(A) Histogram showing the responses of the 440 pixels to one pulse of the drum at 380 nm.



(B) Histogram showing the camera response, all 440 PMTs/pulse, to 100 pulses of the drum at 380 nm.

FIGURE 3.35. Histograms of the pixel response and camera response.

histogram of the average response of the 440 pixels, or camera-averaged, to the 100 pulses for the drum at 380 nm. The spread in the response of the 440 pixels to one flash of the drum is much greater than the spread in the average response of the camera to 100 flashes of the drum for a given wavelength. The pixel spread is on account of the drift of the gain in the individual pixels after the so-called flat-fielding as described in [93], where the pixels have been observed to drift from a $\pm 0.3\%$ spread to $\pm 3\%$ over six months. The observed drift is expected from power cycling the camera, and the exposure of the PMTs to ambient starlight during data-taking. We want to develop a single calibration constant for the entire camera

at a given wavelength, so we need a way to measure a systematic uncertainty associated with this spread in pixel response; see section 3.4.7.2 for the evaluation of this uncertainty.

During the scan the monitoring data from the Drum PMT and the monochromator PD were analyzed on the fly and checked for inconsistencies as compared to the lab measurements made in the dark hall. After the completion of a scan we analyzed the FD data and produced a raw response for the FD with the average camera response along with a statistical uncertainty based on the standard deviation of those averages, $\delta_{FD}(\lambda) = \frac{\sigma_{FD}^{cam}(\lambda)}{\sqrt{100}}$, at each wavelength. Shown in figure 3.35b is an example of the camera-averaged response distribution to 100 pulses of the drum where $\delta_{FD}(\lambda) < 1\%$.

3.4.7.2. *Systematic Uncertainties.* The systematic associated with the FD responses is more complicated than the drum spectrum because we do not have several measurements of a single FD to compare and derive an uncertainty. The first systematic is evaluated by examining the spread in the responses of the 440 pixels that make up the telescope camera. As shown in figure 3.35, the spread in the pixels is larger than the spread in the camera response to 100 flashes of the drum. Since we want a single calibration constant at each wavelength for a given camera we estimate a systematic associated with the spread in the pixels for each wavelength. We take the 100 averages of the 440 pixels at each wavelength, $\mu^{440}(\lambda)$, and the statistical uncertainty on those averages based on the spread of the pixels across the camera, $\sigma^{440}(\lambda)$, and perform a χ^2 comparison between the averages of the pixels to the final average obtained from those 100 camera-averages, $\mu_{cam}(\lambda)$. We then introduce a parameter such that at each wavelength the $\chi_{ndf}^2 \leq 1$ for $ndf = 99$, and this parameter is then an estimation of the systematic as a function of wavelength, $\sigma(\lambda)_{Syst}^{FD}$. The expression (3.7)

is calculated at each wavelength.

$$\chi_{ndf}^2(\lambda) = \sum_{n=1}^{100} \frac{\left(\mu^{440}(\lambda)_n - \mu_{cam}(\lambda)\right)^2}{\left(\frac{\sigma^{440}(\lambda)}{\sqrt{440}}\right)_n^2 + \left(\sigma(\lambda)_{Syst}^{FD}\right)^2} \leq 1 \quad (3.7)$$

A plot of $\sigma(\lambda)_{syst}^{FD}$ for Coihueco bay four is shown in figure 3.36 where the systematic is shown as a percentage of the FD response value at that wavelength. The evaluation of $\chi_{ndf}^2(\lambda) \leq 1$ at each wavelength using (3.7) only requires a non-zero value for $\sigma(\lambda)_{syst}^{FD}$ for a few wavelengths. The data shown for Coihueco bay four have a particularly low number of

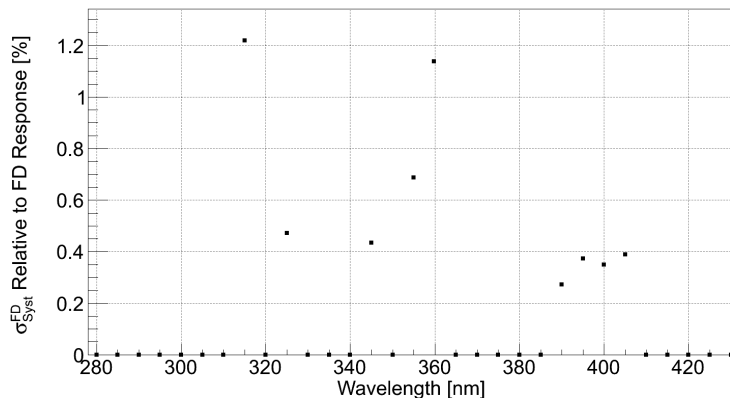


FIGURE 3.36. The systematic $\sigma(\lambda)_{syst}^{FD}$ calculated for Coihueco bay four. The y-axis is the size of the systematic relative to the FD response at that wavelength in percent.

non-zero values for the systematic, with the other measured FDs having up to twenty non-zero values. Additionally, we also make use of the two responses measured for telescopes with the same components.

3.4.7.3. *FD Systematics Evaluated by Comparing Similar Telescopes.* If we assume that the FDs with like components, the same mirror and corrector ring types, should give similar responses, we can make a comparison between them and determine how different they are. To that end we perform a χ^2 test between them and introduce parameters to minimize the χ^2 such that $\chi_{ndf}^2 \leq 1$ for $ndf = 34$, where there are 35 wavelengths used in the comparison.

The parameters introduced are a scale factor β that is applied to one of the FD responses, and then ε_{FD} , which is an estimate of a systematic that would be needed to account for the difference between the two telescopes, such that the raw response of one of the FDs as a function of wavelength is then $\beta * (FD_{Resp}(\lambda) \pm \delta_{Stat}^{FD}(\lambda) \pm \sigma_{Syst}^{FD}(\lambda) \pm \varepsilon_{FD})$ for one of the telescopes in the comparison. The scale factor accounts for any overall difference in response between the two telescopes; this is similar to performing a Cal A analysis between the respective bays, and is allowable because the wavelength-dependent FD efficiency is a relative measurement.

The minimization is done in two steps according to (3.8) where the sum is over the N_λ measured wavelength points.

$$\chi_{ndf}^2 = \sum_{n=1}^{N_\lambda} \frac{\left(FD_1(\lambda)_n - \beta * FD_2(\lambda)_n \right)^2}{\left(\delta_{Stat}^{FD_1}(\lambda)_n \right)^2 + \left(\sigma_{Syst}^{FD_1}(\lambda)_n \right)^2 + \left(\beta * \delta_{Stat}^{FD_2}(\lambda)_n \right)^2 + \left(\beta * \sigma_{Syst}^{FD_2}(\lambda)_n \right)^2 + \left(\beta * \varepsilon_{FD} \right)^2} \quad (3.8)$$

$$\leq 1$$

First a minimum in χ_{ndf}^2 is found by setting $\varepsilon_{FD} = 0$ and allowing the scale factor β to vary, as shown in the left side of figure 3.37. Once β has been determined, ε_{FD} is allowed to vary until $\chi_{ndf}^2 \leq 1$, this is shown on the right side of figure 3.37 where χ_{ndf}^2 decreases until the criteria is met.

The values for ε_{FD} and β are listed in table 3.2 for each pair of telescopes that are constructed with similar components. In order to quantify the introduced parameter, ε_{FD} , that is needed to give a $\chi_{ndf}^2 \leq 1$, the values are reported as a percentage of the averaged response of the two telescopes at 375 nm. Prior to the minimization the $FD_2(\lambda)$ response data are normalized by the ratio of the PD response as measured at FD_1 and FD_2 for a

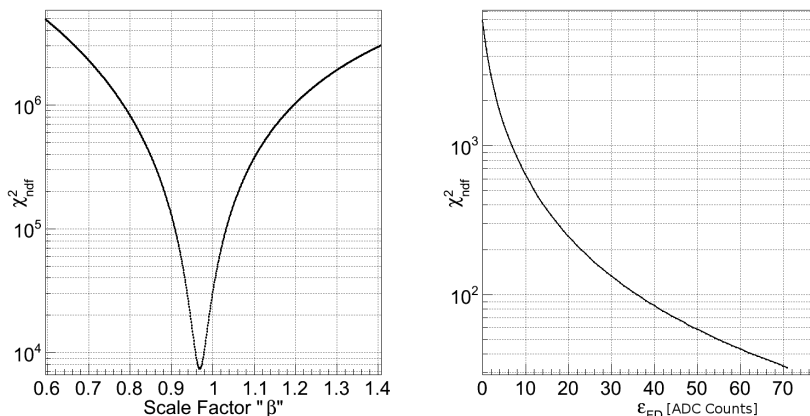


FIGURE 3.37. An example of plots showing the χ^2 minimization technique to determine the systematic uncertainty associated with the FD responses. The left plot shows the minimization by varying the scale factor between the two telescopes, and the right plot shows the determination of ϵ_{FD} such that $\chi_{ndf}^2 \leq 1$ for $ndf = 34$.

given wavelength; this serves to divide out any change in intensity of the light source as measured by the PD just downstream of the monochromator.

TABLE 3.2. Table of the ϵ_{FD} and β values obtained via (3.8) for the similarly constructed telescopes. The ϵ_{FD} for a given pair of telescopes is given in percentage relative to the averaged response of the pair of telescopes at 375 nm.

FDs	ϵ_{FD} [%]	β	FDs Affected
Coihueco2/3	0.3	0.97	CO2/3
Coihueco4/5	0.5	1.02	CO1,4-6, LA, HEAT
Los Morados3/4	0.1	1.01	LM
Los Leones3/4	3.4	1.09	LL2-5

As a check, we performed the exact same χ^2 minimization for the PD spectra measured at FD_1 and FD_2 and find all four scale factors to be order unity and no introduced parameter is larger than 1% relative to the signal at 375 nm. The largest PD systematic between two PD spectra are for Coihueco two vs. three and Coihueco four vs. five data, and including this systematic in the PD for the FD data normalization improves the χ_{ndf}^2 for the FD comparisons involving Coihueco as shown in the table.

Aside from Los Leones bay three and four, the values for ε_{FD} derived through this minimization technique are about the same size as the non-zero $\sigma(\lambda)_{Syst}^{FD}$ values, and the β scale factors are all $\sim 3\%$ within unity. The large parameters obtained for Los Leones imply that the assumption that Los Leones three and four should give similar responses since they are made of the same combination of components may not be valid, leading to a large systematic associated with those telescopes.

For each wavelength we use the ε_{FD} calculated for a given pair of FDs as the systematic uncertainty, and then these are added in quadrature with those wavelengths that have a non-zero value for $\sigma(\lambda)_{Syst}^{FD}$. The systematic uncertainties are then normalized by the telescope response at 375 nm and are added in quadrature with the others, the Lab PMT and Lab PMT QE, and plotted as the black brackets in figure 3.38.

3.4.8. PHOTODIODE MONITOR DATA. We performed a comparison between the average dark hall PD spectrum to each of the spectra measured for the data-taking nights at the FDs to ensure that the light source was stable and was consistent with what had been measured in the lab. An overall scale factor of $\sim 1\%$ was derived as the average ratio of the PD response at the FD to the lab to accommodate any overall variations in intensity or response due to temperature effects, and then we performed a χ^2 comparison for all the measured wavelengths. For all eight nights at the FDs the PD spectra agree very well, the comparison gives a $\chi_{ndf}^2 \leq 1$ where $ndf = 34$ for each, implying that the spectrum as seen by the PD was the same at all locations.

3.5. CALCULATION OF THE FD EFFICIENCY

We calculate the relative FD efficiency, $FD_{eff}^{Rel}(\lambda)$, for each bay by dividing the measured telescope response, $FD_{Resp}(\lambda)$, to the drum by the measured drum emission spectrum,

$\overline{S^{Drum}}(\lambda)$. The relative drum emission spectrum is measured as described in section 3.4.3 and takes into account the Lab PMT quantum efficiency, $QE_{PMT}^{Lab}(\lambda)$, over the 270 nm to 440 nm range.

3.5.1. FD EFFICIENCY. The relative efficiency for a given bay is calculated using (3.9) for each wavelength from 280 nm to 440 nm in steps of 5 nm.

$$FD_{eff}^{Rel}(\lambda) = \frac{FD_{Resp}(\lambda) \times QE_{PMT}^{Lab}(\lambda)}{\overline{S^{Drum}}(\lambda)} \times \frac{1}{FD_{eff}(375 \text{ nm})} \quad (3.9)$$

The curves are taken relative to the efficiency of the telescope at 375 nm since this is the relative wavelength used in the reconstruction software for all fluorescence detector calculations. The 280 nm to 440 nm range for evaluating the FD efficiency is smaller than the range measured in the lab because below 280 nm the light level is near zero intensity for the emission spectrum and FD response, and above 430 nm the FD response is also near zero.

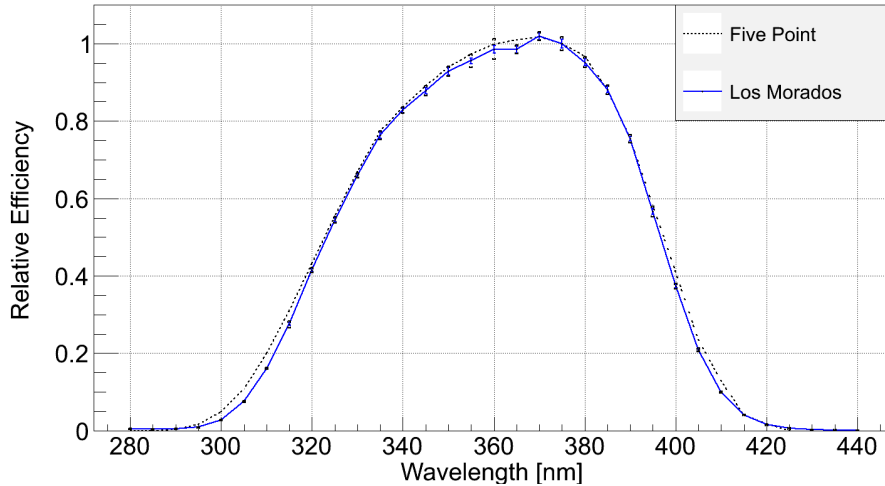


FIGURE 3.38. Los Morados relative efficiencies with the five-point curve shown as a dashed line [108] and the monochromator setup shown as the solid line (this work). Error bars are statistical uncertainties, and the brackets are the systematic uncertainties calculated as described in section 3.4.6.

Figure 3.38 shows the relative efficiency for Los Morados as measured and calculated based on the March 2014 work compared with the five-point measurement. The statistical uncertainties for the FD efficiency calculation are the propagated one-sigma statistical uncertainties associated with each quantity in (3.9) for a given wavelength, as described in section 3.4.7.1. The systematic uncertainties are estimated in two steps, first by determining a systematic at each wavelength and then by comparing two telescopes that have the same detector components and assuming that they should give a similar response to the multi-wavelength drum, as shown in sections 3.4.7.2 and 3.4.7.3. The measured calibrations for Los Leones, Coihueco, and Loma Amarilla are shown in appendix A.

3.5.2. FINAL UNCERTAINTY CALCULATION. The uncertainties in the FD efficiencies have statistical and systematic components associated with the measurement of the relative emission spectrum of the drum, the Lab PMT QE, and the FD response to the multi-wavelength drum.

3.5.2.1. *Statistical Uncertainties.* The statistical uncertainties associated with the lab work and the FD responses are propagated through the calculation of the FD efficiency via (3.9), and are calculated using (3.10) as a function of wavelength, where the wavelength dependence is removed for clarity.

$$\delta_{Stat}^{FD}(\lambda) = \sqrt{\left(\frac{QE_{PMT}^{Lab}}{S^{Drum}} \times \delta_{Stat}^{FD}\right)^2 + \left(\frac{FD_{Resp}}{S^{Drum}} \times \delta_{PMTQE}^{Drum}\right)^2 + \left(\frac{FD_{Resp} \times QE_{PMT}^{Lab}}{S^{Drum}^2} \times \delta_{PMTStat}^{Drum}\right)^2} \quad (3.10)$$

3.5.2.2. *Systematic Uncertainties.* Each systematic uncertainty described above associated with the lab work, the Lab PMT and its QE, and the FD response, the $\sigma(\lambda)_{Syst}^{FD}$ and ε_{FD} for a given FD telescope, are added together in quadrature as a function of wavelength.

3.5.2.3. *Reduction of Uncertainties.* Similar to section 3.3.3, the multi-wavelength calibration has benefited from improvements in measurement technique, hardware, and data analysis to reduce the associated uncertainty. Section 5.1 of [108] details the complicated interpolation procedure needed to account for the wide spectral widths of the notch filters when convolved with the rapidly changing FD efficiency, which led to systematics on the order of 4.5% for each of the four measured wavelengths. By using the monochromator in the work detailed here, the systematics associated with each measured wavelength at the FDs are $\sim 1\%$, and the statistical uncertainties have also benefited from the improved data analysis and the automation of the measurement process. The new FD multi-wavelength calibration now has a 3.5% total uncertainty relative to 375 nm, compared to the overall 5% quoted in [108].

The reduction in uncertainties in the multi-wavelength calibration of the FDs was achieved through a thorough understanding of the relative drum emission spectrum. As explained in section 3.4.5 the systematic uncertainty derived through χ^2 comparisons of the four measured spectra is less than 2.5% for all wavelengths, and between 320 nm to 380 nm it is $\sim 1\%$.

3.5.3. COMPARISONS BETWEEN DIFFERENTLY CONSTRUCTED TELESCOPES. We compared the combinations of detector components using a type of χ^2 test as a quantitative way to determine if there is any correlation between detector components and large χ_{ndf}^2 for $ndf = 34$. The comparisons are shown in table 3.3 with the computed χ_{ndf}^2 from comparing the FD responses taking into account PD spectra measured during data-taking; please refer to table 3.1 for the different FD component listings. In calculating the aforementioned χ_{ndf}^2 for the differently constructed FD telescopes we use the ratio of the PD data taken at the corresponding FDs to normalize the average response of one of the FD types. The PD data from the two FD data-taking nights are averaged together as a function of wavelength and

the ratio of the PD averages from the two types of FDs are applied to the combined FD response and the statistical and systematic uncertainties. Using this normalization serves to divide out any differences in the drum spectrum between the two measurements of the FD types and it accentuates the measured differences. An example for calculating the χ^2 between Coihueco2/3 and Coihueco4/5 is shown in (3.11) where the uncertainties are those described in 3.5.2; the χ^2 is divided by $ndf = 34$ to arrive at the values listed in table 3.3.

TABLE 3.3. Table of the χ_{ndf}^2 values obtained for the FD comparisons, where $ndf = 34$.

Comparison	χ_{ndf}^2
Coihueco2/3 vs. Coihueco4/5	3.37
Los Morados4/5 vs. Los Leones3/4	0.181
Coihueco4/5 vs Los Morados4/5	26.9
Coihueco2/3 vs. Los Leones3/4	1.49
Coihueco2/3 vs. Los Morados4/5	65.6
Los Leones3/4 vs. Coihueco4/5	0.872

$$\chi^2 = \sum_{n=1}^{N_\lambda} \frac{\left(\overline{S_{CO23}(\lambda)_n} - PD_{Ratio}(\lambda)_n * \overline{S_{CO45}(\lambda)_n} \right)^2}{\left(\delta_{Stat}^{CO23}(\lambda)_n \right)^2 + \left(\sigma_{Syst}^{CO23}(\lambda)_n \right)^2 + \left(PD_{Ratio}(\lambda)_n * \delta_{Stat}^{CO45}(\lambda)_n \right)^2 + \left(PD_{Ratio}(\lambda)_n * \sigma_{Syst}^{CO45}(\lambda)_n \right)^2} \quad (3.11)$$

Where :

$$PD_{Ratio}(\lambda) \equiv \frac{\overline{S_{CO45}^{PD}}(\lambda)}{\overline{S_{CO23}^{PD}}(\lambda)}$$

The ε_{FD} derived from comparing Los Leones bays three and four was larger than the others by a factor of five, and due to the ε_{FD} then being used as a systematic uncertainty for those bays, the comparisons in table 3.3 involving Los Leones are not valid. Los Leones has a large systematic uncertainty based on the assumption that bays three and four should give the same response, and therefore χ^2 comparisons with other telescope types are not sensitive.

In order to determine if either of the Los Leones bays give a small χ_{ndf}^2 when compared to the other combination of detectors, we gave Los Leones bays three and four individually a systematic that was as large as the largest ε_{FD} calculated for the other bays, roughly 2% of the signal, and then compared bays three and four to Coihueco and Los Morados. With the conservative systematic applied to the Leones data, the χ^2 comparisons all give $\chi_{ndf}^2 > 3$ implying that the telescopes at Los Leones are different than the others.

3.5.4. FD EFFICIENCIES. Between 320 nm and 400 nm all eight measured efficiencies agree with the five-point measurement within uncertainties, but below 320 nm and near and above 400 nm there is disagreement. The disagreement at the shortest and longest wavelengths is perhaps not surprising since the previous highest and lowest measurements were at 405 nm and 320 nm and the efficiency was extrapolated to zero from those points following the piecewise curve [108] and assumed to go to zero below 295 nm and above 425 nm.

Based on the comparisons between the different detector components shown in table 3.3, a global average of the eight measured relative FD efficiencies should not be applied to all FD telescopes in the Observatory. Instead we recommend that each FD type, based on components, have its own efficiency.

Coihueco two and three will have their own efficiency being the average of the two measurements in those bays, and bays one, four, five, and six use the average of the measurements of bays four and five. Since Loma Amarilla was not measured, we have to assume that it should have a similar efficiency to the bays that are the same construction in Coihueco, which are bays four and five, so the averages of these curves should be used for Amarilla. HEAT will use the efficiency corresponding to the type of components it has from Coihueco. All of Los Morados should use the average of the measurements made in bays four and five.

For Los Leones, although it has by far the largest ε_{FD} , we take the average of the two measurements performed in bays three and four as the response and apply the large systematic derived from the comparison between the two.

3.6. NEW CALIBRATIONS: NOW WHAT?

The following Chapter will discuss the implementation of the FD calibrations in the Auger Observatory event reconstruction software. With the calibrations inserted into the event reconstruction framework, I then perform comparisons using Monte-Carlo simulations of showers and the response of the detector(s), to the actual Auger Observatory data reconstructions, which elucidate the effects of changing the multi-wavelength calibration on Auger Observatory measurements. I will then explain how the detailed multi-wavelength calibration affects the FD energy estimation and reconstructed X_{max} measurements made by the observatory.

CHAPTER 4

THE EFFECTS OF CALIBRATIONS ON MEASUREMENTS

The nitrogen fluorescence technique for measuring EAS as they propagate through the atmosphere was introduced in the 1960s. Its greatest appeal is that the number of photons emitted due to ionizing the nitrogen molecules in the atmosphere is proportional to the energy deposited into the atmosphere.

$$\frac{dN_\gamma}{dX} \propto \frac{dE_{dep}^{tot}}{dX} \quad (4.1)$$

Measuring the amount of nitrogen fluorescence is then a calorimetric estimation for the energy contained in an EAS, and therefore the energy of the initial primary particle. The UV light is emitted isotropically about the shower axis, allowing for side-on observation, but the number of photons emitted, $Y(\lambda, P, T, u)$, is very small, only a few photons per ionizing particle per meter of track-length in the atmosphere and is dependent on atmospheric parameters, pressure (P), temperature (T), and humidity (u). Measuring the nitrogen fluorescence light from afar meant the atmosphere must be characterized very well, as described in the atmospheric calibration section of Chapter 3, so that the attenuation $\tau_{atm}(\lambda, X)$ must be well characterized in order to fully understand the emission of photons and their subsequent attenuation.

The relationship (4.1) between the number of fluorescence photons generated, dN_γ , per track-length in the atmosphere, dX , as detected by an FD telescope, and the total energy deposited into the atmosphere, dE_{dep}^{tot} , becomes the expression in (4.2) for the energy deposited into the atmosphere when one integrates over the attenuation, the number of photons emitted, and the FD efficiency, $\varepsilon_{FD}(\lambda)$. A change in the multi-wavelength calibration of the

FD telescopes implies a change in their efficiency at detecting the photons that reach their aperture. It follows then from (4.2), that altering the detection efficiency will directly affect the energy measurement.

$$\frac{dN_\gamma}{dX} = \frac{dE_{dep}^{tot}}{dX} \int Y(\lambda, P, T, u) \tau_{atm}(\lambda, X) \varepsilon_{FD}(\lambda) d\lambda \quad (4.2)$$

As will be seen below, the longitudinal development of an EAS is directly measured by the FD by how much fluorescence light it detects as a function of atmospheric depth, and from this the location in the atmosphere where the shower maximum occurs, X_{max} , is determined. Changing the FD efficiency, particularly as a function of wavelength, will also affect the measurement of shower maximum.

The integral over wavelength in (4.2) readily shows how the atmospheric attenuation, $\tau(\lambda, X)$, and the fluorescence yield, $Y(\lambda, P, T, u)$ are entangled with the FD efficiency. The wavelength dependencies in these factors will be discussed below as they pertain to a change in the FD efficiency.

4.1. HYBRID DATA

Before the attenuation of the fluorescence light can be evaluated, the geometry of a given EAS must be determined, and for this thesis work I took advantage of the hybrid nature of the Pierre Auger Observatory, and used data and simulations that were observed by the SD and FD simultaneously. While the focus of this thesis deals with the calibration of the FD, the timing information obtained by the SD for a given event was needed to determine the geometry more accurately.

Within the Monte-Carlo (MC) reconstructions, a hybrid requirement was used so that at least one tank within the SD was triggered, as described in Chapter 2 section 2.1, to pin down

the core location of the simulated shower. Auger data used for this analysis were the so-called golden hybrid data. These golden data are the highest quality events the Observatory produces, in which the FD and SD are triggered independently for a given air shower, and it is a subset of these data that are used in the SD-FD cross-calibration shown in figure 2.3 in Chapter 2.

The energy for a given event is estimated through integrating the total energy deposited into the atmosphere as a function of slant depth as measured by the amount of light detected by an FD. The reconstruction of the EAS longitudinal profile from the signals in the individual PMTs is a complex procedure that is outlined in detail elsewhere [162], but the wavelength dependence of the method is crucial to this work.

4.1.1. HYBRID GEOMETRY. The hybrid events utilize both detectors within the Observatory and achieve the best geometrical accuracy by combining the timing information obtained by the SD with the shower parameters measured by the FD. Within the FD, EAS

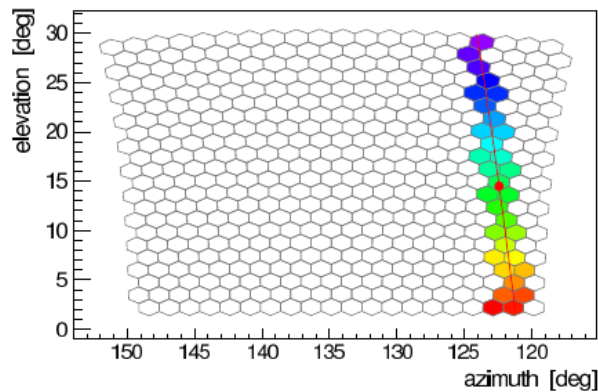


FIGURE 4.1. An EAS as it appears in a part of the FD event display, where each hexagon represents one PMT pixel within the camera. The colors represent the relative timing between subsequent triggered pixels, and the line through the pixels represents the Shower-Detector Plane.

are detected as a sequence of triggered pixels in the telescope camera. Figure 4.1 shows an

example of a real EAS observed by an FD telescope where the coloring of the pixels show the relative timing between the subsequent triggered pixels.

From the information gathered by the triggered pixels, the first step in determining the geometry of the shower is calculating the Shower-Detector Plane (SDP), or the plane containing the shower axis and the pointing direction of the triggered FD pixels, the line through the pixels in figure 4.1. The timing information from the triggered pixels is then used to determine the shower axis within the SDP, and figure 4.2 schematically shows the relevant angles and distances associated determining the shower axis. The geometrical projection of

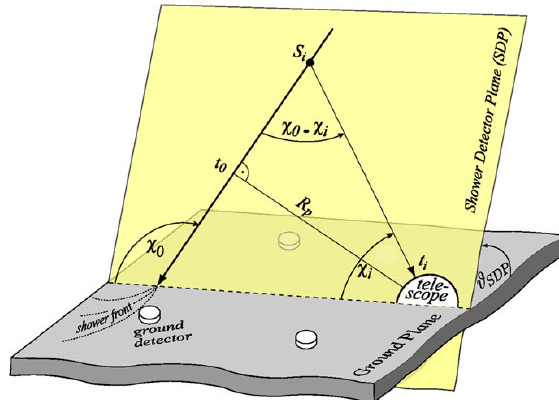


FIGURE 4.2. A schematic showing the SDP as used in the Pierre Auger Observatory, defining the geometry of the shower reconstruction using the observables of the fluorescence detector [93].

the shower axis on the camera can be parameterized in terms of the angle χ_i the i^{th} triggered pixel makes with respect to the horizontal, R_p the distance of closest approach of to shower to the telescope, and the angle the shower makes with respect to the horizontal χ_0 . These parameters then satisfy (4.3) for the i^{th} triggered pixel, where t_0 is the time of closest approach.

$$t(\chi_i) = t_0 + \frac{R_p}{c} \tan\left(\frac{\chi_0 - \chi_i}{2}\right) \quad (4.3)$$

Figure 4.3 shows another schematic of the geometry involved with determining the SDP from the FD timing information. Section 10 of [163] has much a more detailed explanation of the minimization techniques used in the determination of the parameters in (4.3). Use

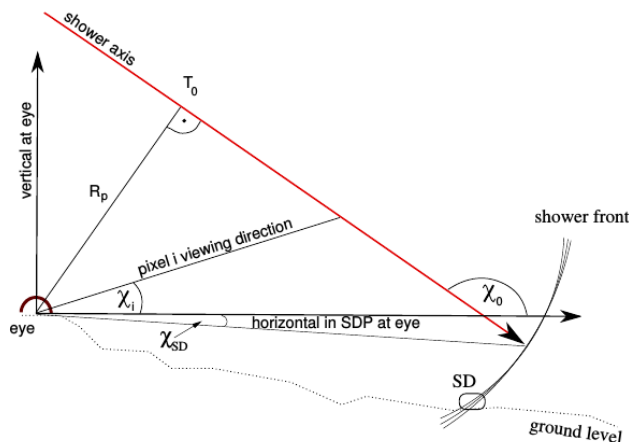


FIGURE 4.3. Schematic showing relevant geometry for the SDP as a 2D slice in azimuth, from [163].

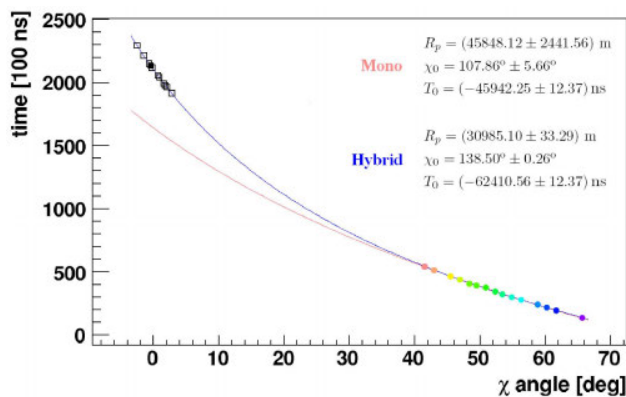


FIGURE 4.4. A plot of $\frac{d\chi}{dt}$ measured with the FD timing information only as the points in the lower right, and the improvement to the fit once the data from the SD, the points in the upper left, are included. From [93].

of the SD information becomes important when the angular speed, $\frac{d\chi}{dt}$, of the shower across the camera is slow such that there are several R_p and χ_0 values satisfying (4.3). The timing information from the triggered SD stations helps to break this degeneracy, as shown in figure 4.4, where the FD-only fit to the timing is shown as the lower line in red, and the

hybrid as the upper line in blue. By using the hybrid reconstruction, the location of the shower core has a resolution of 50 m [93], and within this thesis work the hybrids allow for a high quality dataset for analysis.

4.1.2. MEASURING THE LONGITUDINAL PROFILE. With the geometry determined for the EAS, the light reaching the telescope aperture is now converted to energy deposited into the atmosphere at the shower as a function of slant depth. The attenuation of the fluorescence photons in the atmosphere needs to be well known, section 4.1.4 will discuss this and the wavelength dependence. The energy deposited per unit depth in the atmosphere, $\left(\frac{dE}{dX}\right)_i$, is calculated for every 100 ns time bin in each triggered pixel, and the longitudinal profile for the EAS is constructed. The 100 ns time bins are converted to slant depth, g/cm^2 ,

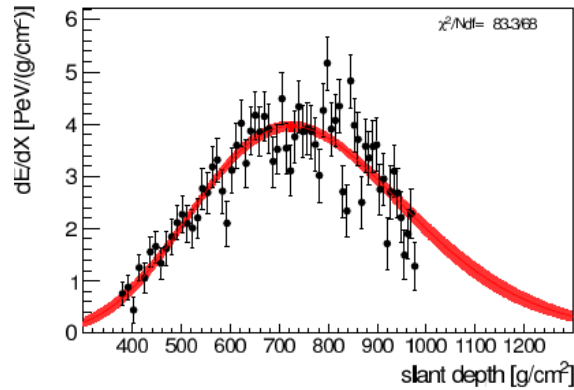


FIGURE 4.5. An example of the longitudinal profile reconstructed for an event. Each point is the energy deposited into the atmosphere for a 100 ns time bin with a triggered pixel. The red line is a Gaisser-Hillas fit to the data whose width represents the uncertainty associated with the fit.

and in figure 4.5 the profile is shown for the event shown in figure 4.1.

The calorimetric energy is then estimated by fitting the profile with a Gaisser-Hillas function [164], and integrating it. Equation (4.4) is the functional form of the Gaisser-Hillas.

$$f(X) = \left(\frac{dE}{dX}\right)_{max} \left(\frac{X - X_0}{X_{max} - X_0}\right)^{\frac{X_{max} - X_0}{\lambda}} e^{-\frac{X_{max} - X}{\lambda}} \quad (4.4)$$

There are four free parameters in expression (4.4): X_{max} , the depth in the atmosphere where the EAS reaches its maximum energy deposit, the maximum energy deposit $(\frac{dE}{dX})_{max}$, and two shape parameters X_0 and λ . The total energy is then the sum of the Gaisser-Hillas integral and the estimation of the energy carried away by neutrinos and high-energy muons, which produce no light. The invisible energy is estimated using MC methods and depends on primary composition and neutrino and muon production models. The correction for the invisible energy depends on the energy contained in the EAS, but based on the work in [165] the correction varies from 11% at 10^{18} eV to 7% at $>10^{20.5}$ eV.

4.1.3. FLUORESCENCE YIELD. Besides the atmospheric attenuation parameter, $\tau(\lambda, X)$, that was introduced in the expression at the beginning of this Chapter, the fluorescence yield, $Y(\lambda, P, T, u)$, is also a function of wavelength, which is convolved with the FD efficiency. The fluorescence yield is the number of photons emitted per amount of energy deposited into the atmosphere via ionization of nitrogen molecules from the secondary particles in an EAS. It is a function of atmospheric parameters along with wavelength (λ). The excited nitrogen molecules radiate photons either through relaxing to a ground state or through collisional quenching; reference [166] has a more detailed description of the fluorescence process.

$$N_{gas} \propto E_{dep}^{gas} Y_{gas}(p) \propto p \frac{f_{N_2}}{1 + \frac{p}{p'_{gas}}} \quad (4.5)$$

In its simplest form, the number of fluorescence photons emitted by a given volume of gas can be written as (4.5), as shown in [137], where f_{N_2} is the fraction of nitrogen molecules in the atmosphere (79%), and p'_{gas} is the collisional quenching reference pressure. For nitrogen, p'_{N_2} can be expressed as (4.6)

$$p'_{N_2} = \frac{\sqrt{\pi m_{N_2} k T}}{4\tau_0 \sigma_{NN}} \quad (4.6)$$

with τ_0 being the lifetime of the excited state, m_{N_2} is the molecular mass of nitrogen, k is Boltzmann's constant, T is temperature, and σ_{NN} is the nitrogen-nitrogen collisional cross section. The atmosphere is a mixture of nitrogen and oxygen such that p'_{gas} becomes

$$\frac{1}{p'_{air}} = \frac{0.79}{p'_{N_2}} + \frac{0.21}{p'_{O_2}} \quad (4.7)$$

where p'_{O_2} similar to (4.6) but for oxygen with the nitrogen-oxygen collisional cross section σ_{NO} .

In (4.5), $Y_{gas}(p)$ is the fluorescence yield as measured in units of photon/MeV of energy deposited, and recently has been measured extremely well by the AIRFLY collaboration and found to be 5.6 photons/MeV with a systematic uncertainty of 4% [98, 122, 136, 167]. Previously the uncertainty in the fluorescence yield was 14%, and was the dominating contributor to the overall 22% uncertainty in the Auger Observatory energy scale. Details of how this new fluorescence yield measurement affected the energy scale can be found in [167].

The AIRFLY measurement also gave special attention to the pressure dependence of the main spectral bands within the nitrogen fluorescence spectrum. They measured the intensities of 24 bands as a function of pressure relative to the intensity of the 337 nm band, Y_{337} [137]. The pressures varied from 4 hPa to 10^3 hPa, or roughly the change in pressure experience by an EAS propagating 40 km vertically through the atmosphere. Several of the bands vary in intensity, relative to Y_{337} , such as the band at 391.4 nm decreasing by almost a factor of two as shown in figure 4.6, meaning that the number of photons from different wavelength bands vary as an EAS propagates through the atmosphere. The pressure dependence on the relative wavelength intensities may imply systematics associated with a change in the wavelength-dependent detector efficiency.

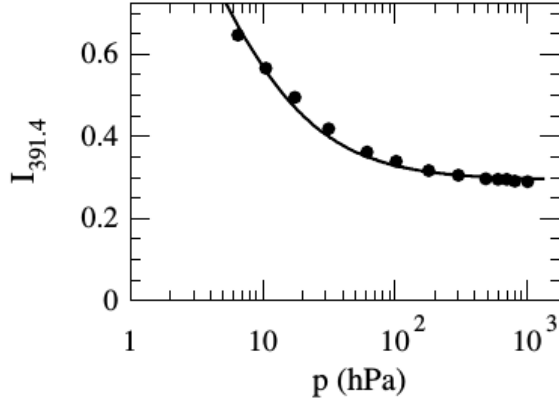


FIGURE 4.6. The pressure dependence in the intensity of the fluorescence band at 391.4 nm relative to the intensity at the 337 nm band, shown with statistical uncertainties only, and a fit to the data. Figure is from [137], see for details about the fit.

4.1.4. ATTENUATION OF FLUORESCENCE LIGHT. There are two forms of attenuation the emitted fluorescence light undergoes as it propagates through the atmosphere before entering an FD, Rayleigh, which is strongly dependent on wavelength, and Mie due to the aerosol content of the atmosphere. Rayleigh attenuation is accounted for by determining the distance the light traveled via timing as explained in section 4.1.1 above, and Mie scattering is calculated using the atmospheric monitoring information obtained through the various laser systems described in Chapter 3 section 3.2.1. An exhaustive study on the effects of molecular and aerosol attenuation on the fluorescence measurements performed at the Auger Observatory is found in reference [139].

How the two attenuations depend on wavelength makes them relevant to this work because a change in telescope efficiency convolved with these wavelength dependencies will affect the measurements made by the detector.

4.1.4.1. *Rayleigh Scattering.* Molecular absorption and scattering per unit length is characterized by the extinction coefficient shown in (4.8),

$$\alpha_{ext}(h, \lambda) = \alpha_{abs}(h, \lambda) + \beta(h, \lambda) \quad (4.8)$$

where α_{abs} and β are the absorption and scattering coefficients, respectively.

The total optical depth between a given telescope and the point of emission in the atmosphere is then the integral of (4.8) over the path length, as in (4.9).

$$\tau(h, \lambda) = \int_{h_{FD}}^h \alpha_{ext}(h', \lambda) dh' \quad (4.9)$$

Fortunately, in the near UV wavelengths where nitrogen fluorescence takes place the molecular extinction coefficient simplifies to only being dependent on Rayleigh scattering. Work done in [168] showed that the Rayleigh cross section on air dominates the inelastic scattering, and there is little absorption. This means at standard temperature and pressure, the scattering coefficient, β in (4.8), becomes (4.10),

$$\beta^{STP}(h, \lambda) \equiv N_s \sigma(\lambda) = \frac{24\pi^3 (n_s^2(\lambda) - 1)^2}{\lambda^4 N_s (n_s^2(\lambda) + 2)^2} \left(\frac{6 + 3\rho_n}{6 - 7\rho_n} \right) \quad (4.10)$$

which is the analytical Rayleigh scattering cross section [169, 170], and (4.8) does not have a non-zero absorption term.

In the above expression, N_s is the molecular number density of air under standard conditions, $n_s(\lambda)$ is the refractive index of air as a function of wavelength, and ρ_n is the depolarization factor that accounts for the anisotropy in the shape of an air molecule. Within the range of wavelengths for nitrogen fluorescence the depolarization factor has been measured and is about 0.03 [169]. The molecular attenuation of the fluorescence light just depends on the $1/\lambda^4$ Rayleigh scattering cross section, and since there is such a strong inverse-wavelength dependence it will affect the shorter wavelengths in the nitrogen fluorescence spectrum more. Any changes to the FD efficiencies at the shorter wavelengths coupled with the Rayleigh scattering will lead to direct effects on the Auger Observatory energy scale.

4.1.4.2. *Mie Scattering and Atmospheric Aerosols.* Attenuation due to aerosols in the atmosphere above the Auger Observatory relies more on measurements and monitoring done in the field due to the non-analytical nature of the aerosol extinction coefficient. The robust atmospheric monitoring system described in section 3.2.1 of Chapter 3 makes several measurements of the vertical aerosol optical depth (VAOD), $\tau_a(h, \lambda)$.

How the VAOD depends on wavelength is given by (4.11), and was formulated by Ångström [171],

$$\tau_a(h, \lambda) = \tau(h, \lambda_0) \left(\frac{\lambda_0}{\lambda} \right)^\gamma \quad (4.11)$$

where γ is the Ångström exponent and λ_0 is a reference wavelength, 355 nm, the wavelength used by the CLF. The exponent is measured in the field and depends on the sizes of the scattering aerosols, where smaller particles have a larger exponent [172]. For regions similar to that around the observatory, coarse particles ($>1 \mu\text{m}$) dominate the aerosols, and therefore the VAOD has little wavelength dependence [173].

4.2. BUILDING THE ANALYSIS

In order to investigate the effects on measurements made by the Pierre Auger Observatory from updating the multi-wavelength calibration, I took the three multi-wavelength calibrations, the Piece-Wise [154], Five-Point [108], and the work presented in Chapter 3, which will be referred to as the new-multi-wavelength, and compared them. I performed an analysis determining the effects on measurements made by the Auger Observatory, using MC air showers generated with CORSIKA [174], and real Auger Observatory data, called golden hybrids, from 2006 through 2013. The simulated showers provided an expectation for

the various measurements using known proton and iron primary particles, and these expectations give perspective on the golden hybrid events, which reveal the actual effect on the results.

The analysis proceeded in a straightforward manner. For the MC showers, I performed a hybrid detector simulation described below in section 4.2.2.1, and then performed a hybrid reconstruction on the simulated detector response data. For the golden hybrid data, I performed the typical hybrid data reconstruction outlined below in section 4.2.3, which is very similar to the reconstruction performed on the MC data. I then investigated the effects on FD energy estimation and X_{max} due to updating the multi-wavelength calibrations, and estimated systematics related to energy dependence, distance from the FD, and azimuthal shower angle, associated with this thesis work on those measurements.

4.2.1. SHOWER SIMULATIONS. Shower libraries were obtained from the Centre de Calcul de l'IN2P3, or CC-IN2P3 [175], which handles most of the Auger Collaboration's MC productions. I used two sets of CORSIKA shower productions called "EPOS 2 Proton SRB" and "EPOS 2 Iron SRB", where each use the EPOS 1.99 hadronic interaction model [176], with full azimuthal coverage, 0° – 360° , $\log(E/\text{eV})$ energy Bins of: 18.0, 18.5, 19.0, 19.5, 20.0, 20.5, zenith angle bins: 0° , 18° , 26° , 32° , 38° , 41° , 45° , 53° , 57° , 60° , 63° , thinning of 10^{-6} , and have proton and iron primaries. I chose these productions because they were the most recent (2011) shower-only simulations produced, and the extrapolation of the EPOS model to ultra-high energies shows good agreement with the Auger measured proton-air cross section [177].

4.2.2. AUGER OFFLINE SOFTWARE FRAMEWORK. The so-called "Offline" is a blanket term that describes the software framework associated with the Auger Observatory. It is

implemented in C++, and takes advantage of object oriented design and common open source tools. There are three main parts to Offline, a collection of algorithm-based modules that are assembled and sequenced via instructions in an Extensible Markup File (XML), an event data model through which modules can relay data to one another and accumulate all simulation and reconstruction information, and detector description files where the components of the Observatory are defined in terms of their configuration and performance as a function of time. Figure 4.7 schematically shows the three parts of the Offline framework.

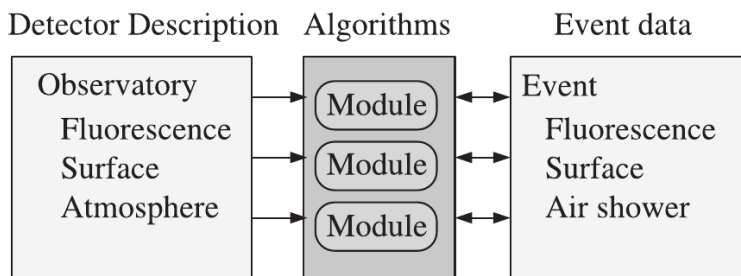


FIGURE 4.7. Very general structure to the Offline Framework, from [178].

The parts of Offline that are relevant to this work in terms of measured FD efficiencies are the module(s) related to calculating the energy deposit in the atmosphere using FD data, and the FD detector description file(s). For extensive details about the whole framework see [178], and section eight of [163]. The sequence of modules put together in an XML file determines what the user is attempting to do, and in my case this was either performing a hybrid detector response simulation, or a hybrid reconstruction. The series of modules used in the hybrid reconstruction of MC data and real data related to determining the geometry and energy are identical in this analysis.

4.2.2.1. *Hybrid Detector Response Simulation.* Before performing the reconstructions on the MC showers described above, a hybrid detector simulation is performed within the Offline framework to generate MC detector response data to reconstruct. The showers were thrown randomly within the area covered by the SD, the number of showers thrown varied as a

function of energy in order to limit computation time. For the proton showers there were ~ 5000 showers for the 18.0 and 18.5 energy bins, ~ 2500 for 19.0, ~ 2000 for 19.5 and 20.0, and ~ 1000 for 20.5. The iron showers had similar totals for each energy bin.

The simulation proceeds using an ultra-fast version of the SD simulation and then is followed by the standard FD simulation. The SD simulation uses the “SdSimpleSim” module, where realistic air shower events in the SD are generated without employing full MC simulations for the water tanks, and this saves weeks of computation time for this work, without affecting the crucial FD reconstruction. With this approach the lateral distribution of the air shower is assumed to follow a NKG-like functional form [179, 180], and the hybrid geometry can be determined well enough for this analysis.

The FD simulation [181] encompasses the generation of the fluorescence and Cherenkov photons given the MC air shower information, the atmospheric attenuation of the light, the propagation of the photons through the FD telescope to the photocathodes of the camera PMTs via ray-tracing methods, and then this photon signal is used as input to a simulation of a model detector electronics and trigger. Several XML files parameterize the atmosphere in terms of the expressions above in section 4.1.4 based on experimental data and atmospheric models. The AIRFLY fluorescence yield measurement is used to determine the number of photons generated and the nitrogen spectrum is estimated using twenty equal sized wavelength bins from 300 nm to 420 nm. Once the simulated photons reach the telescope aperture the ray-tracing module takes into account all of the components within the telescope using the transmittance, reflectivity, and efficiency according to experimental measurements or manufactures’ values. The transformation of the photons arriving at the PMTs within the

camera to ADC counts is done using the absolute calibration constants,

$$N_i^{375equiv} = C_i \times N_i^{ADC} \quad (4.12)$$

where for a given pixel, i , the calibration constant, C_i , related the number of ADC counts, N_i^{ADC} , to the number of 375 nm-equivalent photons, $N_i^{375equiv}$. The spectrum as calculated in the twenty wavelength bins is combined into a single 375 nm equivalent number of photons using the optical efficiency, ε_λ , such that in expression (4.12) $N_i^{375equiv}$ becomes:

$$N_i^{375equiv} = \frac{1}{\varepsilon_{375}} \sum_{\lambda} N_\lambda \varepsilon_\lambda \quad (4.13)$$

where the sum is over the twenty wavelength bins.

4.2.3. HYBRID RECONSTRUCTION. With the MC event data generated using the CORSIKA shower simulations, the next step in the analysis is to perform a hybrid reconstruction. The reconstruction for the MC event data and golden data follow the same set of modules, and both used the SdSimpelSim to limit the computation time. Details about the hybrid reconstruction can be found elsewhere, see section 9.2 of [178], and [182, 183], but what is relevant to this work is the algorithm that takes the measured photon flux at the aperture and relates it to the energy deposited at the shower track through a numerical implementation of an analytic least-squared matrix formalism, as this is where the multi-wavelength calibration is used. The Cherenkov-fluorescence matrix calculation is described in gory detail in reference [162]. The module where the algorithm is calculated is called “FdEnergyDepositFinderKG”, but before I could proceed with my analysis I had to redefine the FD efficiencies within the algorithm(s) to be telescope-dependent. Prior to my work all FD efficiencies were assumed to be the same, and for the sake of simplicity in the Offline

code, the efficiency of a telescope in a given event was defined as the efficiency of the first telescope in the building (Eye). This simple definition of the FD efficiency worked fine with previous calibrations, but this would not work with measurements presented in Chapter 3. It is also the FdEnergyDepositFinderKG module that required a well defined shower geometry to work properly, and forced the hybrid requirement for my analysis. Implementing the telescope-dependent efficiencies were straightforward and only required a few modifications to the matrix calculation source file.

For the MC event data there are a total of fifteen reconstructions for each type of primary, three calibrations and five energy bins. I chose not to include the $10^{20.5}$ eV energy bin in the analysis since the golden data do not have observed events with energy that large. The golden data were treated in a similar fashion where they were broken up into the three calibrations, but I then broke up the eight years of data into three separate sets based on the years 2006-2008, 2009-2011, and 2012-2013, allowing them to be run in parallel as a safeguard if one failed.

4.3. MEASUREMENTS

I have evaluated the effect of the multi-wavelength calibrations on the FD energy estimation and the measurement of X_{max} . The calorimetric energy is estimated by integrating (4.2) over the full atmospheric path length traversed by the EAS, and X_{max} is determined by where the longitudinal profile reaches its maximum. Both of these measurements are affected by the number of photons an FD detects, but how that number depends on other quantities, such as distance from the FD, and the azimuthal shower angle have also been examined.

4.3.1. DATA SELECTION. Before performing any analysis on measurements, I put the reconstructed data, MC and real, through a set of strict data quality cuts. The cuts that are

applied are the same used when performing the FD-SD energy calibration; they are described in detail in [128, 135, 184]. Explained here are the field of view (FoV) cut applied on the X_{max} data, and those cut(s) that have a low selection efficiency.

4.3.1.1. *Real Data Cuts.* Shown in figure 4.8 are the selection efficiencies of the cuts applied to the 2012-2013 golden data. The uncertainty on X_{max} was required to be below $40 \frac{g}{cm^2}$, as this is the theoretical value for the separation between expected proton and iron X_{max} distributions, and the uncertainty on the energy estimation was set to be less than 20%. The least efficient is the core distance cut for 750 m as the maximum distance of the water tank from the shower core, and is included in the SD-FD calibration dataset in an attempt to require the events are well contained within the area covered by the SD [135].

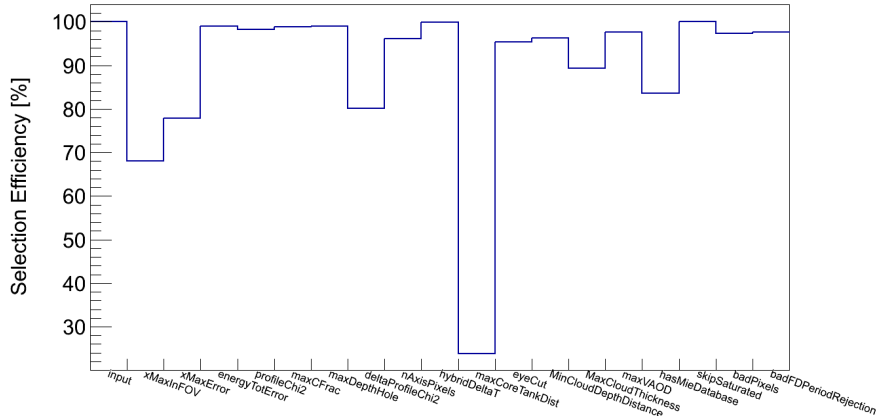


FIGURE 4.8. Selection efficiencies of data-quality cuts

The X_{max} FoV cut is a fiducial cut due to the FoV of the FD affecting the sampling of the X_{max} distributions, and so showers that have vastly different geometries are treated equally in the analysis. By requiring X_{max} to be within the FoV of the FD leads to biased event selection where events with very small or large X_{max} are cut due to their values being above or below the FoV respectively. The effect of the FoV of the FD on three different event geometries is shown in figure 4.9, where the FoV is the hatched region inside the dashed

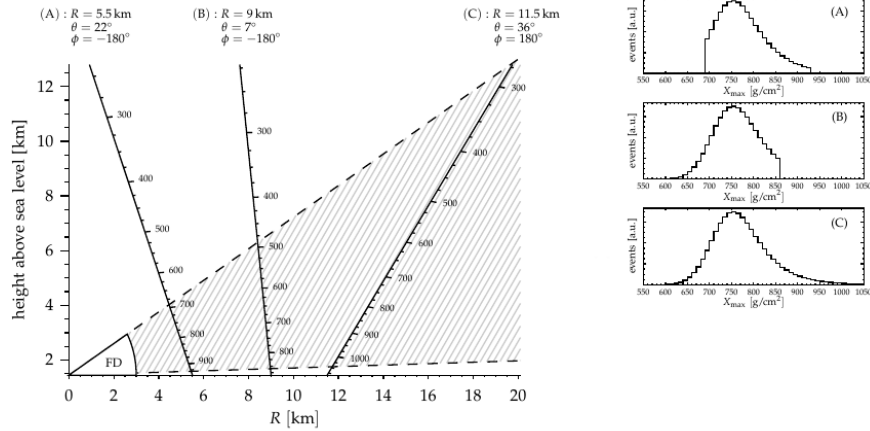


FIGURE 4.9. Schematic showing how the field of view of the FD can affect the sampling of the X_{max} distribution. The left figure shows three different examples of EAS geometries, (A), (B), and (C) in g/cm². The FD FoV is represented by the hatched region within the dashed lines. The right figure are examples of truncated X_{max} distributions corresponding to the geometries on the left. Adapted from [128].

lines. As can be seen in the figure the geometries following type (C) are those that will be preferentially selected since they are the only ones that are fully contained within the FD FoV. In order to understand the affect of the FoV bias studies were performed on data in [128] on the differential behavior of $\langle X_{max} \rangle$ on the lower and upper FoV boundary, X_l and X_u . Figure 4.10 shows an example of one of the studies. When the FoV starts truncating

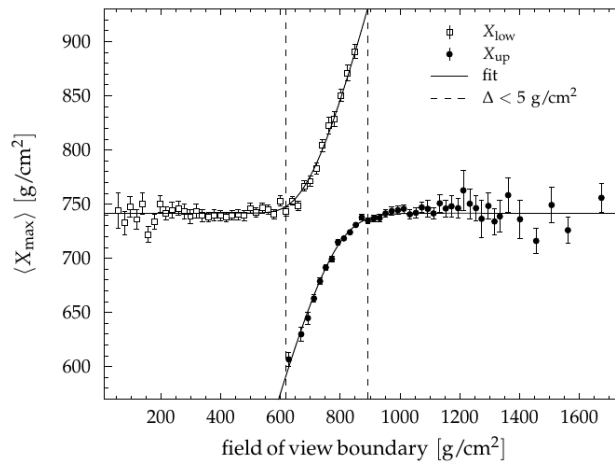


FIGURE 4.10. Example showing the effect of the X_{max} FoV cut, from [128].

an X_{max} distribution as in the (A) geometry in figure 4.9 the observed $\langle X_{max} \rangle$ begins to

deviate from its unbiased value as shown by the boxes in the left data of figure 4.10, and similarly for those geometries like (B) the filled circles on the right show how the observed $\langle X_{max} \rangle$ deviates. The fiducial values of X_l and X_u are set such that the deviation of $\langle X_{max} \rangle$, $\Delta > 5 \text{ g/cm}^2$, as represented by the example in figure 4.10.

4.3.1.2. *MC Data Cuts.* Cuts applied to the MC data are mostly the same as above. The only difference is the absence of cuts that remove bad time periods for the FD and SD, and cuts associated with atmospheric properties, since this work is only using the MC data for expectations on X_{max} values.

4.3.2. ENERGY ESTIMATION. As explained in section 4.1.2, the number of photons detected by the FD as a function of atmospheric depth is converted to energy deposited as a function of depth by understanding the fluorescence and Cherenkov light emission. Then numerical integration of (4.9) accounts for the attenuation of the photons, and the longitudinal profile for the EAS is assembled for every 100 ns time bin measured. Once the longitudinal profile is determined it is fitted with a Gaisser-Hillas function, and this expression is integrated over the full atmospheric path length to give the calorimetric energy of a given EAS.

The expression introduced at the beginning of this Chapter shows that the number of photons detected by the FD, N_γ , is directly proportional to the efficiency of the FD, and this, in turn, affects the energy estimation. When the Auger collaboration switched to the five-point calibration in 2012, it was shown that the Auger energy scale at 10^{18} eV increased by 4.3% due to the change [185]. The increase in energy arises because the five-point calibration measurement showed that the FDs were less efficient than assumed based on the piece-wise calibration, meaning that more photons are needed to generate an ADC count in the PMTs, and more photons meant more energy.

For this analysis, I sought to repeat this measured increase within the data I selected. I performed an event-by-event comparison between data reconstructed with the piece-wise calibration and the five-point calibration. Shown in figure 4.11 is the comparison between reconstructed energies for the piece-wise and five-point calibrations as a function of energy. The energy bins in the figure are defined as $\Delta\log(E/\text{eV}) = 0.1$ starting at $10^{17.8}$ eV up to $10^{19.5}$ eV, where after $10^{19.5}$ eV an integral bin is used to the highest energy event; the average value for the energy reconstructed with the five-point calibration within the energy bin is used as the ordinate within the figure. The uncertainties are statistical only, and are the standard deviation of the mean of the difference distributions at each energy bin.

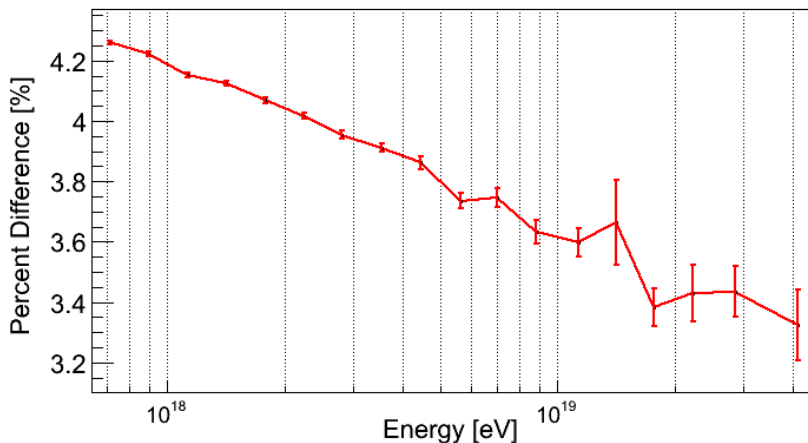


FIGURE 4.11. Comparison between data reconstructed with the piece-wise and five-point calibrations as a function of energy. The comparison was performed on an event-by-event basis so that only the same events are used in this analysis. See the text for details about binning.

For the data used within this analysis, I find a difference of 4.2% at 10^{18} eV, and a decrease with increasing event energy. The decrease as a function of energy can be understood a priori if one recalls the difference between the two calibrations, and that higher energy events are generally further away from the FDs. The five-point calibration measured that the efficiency of the FDs below 380 nm, relative to 380 nm, was $\sim 12\%$ less than the piece-wise calibration, therefore the FDs are less efficient at shorter wavelengths. It is this inefficiency at shorter

wavelengths coupled with the increased Rayleigh attenuation on the higher-energy events that causes the change in energy to decrease with increased energy. There are fewer short-wavelength photons reaching the aperture in the high-energy events that would be affected by the change in the efficiency at those wavelengths.

An a priori understanding of the affect on the energy due to changing from the five-point calibration to the calibration described in this thesis will not be as straightforward. This is partly due to there being telescope-dependent calibration curves now implemented, and a subset of Coihueco having its own calibration, and because the shorter wavelengths are not uniquely affected; the calibration presented in Chapter 3 affects the the upper and lower wavelength regions. See appendix A for a reminder about how the this work differs from the five-point measurements.

Presented in figure 4.12 is the comparison between the five-point and new-multi-wavelength calibration similar to the previous figure. As the reader can see there is roughly an increase of 1% in energy at 10^{18} eV but with no energy correlation, and the uncertainties are relatively large. The uncertainties are the statistical standard deviation of the mean of the

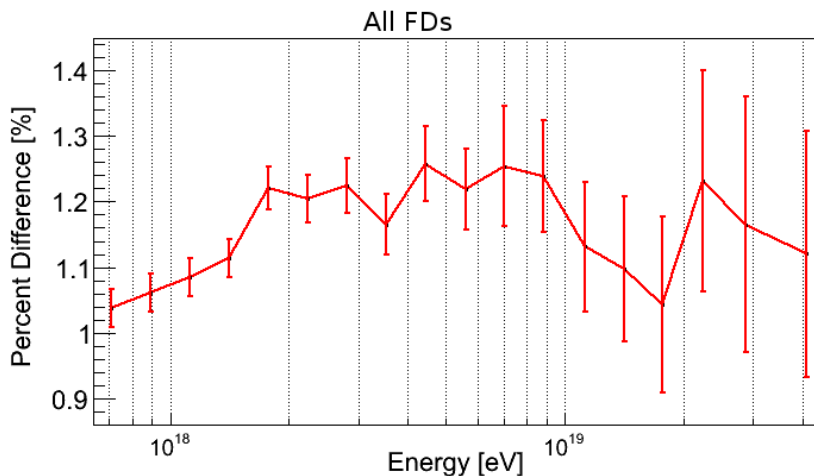
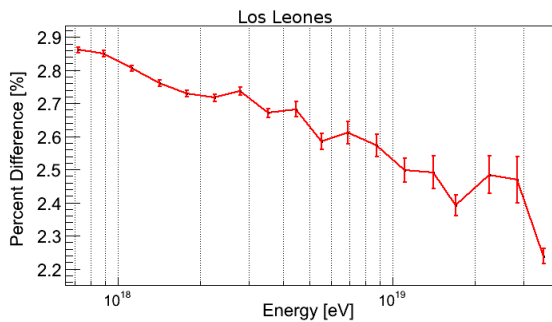


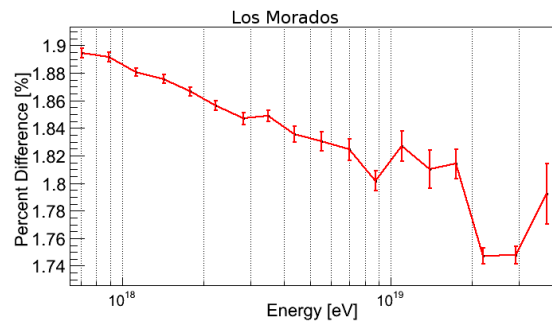
FIGURE 4.12. Comparison between data reconstructed with the five-point and the work presented in this work, as a function of energy.

difference distributions at each energy bin. The increase in energy is expected since all of the calibrations presented in this thesis have wavelength regions that are less efficient than the five-point calibration.

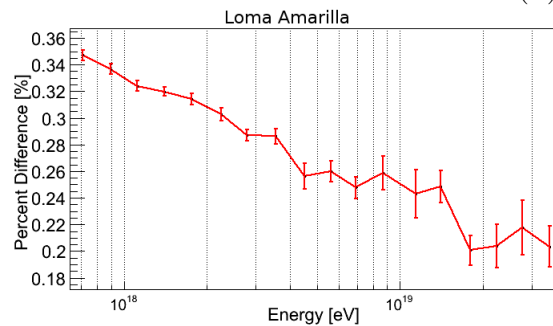
In order to better understand the effect on energy reconstruction, I broke up the new multi-wavelength calibration into its constituent calibration curves: Los Leones, Los Morados



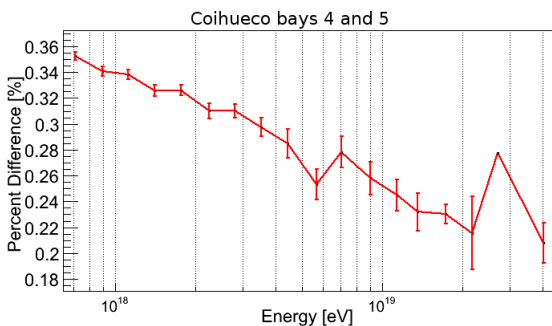
(A) Los Leones



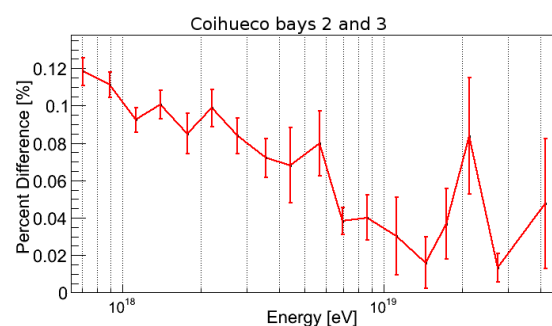
(B) Los Morados



(C) Coihueco bays four and five calibration curve as applied Loma Amarilla.



(D) Coihueco bays four and five, also including bays one and six.



(E) Coihueco bays two and three.

FIGURE 4.13. Difference in reconstructed energy between the five-point calibration and the individual calibrations presented in this thesis as a function of energy.

dos, Coihueco bays four and five, and Coihueco bays two and three. Note that Loma Amarilla uses the Coihueco bays four and five calibration, but since data measured by Loma Amarilla will suffer different atmospheric corrections it has been separated into its own plot. Shown in figure 4.13 are the reconstructed energies from the individual calibration curves compared to the same events as reconstructed with the five-point calibration. The percent difference in energy is the largest for the Los Leones calibration, figure 4.13a, which varies from 2.9% to 2.2%, whereas the curve measured for Coihueco bays two and three, figure 4.13e, yields a negligible difference of less than 0.1% for most energies. Los Morados, figure 4.13b, shows a change of $\sim 2\%$ to 1.75%. There is an overall anti-correlation with increasing energy, however it is not as strong as for the change from the piece-wise to the five-point measurement. From these plots it is clear that the estimation of the uncertainties in figure 4.12 is not valid because there are more than one difference distribution due to the different calibration curves.

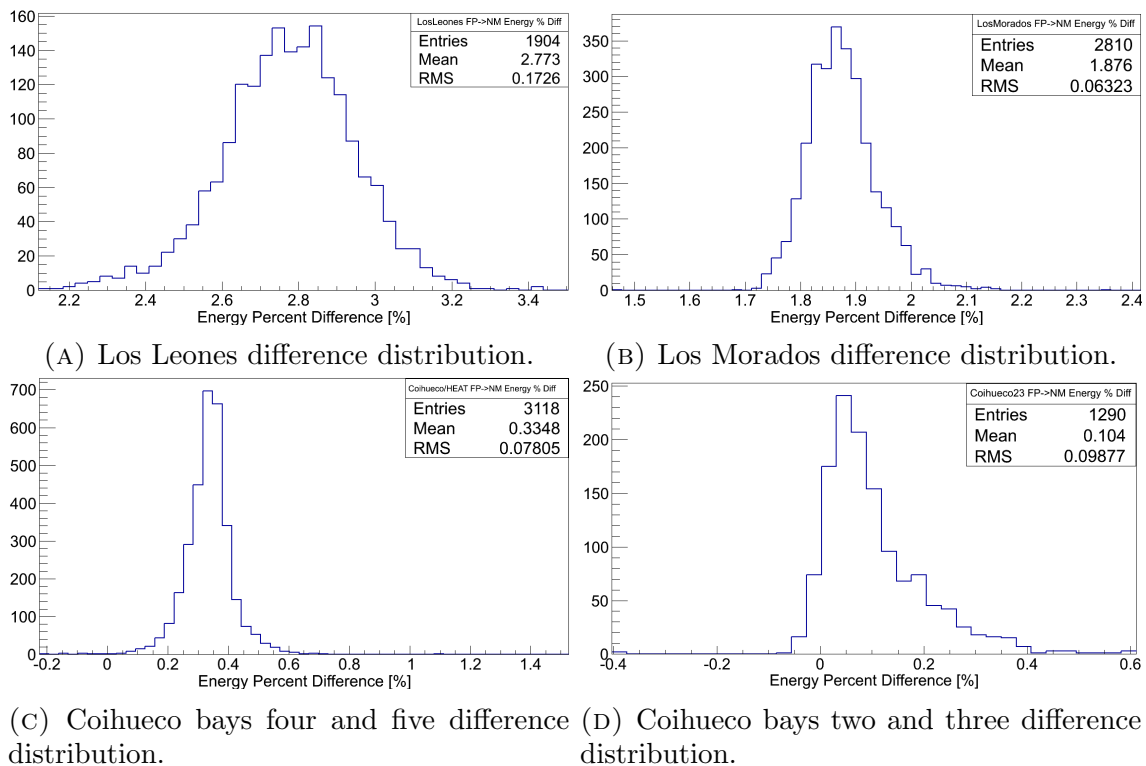


FIGURE 4.14. Percent difference distributions for the new-multi-wavelength calibrations.

Figure 4.14 shows the difference distributions for Los Leones 4.14a, Los Morados 4.14b, Coihueco bays four and five only 4.14c, and Coihueco bays two and three only 4.14d. The statistical uncertainties shown in figure 4.12 span these distributions, and therefore are an overestimation. Events measured at Los Leones and Los Morados will have increased energies by 2.8% and 1.9%, respectively, whereas the rest of the FDs will have a negligible change to their energy reconstruction.

4.3.2.1. *Hybrid Flux.* The increase in the energy scale due to updating the multi-wavelength calibration will affect the flux of cosmic rays as measured by the Auger Observatory, since the flux is the number of events measured per energy for a given energy bin. The number of events in an energy bin, $N(E)_{events}^i$, in expression (4.14),

$$J(E)_i \propto \frac{N(E)_{events}^i}{\Delta E_i} \quad (4.14)$$

will change depending on the reconstructed energy for a given event, and the difference between the calibrations may be enough to significantly affect which events are in which energy bin. For the energy bins used in this calculation, I used the same $\Delta \log(E/\text{eV}) = 0.1$ such that $\Delta E_i \approx 0.1$ up to $10^{19.5}$ eV, and for the $>10^{19.5}$ eV integral bin $\Delta E_i \approx 0.4$. For the three calibrations I calculated the flux for the eighteen energy bins and plotted them as the upper graph of figure 4.15, which is shown on a log-log scale. Since the width of the final bin is larger than the others it is artificially lower based on my definition of flux. I make a quantitative comparison between the flux values by looking at the percent difference in the fluxes calculated using the energies reconstructed with the three multi-wavelength calibrations. The lower plot in figure 4.15 shows the relative change in flux as calculated as the percent differences between the fluxes. The black circles are the differences between the

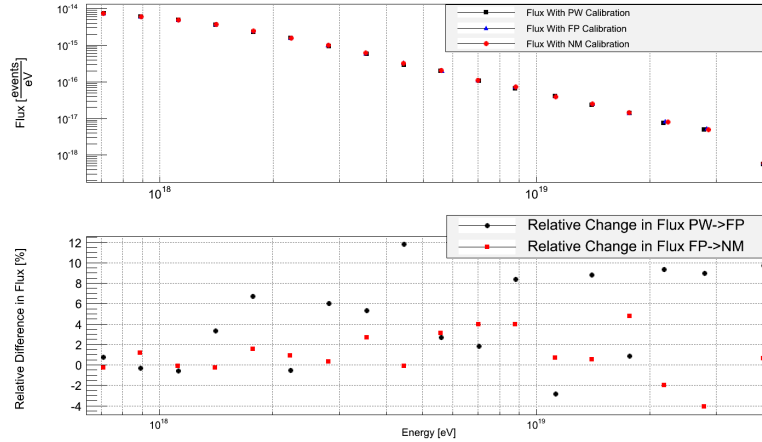


FIGURE 4.15. The upper plot shows the flux calculated by the number of events with an energy falling within a $\Delta\log(E/eV) = 0.1$ bin up to $10^{19.5}$ eV, for which $\Delta\log(E/eV) = 0.4$. The lower plot is the relative changes in flux compared between the three calibrations.

piece-wise and five-point, and the differences between five-point and new-multi-wavelength are the red squares.

The advantage of looking at the relative change between these fluxes is that since these data are for the same set of golden event data, the hybrid exposure is the same for all three reconstructions and divides out, leaving the real change due to the update of the multi-wavelength calibration.

From figure 4.15 a general increase in flux occurs due to updating the multi-wavelength calibration, especially for the piece-wise to five-point transition where there are several bins with an increase of $>8\%$. The changes from the five-point to the new-multi-wavelength are in general lower, especially at the highest energies. Additionally the total number of events between the data reconstructed with the three calibrations are nearly the same such that for increases in flux at the higher energies means the lower energy bins decrease in flux.

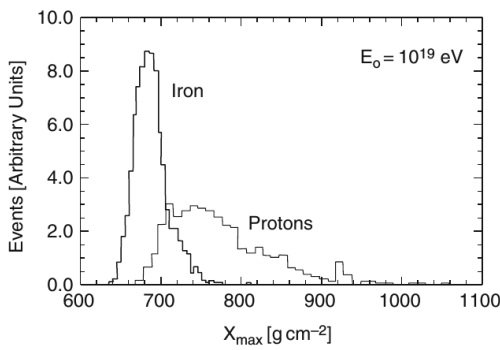
4.3.3. SHOWER MAXIMUM, X_{max} . The FD directly measures the longitudinal profile of an EAS by detecting the number of photons emitted as a function of atmospheric depth.

As explained above, the profile is fitted with a Gaisser-Hillas function and the maximum of that function is the measured value of the shower maximum. X_{max} is related to the primary particle composition through the generalized Heitler model,

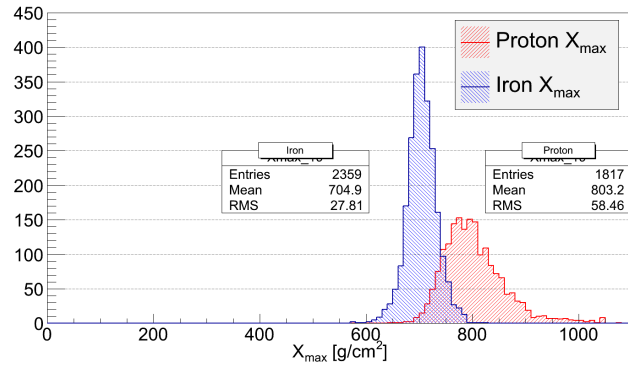
$$\langle X_{max} \rangle = X_0 + D \log \left(\frac{E}{E_0 A} \right) \quad (4.15)$$

where X_0 is the mean depth of proton showers with energy E_0 and D is the elongation rate.

Using this parameterization, known as the superposition model, one readily sees that $\langle X_{max} \rangle$



(A) X_{max} distributions for 500 proton and 1000 iron initiated showers with 10^{19} eV, from [186].



(B) X_{max} distributions of MC event data used in this analysis for proton and iron primaries with an energy of 10^{19} eV

FIGURE 4.16. X_{max} distributions of proton and iron primaries with an energy of 10^{19} eV, showing that the width of the iron X_{max} distribution is smaller, which indicates that the $RMS(\langle X_{max} \rangle)$ can be used for composition studies.

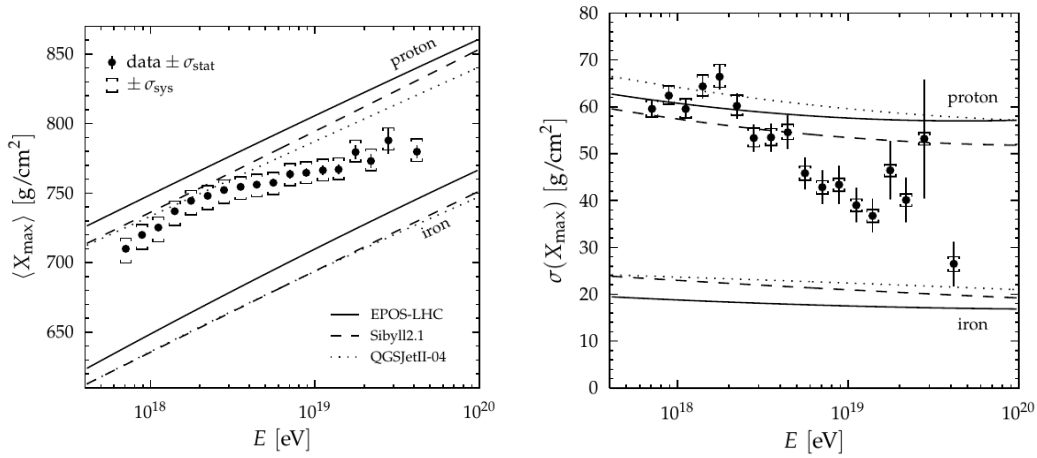
decreases with increasing primary mass. Not only is X_{max} an indication of composition, but the spread, or RMS on measured X_{max} distributions is also a indication of composition.

Figures in 4.16 show two plots of X_{max} distributions for 10^{19} eV proton and iron primaries.

The left figure 4.16a is from [186] and shows the X_{max} distribution for 500 proton showers and 1000 iron showers, and the spread on the iron showers is much less than that of the proton showers. Figure 4.16b on the right are the 10^{19} eV MC event proton and iron data

that have passed quality cuts, which agrees with the statement that the width of the X_{max} distribution for iron is less than that of proton, by almost a factor of two in this case.

As shown in Chapter 2 the latest measurements on $\langle X_{max} \rangle$ and $\text{RMS}(\langle X_{max} \rangle)$ as a function of energy have been made by the Auger Observatory, and are shown again in figure 4.17. For these plots the average values of X_{max} are plotted for the $\Delta \log(E/\text{eV})$ energy bins defined earlier.



(A) Values for $\langle X_{max} \rangle$ for $\Delta \log(E/\text{eV}) = 0.1$ from 17.8 to 19.5 and a integral bin for >19.5 .

(B) $\text{RMS}(\langle X_{max} \rangle)$ for the same energy bins, see text for details about uncertainties.

FIGURE 4.17. Latest measurement on the elongation rate and the RMS of X_{max} , from [128].

The lines in the figures are expectations for proton and iron primaries calculated using various hadronic interaction models, similar to my analysis. Both plots in the figures show a transition to higher mass primaries for higher energies.

The average value of X_{max} for the i^{th} energy bin is determined using the arithmetic mean,

$$\langle X_{max} \rangle_i = \frac{1}{N_i} \sum_{j=1}^{N_{events}} X_{max}^{ij} \quad (4.16)$$

where for the given energy bin, the sum is over the number of events in that bin. The statistical uncertainties in figure 4.17a are the standard deviation of the mean, and the brackets show the systematic uncertainties, which are described in detail in [128]. The standard deviation is calculated using the square root of the variance,

$$V_i = \frac{1}{N_i - 1} \sum_{j=0}^{N_{events}} (X_{max}^{ij} - \langle X_{max} \rangle_i)^2 = \sigma(X_{max})_i^2 \quad (4.17)$$

for each energy bin. For the data in the right figure 4.17b $\sqrt{V_i}$ is plotted as a function of energy, again I refer to [128] for an explanation on the systematic uncertainties, but the statistical uncertainties are estimated using the variance of the variance,

$$\sigma(V_i)^2 = \frac{1}{N_i} \left\{ m_4 - \frac{N_i - 3}{N_i - 1} V_i^2 \right\} \quad (4.18)$$

where m_4 is the fourth moment of the X_{max} distribution for the i^{th} energy bin. The fourth moment is estimated by (4.19) from [187],

$$m_4 = \frac{1}{N_i - 1} \sum_{j=1}^{N_{events}} (X_{max}^{ij} - \langle X_{max} \rangle_i)^4 \quad (4.19)$$

The final statistical uncertainty on the RMS of X_{max} is taken as,

$$\sigma(RMS_{X_{max}})_i = \frac{\sigma(V_i)}{\sqrt{4V_i}} \quad (4.20)$$

which, in general, is slightly larger than the traditional,

$$\sigma(RMS) = \frac{\sigma(V_i)}{\sqrt{2N_i}} \quad (4.21)$$

which is only valid for Gaussian distributions. For each of the multi-wavelength calibrations, I took the X_{max} distributions for the eighteen energy bins and found their mean and variance as described above, and plotted them against the average energy value for the energy bin. Shown appendix B are the overall distributions for the golden data reconstructed with each calibration, starting with the $10^{17.8}$ to $10^{17.9}$ eV in the upper left plot; x-axis is X_{max} in g/cm^2 , and the binning depends on the square root of the number of entries.

Using these data, figure 4.18 shows the values of $\langle X_{max} \rangle$ and $\text{RMS}(\langle X_{max} \rangle)$ plotted as a function of energy, where the energy values for the $\Delta\log(E/\text{eV})=0.1$ are taken as the average energy within that bin. The solid line and dashed line in the figure are the proton and

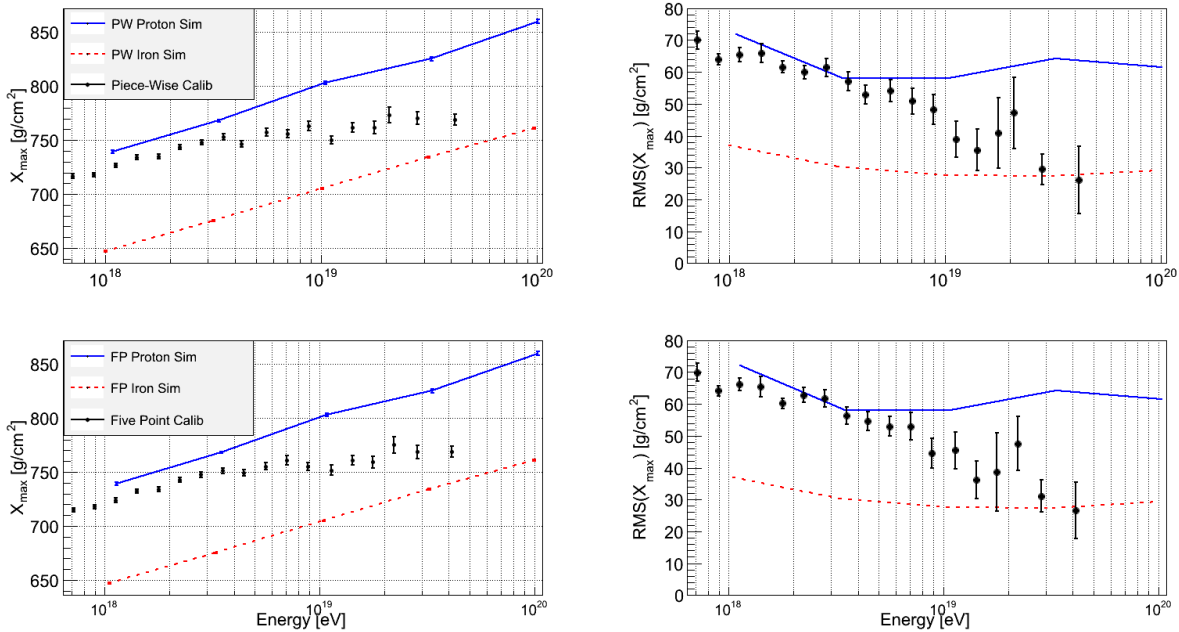


FIGURE 4.18. The left figures show $\langle X_{max} \rangle$ plotted against the 18 $\Delta\log(E/\text{eV})=0.1$ energy bins for the golden data reconstructed with the piece-wise and five-point calibration with the MC expectations for proton, shown in blue, and iron, shown in red. The right figures show $\text{RMS}(\langle X_{max} \rangle)$ plotted for the same energy bins.

iron expectations respectively, similar to figure 4.17, and were reconstructed with the same calibration as the data. Switching to the five-point calibration does not have a qualitative

affect on either of the X_{max} measurements, but to make a quantitative estimate I looked at the difference in reconstructed X_{max} values between the two calibrations.

The data were then compared on an event-by-event basis and the difference between the reconstructed X_{max} values were calculated for each energy bin. In the top plot of figure 4.19 the elongation rates for the piece-wise and five-point calibrations are shown for the eighteen energy bins, where these events are the same between the two calibrations and are used in the difference calculation. The bottom plot of figure 4.19 shows the average difference for each energy bin. The uncertainties are the propagated one sigma values on the respective averages. While these data do seem to show a trend as a function of energy, the value of the calculated difference is always less than 1 g/cm^2 , and this is much less than the 20 g/cm^2 resolution on the X_{max} measurement.

I performed a similar comparison between the five-point calibration and the new-multi-wavelength calibration. From these data, I made a plot of $\langle X_{max} \rangle$ and the $\text{RMS}(\langle X_{max} \rangle)$ as a function of energy as compared to the proton and iron MC expectations as reconstructed with the new-multi-wavelength calibration, and this is shown as the upper two plots in figure 4.20. Then, similar to the energy analysis in section 4.3.2, I broke these data up into the individual FD eyes or calibration curves, such that the rest of the plots in figures 4.20 and 4.21 are the $\langle X_{max} \rangle$ and $\text{RMS}(\langle X_{max} \rangle)$ for the four measured multi-wavelength calibrations presented in this thesis.

The plots in figures 4.20 and 4.21 that show $\langle X_{max} \rangle$ and $\text{RMS}(\langle X_{max} \rangle)$ for each FD or for the individual calibration show qualitative differences, however these are due to the lack of data within a given energy bin for the selected telescopes. For instance the $10^{19.4}$ to $10^{19.5}$ eV bin for Coihueco bay four and five has only two events therefore there is no statistical uncertainty and no associated RMS value in the following plot.

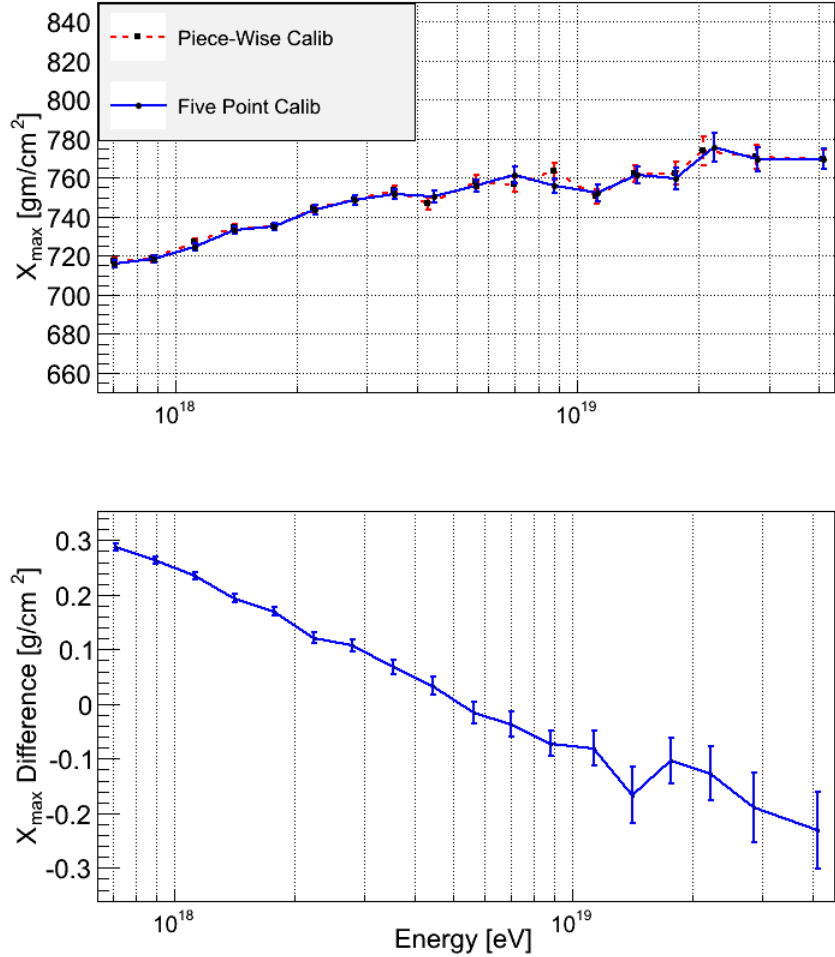


FIGURE 4.19. The top figure shows $\langle X_{max} \rangle$ as a function of energy for the piece-wise and five-point calibrations. The bottom plot shows the difference in $\langle X_{max} \rangle$ as a function of energy between the same golden events reconstructed with the two calibrations.

Shown in figure 4.22 is the event-by-event $\langle X_{max} \rangle$ comparison between the golden event data reconstructed with the five-point and new-multi-wavelength calibrations. There is negligible difference on the reconstructed X_{max} value when comparing the two calibrations, and there is less dependence on energy than in the piece-wise, five-point comparison. Figure 4.23 are the calculated differences between the individual calibration curves and the five-point calibration done on an event-by-event basis. Los Leones has the largest difference out of the five curves, but it is still less than 1 g/cm^2 for all energies, and except for Coihueco bays two and three all of the plots show a slight energy dependence. All of these X_{max} comparisons

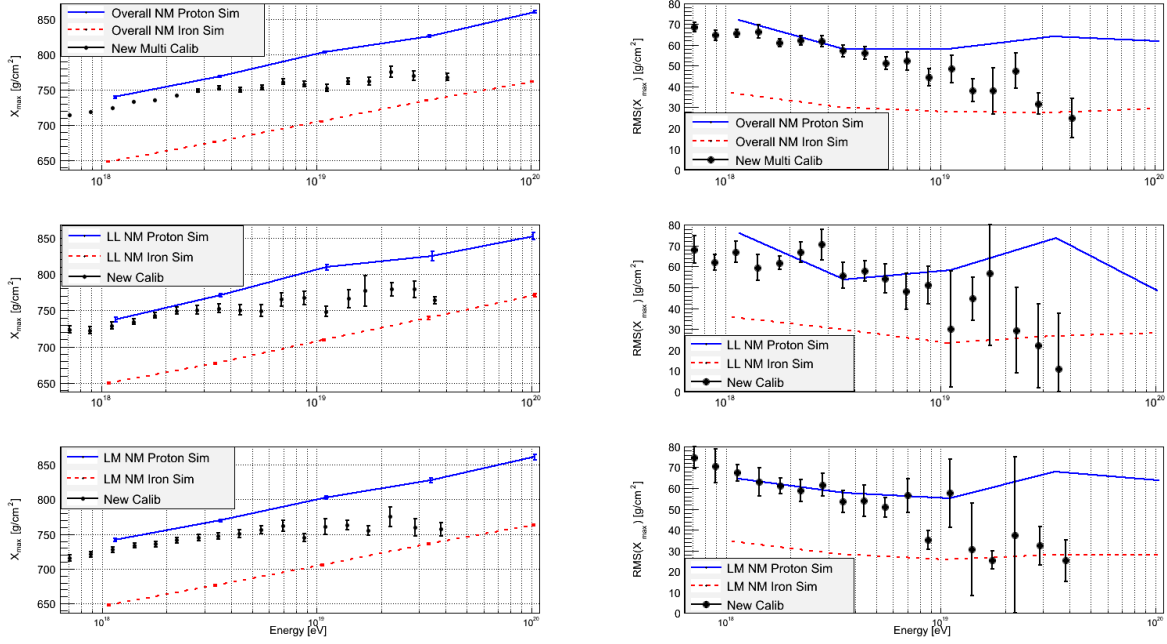


FIGURE 4.20. $\langle X_{max} \rangle$ and $\text{RMS}(\langle X_{max} \rangle)$ as a function of energy for all data using the calibrations curves measured in this work, the top plot. The other plots are for the individual calibration curves, the middle is Los Leones, and the bottom is for Los Morados.

show that there will be a negligible change to the measured shower maximum due to using the work presented in this thesis. Additionally, the widths of the X_{max} distributions in appendix B show that the $\text{RMS}(\langle X_{max} \rangle)$ for each energy bin does not change when the data are compared between the three calibrations.

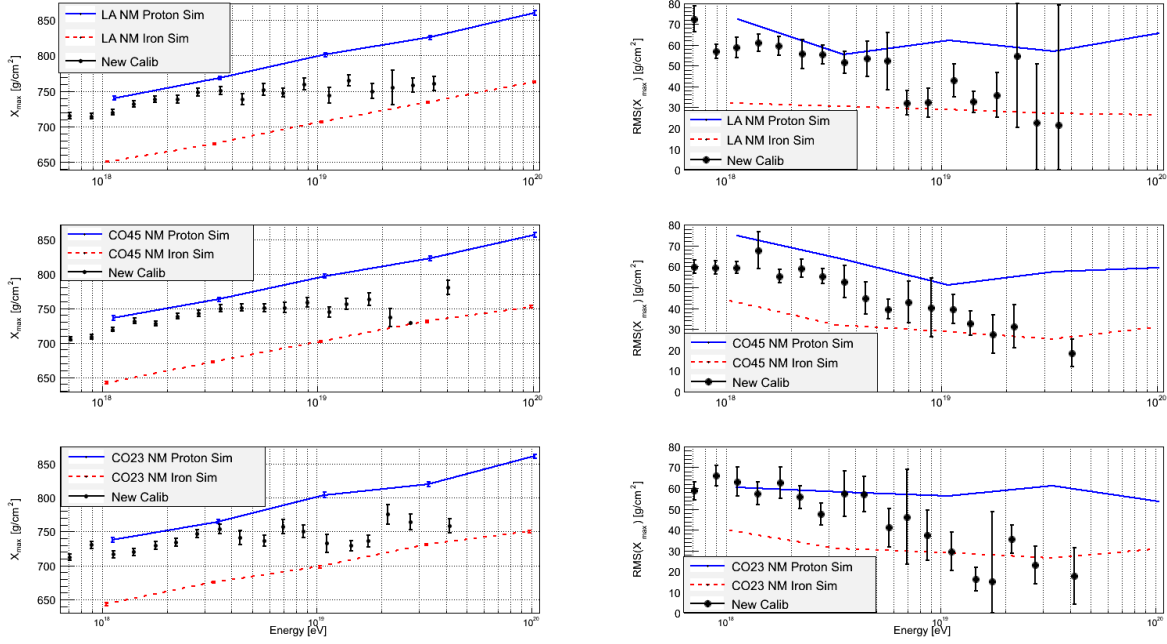


FIGURE 4.21. $\langle X_{max} \rangle$ and RMS ($\langle X_{max} \rangle$) for the calibration curve measured at Coihueco bays four and five as applied to the events measured by those bays and events measured at Loma Amarilla, and then events measured by Coihueco bays two and three using the calibration curve measured at those bays.

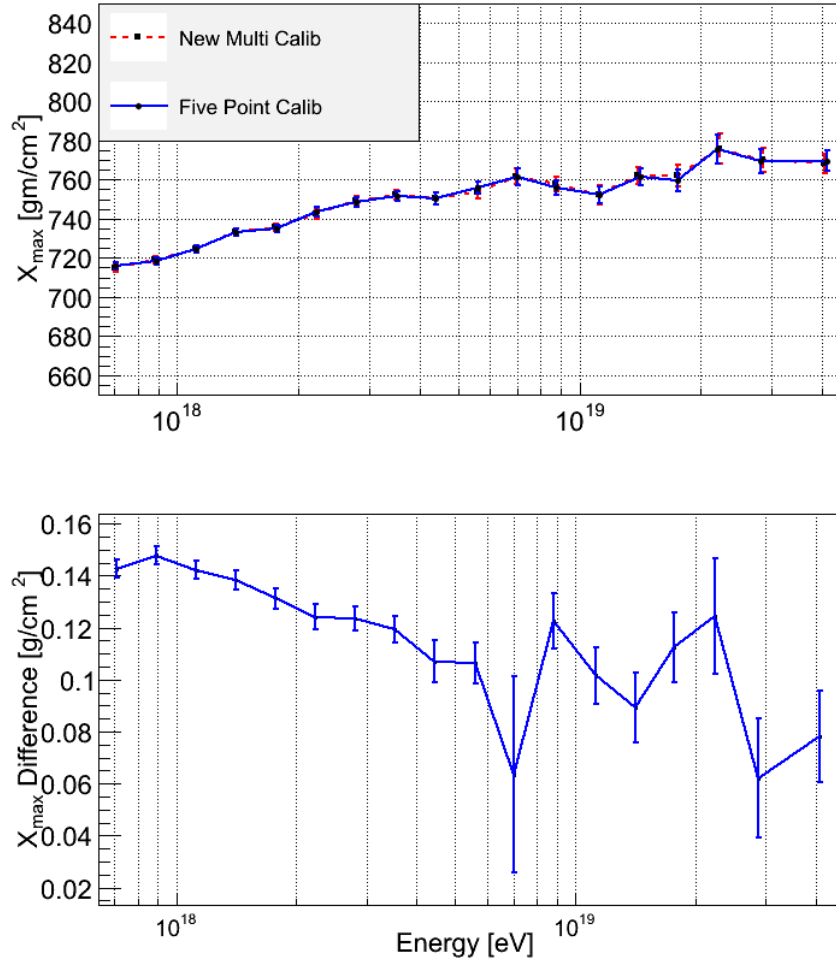
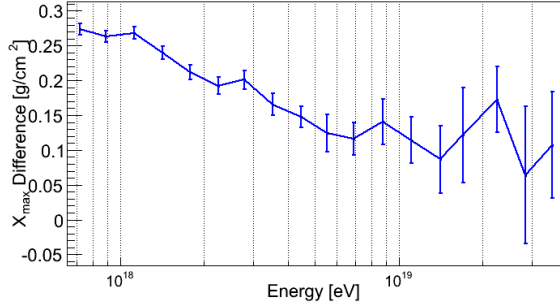
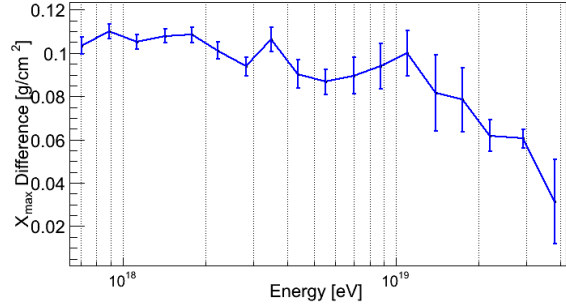


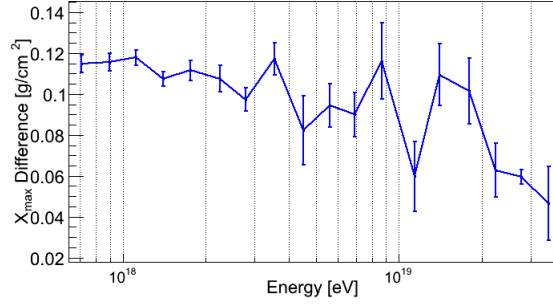
FIGURE 4.22. The top plot shows $\langle X_{max} \rangle$ as a function of energy for the same events for the comparison shown in the lower plot. The lower plot is the calculated average difference in reconstructed X_{max} between the five-point and new-multi-wavelength calibrations.



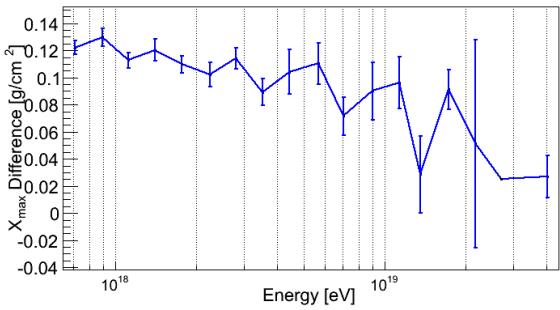
(A) Los Leones



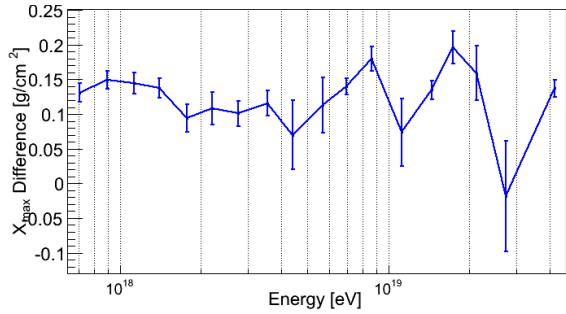
(B) Los Morados



(C) Coihueco bays four and five calibration curve as applied Loma Amarilla.



(D) Coihueco bays four and five, also including bays one and six.



(E) Coihueco bays two and three.

FIGURE 4.23. Difference in reconstructed X_{max} between the five-point calibration and the individual calibrations presented in this thesis as a function of energy.

4.3.4. DISTANCE DEPENDENCE. As mentioned above, due to the steep energy spectrum of cosmic rays and geometry the measured energy for an EAS is dependent on distance, the further away from the FD generally the higher the energy. Shown in figure 4.24 are the reconstructed energy and X_{max} as a function of energy for the three calibrations on the golden data.

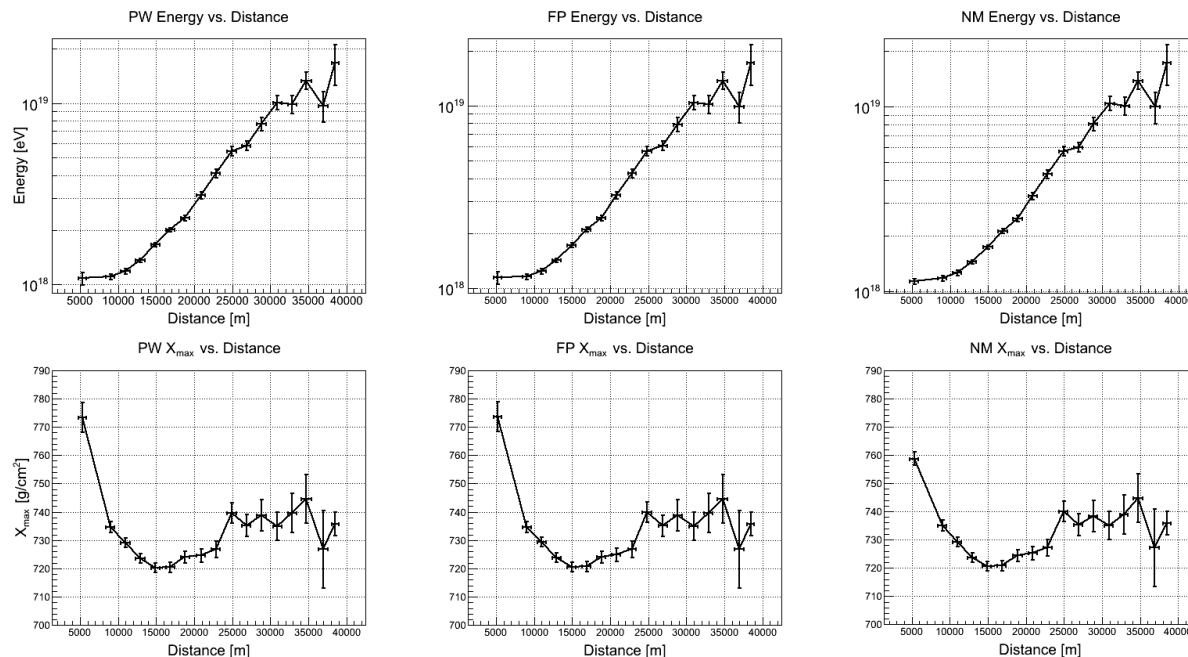


FIGURE 4.24. Energy and X_{max} as a function of distance for golden data using the three multi-wavelength calibrations. Energy increases with increased energy, and X_{max} shows a more complicated dependence on distance.

Showers that are further away from an FD undergo more atmospheric attenuation, and as seen in section 4.1.4 there is a strong wavelength dependence on the attenuation due to Rayleigh scattering. The closer the shower to the detector the more short-wavelength fluorescence light is still in the spectrum, meaning that a change in the detector efficiency at those short wavelengths will affect close showers more. Showers further away will have most of their short wavelengths attenuated away by Rayleigh scattering, diminishing the effect of a change in efficiency at short wavelengths. For the piece-wise to the five-point

calibration change, this is exactly what one expects since only the efficiency at wavelengths less than 380 nm were affected. Figure 4.25 shows the dependence on distance for the percent

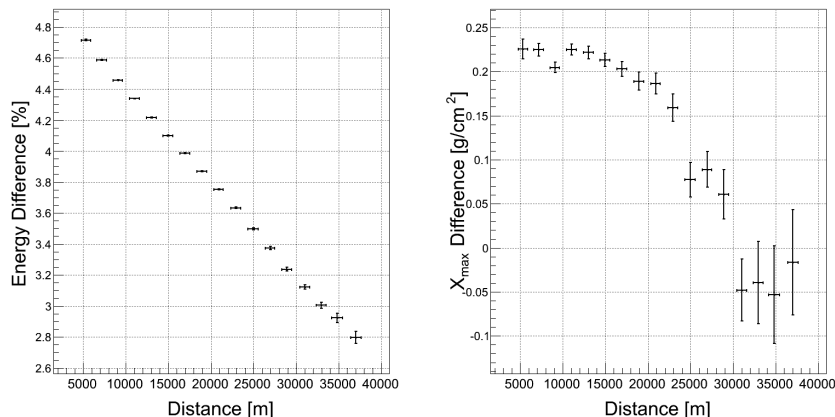


FIGURE 4.25. The change in energy and X_{max} as a function of distance for the update in multi-wavelength calibration from piece-wise to the five-point measurement.

change in energy and the difference in X_{max} for the piece-wise to five-point update in the multi-wavelength calibration. For these data I made an event-by-event comparison for events within 2000 m distance bins, but the first bin goes from 0 m to 6000 m. The uncertainties are the statistical spread in the difference distributions for each bin. The change in energy depends strongly on the distance from the FD, dropping from 4.7% at 6000 m to 2.7% at the furthest distances, whereas X_{max} shows a negligible change and perhaps a dependence on distance.

Again the same comparison for the five-point and new-multi-wavelength calibrations is more complicated due to there being several efficiencies measured as part of this thesis; the same comparison as above for these calibrations yields the data in figure 4.26. Initially there is now an increase in the energy difference up to about 15000 m, and then the difference stays relatively flat. The relationship between the change in energy and distance is once again understood in terms of the difference distributions due to the different calibration curves,

as was the case in section 4.3.2. Shown in figure 4.27 is the difference distribution(s) for

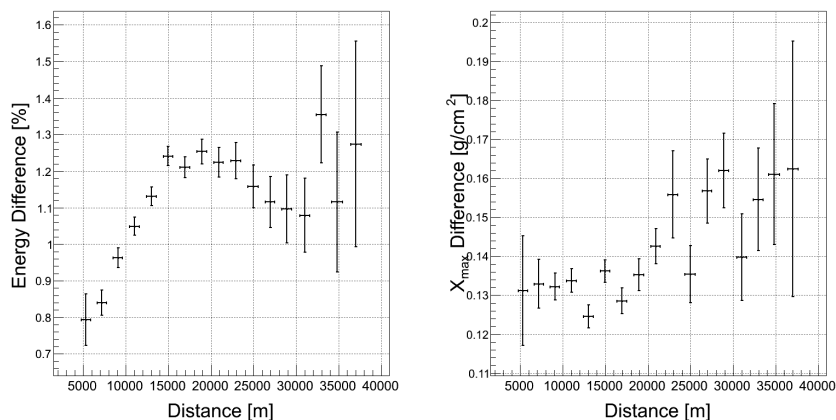
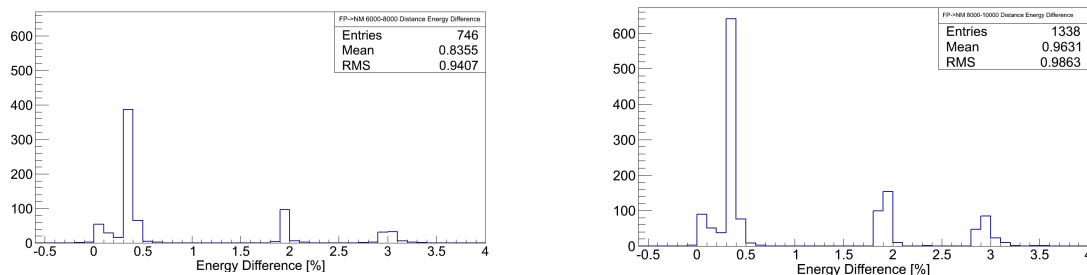


FIGURE 4.26. The change in energy and X_{max} as a function of distance for the update in calibration from the five-point to the work presented in this thesis.

the 6000 m to 8000 m and 8000 m to 10000 m distance bins, where now there are three distributions due to the different efficiencies. Clearly the average will be skewed toward



(A) The 6000 m to 8000 m distance bin energy difference.

(B) The 8000 m to 10000 m distance bin energy difference.

FIGURE 4.27. The difference in energy between the five-point and new-multi-wavelength calibrations for two distance distance bins, clearly showing the three underlying distributions due to the different efficiencies associated with the new-multi-wavelength calibration presented in this work.

the distribution about zero, which is why the left plot of figure 4.26 starts out with a low difference, but for these data as the distance increases for the first several bins the other two distributions around 2% and 3% increase in number of events thereby pulling the average

higher. Figures 4.27a and 4.27b show that while the number of events increase the average difference becomes larger. The distributions about the 2% and 3% change eventually start dropping off due to the same effect as explained above for the piece-wise and five-point comparison, there are fewer short-wavelength photons left in the fluorescence spectrum at large distances, and this explains the decrease in difference above 20000 m in the left plot of figure 4.26.

The individual calibration curves present a similar decrease in the change on energy as

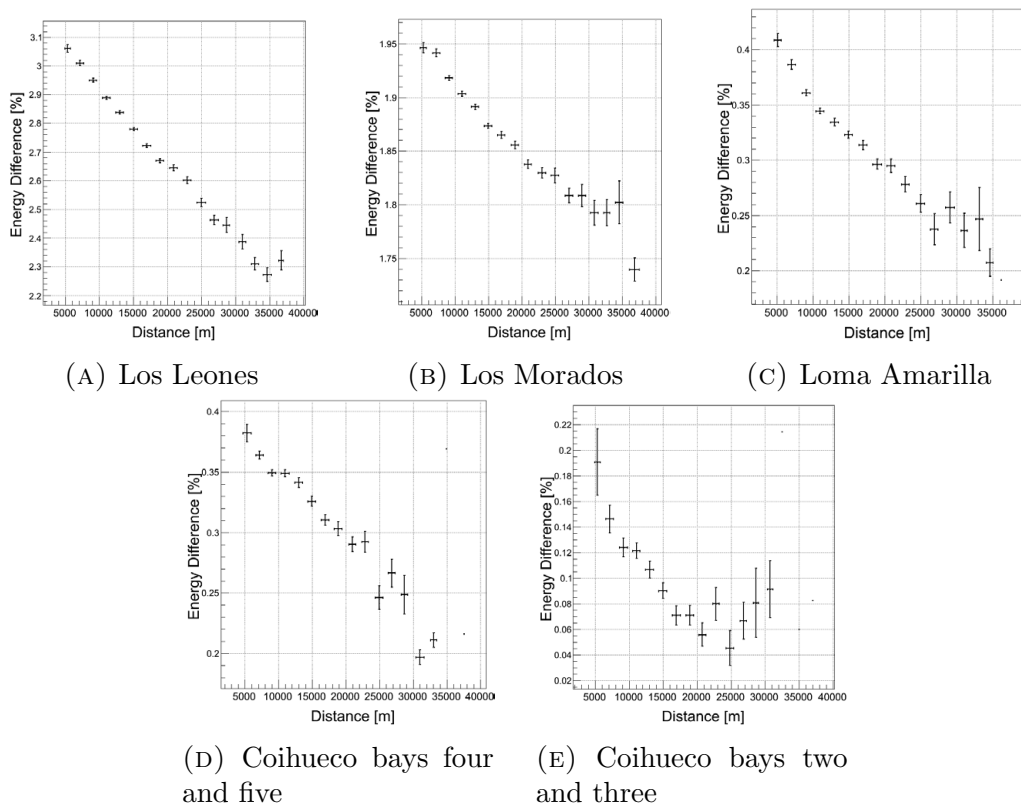


FIGURE 4.28. Difference in reconstructed energy as a function of distance between the five-point calibration and the individual calibrations presented in this thesis.

a function of distance to the piece-wise to five-point change, and little affect on the X_{max} measurement. The event-by-event energy difference comparison of the individual calibration

curves measured as part of this thesis to the same events reconstructed with the five-point calibration are shown in figure 4.28.

4.3.5. AZIMUTH DEPENDENCE. As an EAS traverses the atmosphere it covers tens of kilometers in distance, meaning that light emitted at different times in the shower development are attenuated differently. The previous section described the effect distance has on the change in energy and X_{max} when the multi-wavelength calibration is updated to one with a measured deficiency at shorter wavelengths. It was found that at large distances the effect is diminished because the relevant signal at shorter wavelengths is mostly attenuated away, and the subsequent change in calibration yields no addition of necessary signal. Extending this idea to the distance covered by an EAS means that there will be an increasing amount of signal added as the EAS propagates closer to the FD. The longitudinal position along the shower path where the necessary photons are added will affect the measurement of X_{max} : if it is earlier in the shower development then X_{max} will be smaller, or shallower in the atmosphere, and if they are added later then X_{max} will be deeper in the atmosphere. The energy measurement should only show an overall change as demonstrated in the previous sections as it is an integral over the whole shower path length of the total number of photons detected, it does not care where along the path the photons are emitted.

One way to test for an effect is to look at the change in X_{max} as a function of azimuth, since in general the light detected from showers that are pointed away from an FD will be emitted earlier in the shower development, and therefore be closer to the FD, and vice-versa for showers pointed toward the FD. Figure 4.29 schematically shows that showers pointed away from the FD will in general have the light from the early development of the EAS detected with less atmospheric attenuation than for showers pointed toward the detector. The lower amount of atmospheric attenuation on the short wavelengths for the

light emitted more closely to the FD means that updating the multi-wavelength calibration with a measured deficiency at shorter wavelengths will add more signal at these atmospheric depths. Figure 4.30 shows two real events displaying the toward and away shower geometries for Los Leones as selected by defining azimuthal ranges.

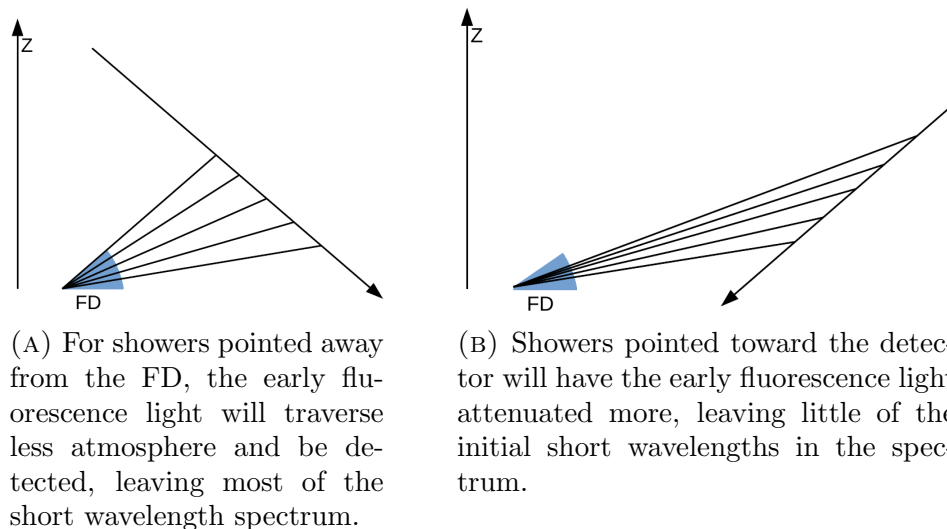


FIGURE 4.29. A schematic showing how the light emitted in the early shower development will be attenuated more for events pointed toward the detector compared to those pointed away. This will lead to an effect in the number of photons detected as a function of atmospheric depth and affect the reconstructed X_{max} .

For the shower geometry shown in figure 4.29a a change in multi-wavelength calibration will move the reconstructed X_{max} shallower since there will be a larger effect on the signal measured early in the shower track. Conversely, the situation in figure 4.29b will lead to a reconstructed X_{max} that is deeper.

In order to investigate this effect on the reconstructed X_{max} values, I performed an event-by-event comparison for between the five-point and the new-multi-wavelength data reconstructions for each of the calibration curves presented in this thesis. I took the difference between the X_{max} values, as defined in expression (4.22), and plotted them as a function of azimuth. Within the coordinate system of the Auger Observatory, 0° in azimuth is defined

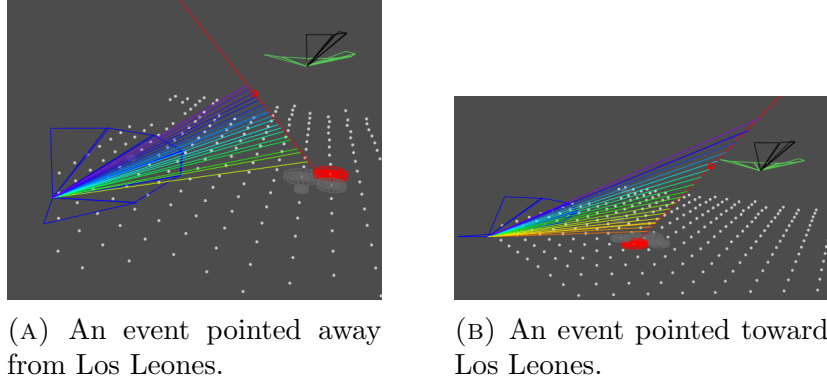
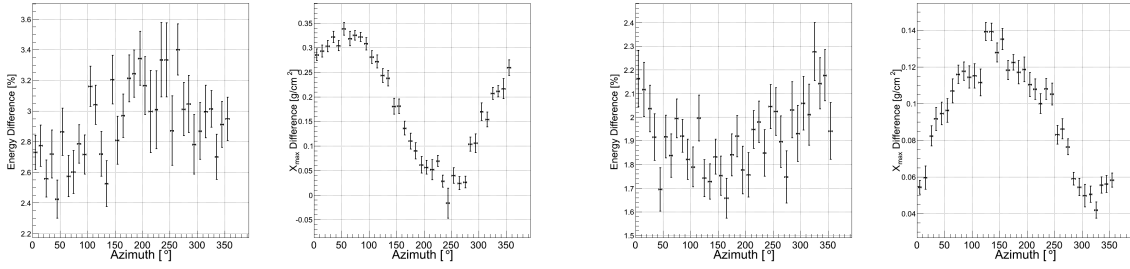


FIGURE 4.30. Real events used in this analysis displayed in the Auger event browser.

to be East and 90° is North.

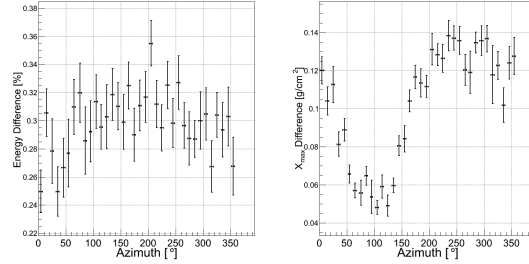
$$\Delta X_{max} = X_{max}^{NewMulti} - X_{max}^{FivePoint} \quad (4.22)$$

Figure 4.31 shows the comparison for each calibration curve, similar to previous sections. The left plot in the figure is the effect on the energy for each calibration curve, and while there may be some azimuthal dependence it is not as strongly correlated as the difference in X_{max} shown in the right plots. The change in the reconstructed X_{max} value when updating to the new-multi-wavelength calibration is not a large effect, the peak to peak variation across all azimuths is less than 1 g/cm^2 at most for the data shown in figure 4.31, and there is little dependence for the difference in energy. As a check, I performed the same comparison for the proton MC data to see if the dependence on azimuth was expected; these data are shown in figure 4.32 for Los Leones only. The effect seen in the reconstructed X_{max} is due to the process outlined above, and to show this, figure 4.33 schematically shows the azimuthal geometry of Los Leones as defined within the Auger coordinate system. The dashed lines in the figure represent the azimuths of the showers giving the extrema in the right plot of figure 4.31a, and based on how the X_{max} difference is defined in (4.22) these events give the

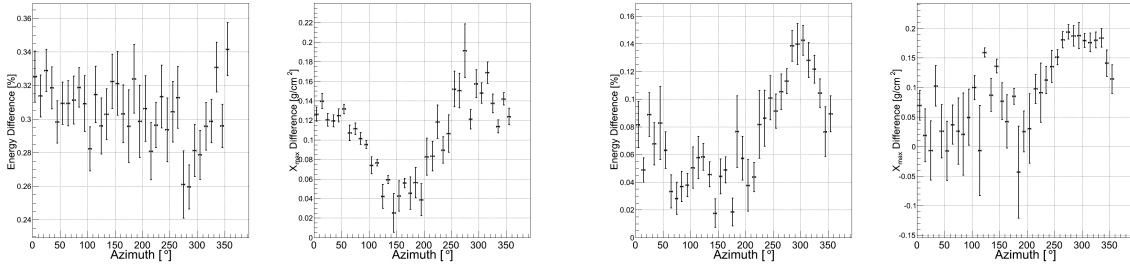


(A) Los Leones.

(B) Los Morados.



(C) Loma Amarilla.



(D) Coihueco bays four and five.

(E) Coihueco bays two and three.

FIGURE 4.31. The azimuthal dependence on the event-by-event comparison between the five-point and new-multi-wavelength calibration in the energy estimation and reconstructed X_{max} .

expected behavior of X_{max} . For all the events pointed toward a given FD the values of X_{max} as reconstructed with the calibrations measured in this work are larger than those from the five-point calibration, meaning that the shower maximum measured are slightly deeper in the atmosphere. For the showers pointed away from the FDs, the values of X_{max} are smaller, meaning the measured shower maximum is higher up in the atmosphere.

For completeness, I performed the same event-by-event comparison between the piecewise and five-point calibrations for the energy estimation and the reconstructed X_{max} . Shown

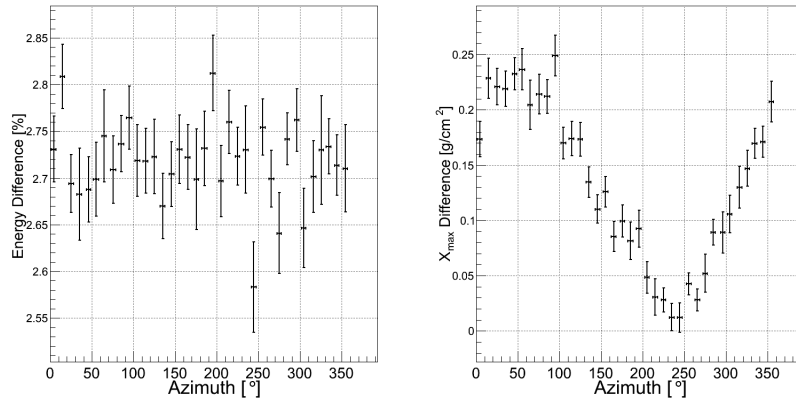
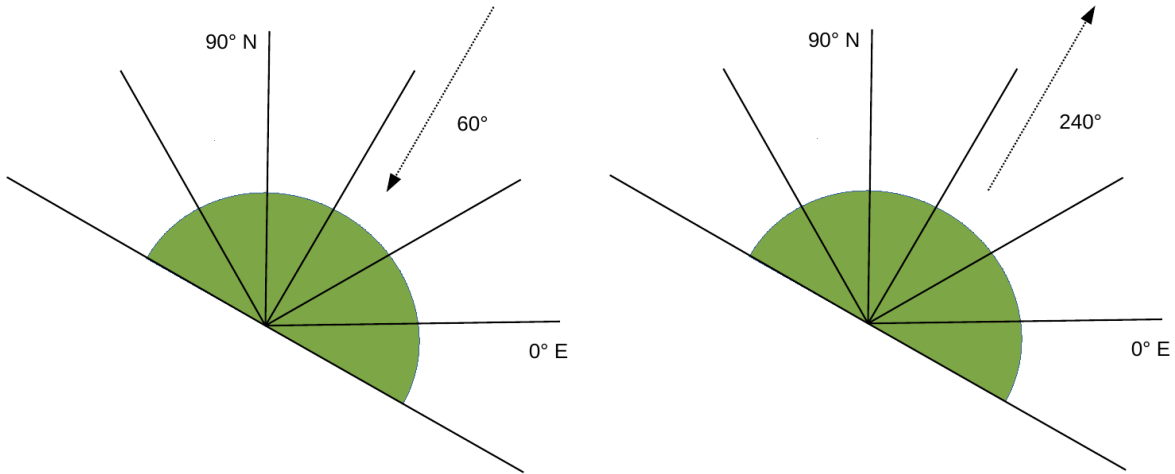


FIGURE 4.32. Azimuth dependence on the comparison between the five-point and the new-multi-wavelength calibrations on energy and X_{max} for the MC proton event data for Los Leones.



(A) The shower geometry in which the reconstructed X_{max} is slightly deeper in the atmosphere when the calibration is updated.

(B) The shower geometry where X_{max} is shallower in the atmosphere with an updated calibration.

FIGURE 4.33. Azimuthal geometry for Los Leones depicting the shower geometry, as the dashed arrows, for the maximum and minimum of the difference in the X_{max} measurements. Each wedge represents the field of view of a telescope.

in figure 4.34 is the comparison between the energy estimation for the golden data, again showing little dependence on azimuth. The difference in the X_{max} values are shown in figure 4.35 and the dependence on azimuth is clearly seen, and is more well defined than the comparison between the five-point and new-multi-wavelength calibrations. The extrema in the plots again correspond to the showers pointing toward and away from the FDs, and have

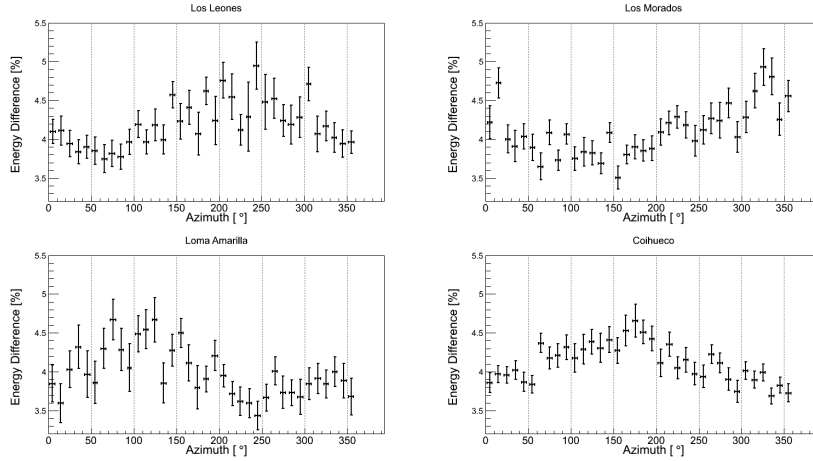


FIGURE 4.34. Energy comparison between the piece-wise and five-point calibrations.

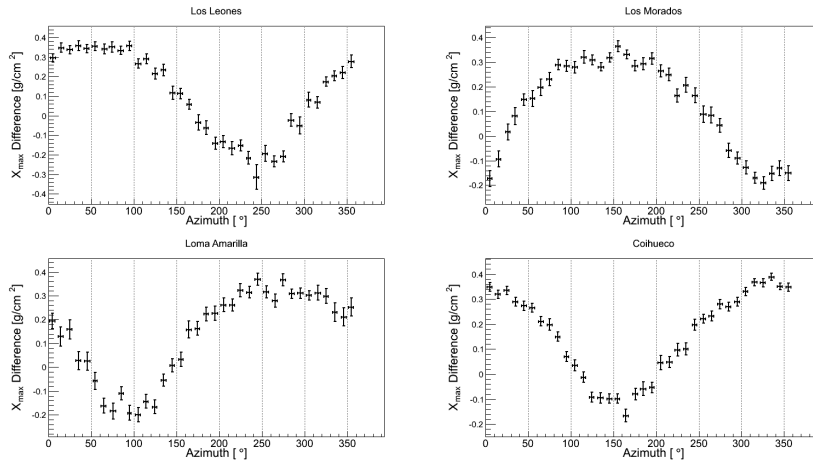


FIGURE 4.35. X_{max} comparison between the piece-wise and five-point calibrations.

a variation of nearly 1 g/cm^2 . Los Morados and Coihueco are 180° out of phase, which makes sense since those two FDs point at one another, whereas Los Leones and Loma Amarilla are not quite since they do not exactly point at one another.

The implications of the measured differences in the FD energy estimation and the reconstructed X_{max} due to updating the multi-wavelength calibration will be discussed in the following chapter.

CHAPTER 5

CONCLUSIONS

Most of the work detailed in this thesis dealt with the calibration of the Auger Observatory fluorescence detectors. The two calibrations, absolute and multi-wavelength, led to a better understanding of the detector(s), and will allow them to measure extensive air showers with the highest precision.

5.1. ABSOLUTE FD CALIBRATION

While the technique for the absolute calibration of the FDs was mature at the time of my work, I was integral to the implementation of the $1/r^2$ technique used to calibrate the photon flux emitted from the drum. By using the new technique, developing new hardware and software to control the LED, the uncertainty associated with the drum calibration dropped from 6% to 2.1%, and led to the FD absolute calibration having an overall 4% uncertainty. We demonstrated that the absolute FD calibration is stable over long periods of time, several years, through the tracking performed by the relative Cal A.

5.2. DETAILED MULTI-WAVELENGTH CALIBRATION

The idea of using a monochromator to select out the wavelengths from a broad UV spectrum was first proposed prior to the work using the notch filters. It was only recently that using a monochromator in conjunction with the drum became feasible through software and hardware development. The fully automated monochromator scanning and data acquisition, which I developed, allowed for a highly robust drum spectrum measurement and FD calibration. Systematics associated with the spectrum measurement and the multi-wavelength calibration were minimized through our highly repeatable technique.

5.2.1. EFFECT ON FD PHYSICS MEASUREMENTS. When updating to the multi-wavelength calibration measurements presented in this thesis, there will be effects on the energy and X_{max} measurements made by the Pierre Auger Observatory.

The energy estimation made by the FD undergoes a relatively small increase when updating from the five-point to the measurements presented in this work. Overall there is a $\sim 1\%$ change in the energy at 10^{18} eV for the Golden data used in this analysis, and when comparing events only measured by Los Leones and Los Morados the difference is 2.8% and 1.9%, respectively. The calibrations applied to Coihueco and Loma Amarilla show less than a 1% change in energy. The relative change in flux as measured by the FD undergoes a smaller change for the $\Delta \log(E/eV)=0.1$ energy bins when changing from the five-point to the new-multi-wavelength calibrations than the piece-wise to five-point change in calibrations. The distance dependence on the change in energy is as expected, where for showers closer to the FD the effect is larger than further away due to the short wavelength signal attenuating away. There is little dependence on azimuth for the change in energy due to the FD energy estimation being a calorimetric measure.

Updating to the detailed new-multi-wavelength calibrations effects the reconstructed X_{max} by less than 0.5 g/cm^2 overall for all energies, and when examining the individual calibration curves, Los Leones has the largest change of 0.27 g/cm^2 at 10^{18} eV. There is little dependence on distance for the new measurements of X_{max} . The most intriguing result was the effect the new calibrations had on the reconstructed X_{max} for showers pointed toward and away from a given FD. The more detailed measurements of the FD efficiencies showed a decrease in detector efficiency at shorter wavelengths; this coupled with Rayleigh attenuation over the track length of the shower through the atmosphere, meant that signal is added in differential amounts along the reconstructed shower axis. For the geometries

pointed toward and away from a given FD, the reconstructed X_{max} was deeper or shallower, respectively, although the difference is less than 0.5 g/cm^2 .

5.3. OUTLOOK

The changes on measurements made by the Auger Observatory as described in this analysis are critical to the success of the experiment. With the calibrations described in this work in place, the Observatory will operate for several years to come with the best understanding of the FD. The detailed multi-wavelength calibrations measured as part of this work are the most accurate and precise measurement of the FD efficiencies to date, and will serve to better understand cosmic rays and the mysteries surrounding them.

BIBLIOGRAPHY

- [1] P. Auger and M. Shapiro, *What are cosmic rays?* University of Chicago press, 1945.
- [2] A. H. Becquerel, “On the invisible radiation ’e made by phosphorescent bodies,” *CR Acad. Sci. Paris*, vol. 122, p. 501, 1896.
- [3] P. Curie and M. S. Curie, “On a new radioactive substance contained in pitchblende,” *Comptes Rendus*, vol. 127, pp. 175–178, 1898.
- [4] A. H. Becquerel, “On radioactivity, a new property of matter,” *Les prix Nobel*, 1903.
- [5] W. Crookes, “On Electrical Insulation in High Vacua,” *Proceedings of the Royal Society of London*, vol. 28, no. 190-195, pp. 347–352, 1878.
- [6] C. T. R. Wilson, “On the ionisation of atmospheric air,” *Proceedings of the Royal Society of London*, vol. 68, no. 442-450, pp. 151–161, 1901.
- [7] M. Curie, “Rays emitted by compounds of uranium and thorium,” *Comptes Rendus de Seances de l’academie de Sciences*, vol. 126, no. 1, pp. 101–1, 1898.
- [8] D. Pacini *Le Radium*, vol. 8, p. 307, 1911.
- [9] M. W. Friedlander and M. W. Friedlander, *A thin cosmic rain particles from outer space*. Harvard University Press, 2000.
- [10] T. Wulf *Phys. Z.*, vol. 11, p. 811, 1910.
- [11] V. Hess *Phys. Z.*, vol. 13, p. 1084, 1912.
- [12] A. Hillas, ed., *Cosmic Rays*, p. 139. Pergamon, 1972.
- [13] W. Kolhörster *Verh. Dtch. Phys. Ges.*, vol. 15, p. 1111, 1913.
- [14] W. Kolhörster *Verh. Dtch. Phys. Ges.*, vol. 16, p. 719, 1914.
- [15] R. M. Otis, *The source of the penetrating radiation found in the earth’s atmosphere*. PhD thesis, California Institute of Technology, 1924.

- [16] R. Millikan and G. Cameron, “New results on cosmic rays,” *Nature*, vol. 121, no. 3036, pp. 19–26, 1928.
- [17] H. Geiger and W. Müller, “Das Elektronenzählrohr,” *Phys. Zs*, vol. 29, p. 839, 1928.
- [18] W. Bothe and W. Kolhörster, “Das wesen der höhenstrahlung,” *Zeitschrift für Physik*, vol. 56, no. 11-12, pp. 751–777, 1929.
- [19] J. Aitken, *Collected scientific papers of John Aitken...* The University Press, 1923.
- [20] P. Coulier, “Note sur une nouvelle propriété de l’air,” *Journal de Pharmacie et de Chimie*, vol. 22, pp. 165–173, 1875.
- [21] J. J. Thomson, “LVII. On the charge of electricity carried by the ions produced by Röntgen rays,” *The London, Edinburgh, and Dublin Philosophical Magazine and Journal of Science*, vol. 46, no. 283, pp. 528–545, 1898.
- [22] C. T. R. Wilson, “LXXV. The condensation method of demonstrating the ionisation of air under normal conditions,” *The London, Edinburgh, and Dublin Philosophical Magazine and Journal of Science*, vol. 7, no. 42, pp. 681–690, 1904.
- [23] C. Wilson, “Cloud-chamber technique,” in *Proc. Roy Soc*, vol. 85, p. 285, 1911.
- [24] D. Skobelczyn, “Distribution of Intensity in the Spectrum of gamma-Rays,” *Nature*, vol. 118, pp. 553–554, 1926.
- [25] C. D. Anderson, “The positive electron,” *Physical Review*, vol. 43, no. 6, p. 491, 1933.
- [26] P. A. Dirac, “The quantum theory of the electron,” *Proceedings of the Royal Society of London. Series A, Containing Papers of a Mathematical and Physical Character*, pp. 610–624, 1928.
- [27] S. H. Neddermeyer and C. D. Anderson, “Note on the nature of cosmic-ray particles,” *Physical Review*, vol. 51, no. 10, pp. 884–886, 1937.

- [28] J. Street and E. Stevenson, “New evidence for the existence of a particle of mass intermediate between the proton and electron,” *Physical Review*, vol. 52, no. 9, p. 1003, 1937.
- [29] H. Yukawa, “Interaction of elementary particles. Part I,” in *Proc. Phys. Math. Soc. Jpn.*, vol. 17, pp. 48–57, 1935.
- [30] C. M. G. Lattes, G. Occhialini, and C. F. Powell, “Observations on the tracks of slow mesons in photographic emulsions,” *Nature*, vol. 160, no. 4066, pp. 453–456, 1947.
- [31] G. Rochester and C. C. Butler, “Evidence for the existence of new unstable elementary particles,” *Nature*, vol. 160, no. 4077, p. 855, 1947.
- [32] P. M. Blackett and G. Occhialini, “Some photographs of the tracks of penetrating radiation,” *Proceedings of the Royal Society of London. Series A*, vol. 139, no. 839, pp. 699–726, 1933.
- [33] P. Auger and R. Maze, “Extensive cosmic showers in the atmosphere,” *CR Acad. Sci. II*, vol. 207, pp. 228–229, 1938.
- [34] N. R. Ikhsanov, “Particle acceleration and main parameters of ultra-high energy gamma-ray binaries,” *Astrophysics and space science*, vol. 184, no. 2, pp. 297–311, 1991.
- [35] R. Atkins, W. Benbow, D. Berley, E. Blaufuss, J. Bussons, D. Coyne, T. DeYoung, B. Dingus, D. Dorfan, R. Ellsworth, *et al.*, “TeV gamma-ray survey of the northern hemisphere sky using the milagro observatory,” *The Astrophysical Journal*, vol. 608, no. 2, p. 680, 2004.
- [36] A. Tepe, H. Collaboration, *et al.*, “HAWC—The High Altitude Water Cherenkov Detector,” in *Journal of Physics: Conference Series*, vol. 375, p. 052026, IOP Publishing, 2012.

- [37] W. Heitler, *The quantum theory of radiation*. Courier Dover Publications, 1954.
- [38] A. Haungs, H. Rebel, and M. Roth, “Energy spectrum and mass composition of high-energy cosmic rays,” *Reports on Progress in Physics*, vol. 66, no. 7, p. 1145, 2003.
- [39] J. Alvarez-Muniz, R. Engel, T. Gaisser, J. A. Ortiz, and T. Stanev, “Hybrid simulations of extensive air showers,” *Physical Review D*, vol. 66, no. 3, p. 033011, 2002.
- [40] J. Matthews, “A Heitler Model of Extensive Air Showers,” *Astroparticle Physics*, 2005.
- [41] J. Engel, T. K. Gaisser, P. Lipari, and T. Stanev, “Nucleus-nucleus collisions and interpretation of cosmic-ray cascades,” *Phys. Rev. D*, vol. 46, pp. 5013–5025, Dec 1992.
- [42] T. K. Gaisser, *Cosmic rays and particle physics*. Cambridge University Press, 1990.
- [43] M. Schein, W. P. Jesse, and E. O. Wollan, “The nature of the primary cosmic radiation and the origin of the mesotron,” *Physical Review*, vol. 59, no. 7, p. 615, 1941.
- [44] H. Bradt and B. Peters, “Investigation of the primary cosmic radiation with nuclear photographic emulsions,” *Physical Review*, vol. 74, no. 12, p. 1828, 1948.
- [45] R. W. Williams, “The structure of the large cosmic-ray air showers,” *Physical Review*, vol. 74, no. 11, p. 1689, 1948.
- [46] L. Wolfenstein, “Theoretical Calculations on Extensive Atmospheric Cosmic-Ray Showers,” *Phys. Rev.*, vol. 67, pp. 238–247, Apr 1945.
- [47] P. Bassi, G. Clark, and B. Rossi, “Distribution of arrival times of air shower particles,” *Physical Review*, vol. 92, no. 2, p. 441, 1953.
- [48] G. Clark, J. Earl, W. Kraushaar, J. Linsley, B. Rossi, and F. Scherb, “The MIT air shower program,” *Il Nuovo Cimento (1955-1965)*, vol. 8, pp. 623–652, 1958.
- [49] G. Clark, J. Earl, W. Kraushaar, J. Linsley, B. Rossi, and F. Scherb, “An experiment on air showers produced by high-energy cosmic rays,” *Nature*, vol. 180, pp. 406–409, 1957.

- [50] J. Linsley and L. Scarsi, “Arrival Times of Air Shower Particles at Large Distances from the Axis,” *Phys. Rev.*, vol. 128, pp. 2384–2392, Dec 1962.
- [51] G. Clark, J. Earl, W. Kraushaar, J. Linsley, B. Rossi, F. Scherb, and D. Scott, “Cosmic-ray air showers at sea level,” *Physical Review*, vol. 122, no. 2, p. 637, 1961.
- [52] D. Krasilnikov, A. Kuzmin, V. Orlov, J. Linsley, R. Reid, A. Watson, and J. Wilson, “Evidence of an anisotropy in the arrival direction of cosmic rays with energies above 1019 eV,” *Journal of Physics A: Mathematical, Nuclear and General*, vol. 7, no. 18, p. L176, 1974.
- [53] O. Adriani, M. Ambriola, G. Barbarino, L. Barbier, S. Bartalucci, G. Bazilevskaja, R. Bellotti, S. Bertazzoni, V. Bidoli, M. Boezio, *et al.*, “The PAMELA experiment on satellite and its capability in cosmic rays measurements,” *Nuclear Instruments and Methods in Physics Research Section A: Accelerators, Spectrometers, Detectors and Associated Equipment*, vol. 478, no. 1, pp. 114–118, 2002.
- [54] F. Cadoux, F. Cervelli, V. Chambert-Hermel, G. Chen, H. Chen, G. Coignet, S. Di Falco, J. Dubois, E. Falchini, A. Franzoso, *et al.*, “The AMS-02 electromagnetic calorimeter,” *Nuclear Physics B-Proceedings Supplements*, vol. 113, no. 1, pp. 159–165, 2002.
- [55] A. A. Abdo, M. Ackermann, W. Atwood, L. Baldini, J. Ballet, G. Barbiellini, M. Baring, D. Bastieri, B. Baughman, K. Bechtol, *et al.*, “The Fermi gamma-ray space telescope discovers the pulsar in the young galactic supernova remnant CTA 1,” *Science*, vol. 322, no. 5905, pp. 1218–1221, 2008.
- [56] M. Nagano and A. Watson, “Observations and implications of the ultrahigh-energy cosmic rays,” *Reviews of Modern Physics*, vol. 72, no. 3, p. 689, 2000.

- [57] A. Strong, J. Wdowczyk, and A. Wolfendale, “The gamma-ray background: a consequence of metagalactic cosmic ray origin?,” *Journal of Physics A: Mathematical, Nuclear and General*, vol. 7, no. 1, p. 120, 1974.
- [58] W. Tkaczyk, J. Wdowczyk, and A. Wolfendale, “Extragalactic heavy nuclei in cosmic rays?,” *Journal of Physics A: Mathematical and General*, vol. 8, no. 9, p. 1518, 1975.
- [59] T. K. Gaisser, T. Stanev, and S. Tilav, “Cosmic ray energy spectrum from measurements of air showers,” *Frontiers of Physics*, vol. 8, no. 6, pp. 748–758, 2013.
- [60] M. E. Newman, “Power laws, pareto distributions and zipf’s law,” *Contemporary physics*, vol. 46, no. 5, pp. 323–351, 2005.
- [61] E. Fermi, “On the Origin of the Cosmic Radiation,” *Phys. Rev.*, vol. 75, pp. 1169–1174, Apr 1949.
- [62] E. Berezhko, S. Petukhov, and S. Taneev, “Shock acceleration of energetic particles in solar corona,” in *International Cosmic Ray Conference*, vol. 8, pp. 3215–3218, 2001.
- [63] L. G. Sveshnikova, “The knee in galactic cosmic ray spectrum and variety in supernovae,” *arXiv preprint astro-ph/0303159*, 2003.
- [64] E. Berezhko and H. Voelk, “Spectrum of cosmic rays, produced in supernova remnants,” *Astrophys.J.*, vol. 661, p. L175, 2007.
- [65] A. Hillas, “The origin of ultra-high-energy cosmic rays,” *Annual Review of Astronomy and Astrophysics*, vol. 22, pp. 425–444, 1984.
- [66] T. Wibig and A. W. Wolfendale, “At what particle energy do extragalactic cosmic rays start to predominate?,” *Journal of Physics G: Nuclear and Particle Physics*, vol. 31, no. 3, p. 255, 2005.

- [67] A. Hillas, “Can diffusive shock acceleration in supernova remnants account for high-energy galactic cosmic rays?,” *Journal of Physics G: Nuclear and Particle Physics*, vol. 31, no. 5, p. R95, 2005.
- [68] A. Hillas, “Cosmic rays: Recent progress and some current questions,” *arXiv preprint astro-ph/0607109*, 2006.
- [69] L. Anchordoqui, T. Paul, S. Reucroft, and J. Swain, “Ultrahigh energy cosmic rays: The state of the art before the auger observatory,” *International Journal of Modern Physics A*, vol. 18, no. 13, pp. 2229–2366, 2003.
- [70] A. A. Penzias and R. W. Wilson, “A measurement of excess antenna temperature at 4080 mc/s.,” *The Astrophysical Journal*, vol. 142, pp. 419–421, 1965.
- [71] K. Greisen, “End to the Cosmic-Ray Spectrum?,” *Phys. Rev. Lett.*, vol. 16, pp. 748–750, Apr 1966.
- [72] G. Zatsepin and V. Kuz’min, “Upper limit of the spectrum of cosmic rays,” *JETP Lett.(USSR)(Engl. Transl.)*, vol. 4, 1966.
- [73] M. Takeda, N. Hayashida, K. Honda, N. Inoue, K. Kadota, F. Kakimoto, K. Kamata, S. Kawaguchi, Y. Kawasaki, N. Kawasumi, *et al.*, “Extension of the cosmic-ray energy spectrum beyond the predicted greisen-zatsepin-kuz’min cutoff,” *Physical Review Letters*, vol. 81, no. 6, p. 1163, 1998.
- [74] R. Abbasi, T. Abu-Zayyad, M. Allen, J. Amman, G. Archbold, K. Belov, J. Belz, S. B. Zvi, D. Bergman, S. Blake, *et al.*, “First observation of the Greisen-Zatsepin-Kuzmin suppression,” *Physical Review Letters*, vol. 100, no. 10, p. 101101, 2008.
- [75] C. Bell, A. Bray, S. David, B. Denehy, L. Goorevich, L. Horton, J. Loy, C. McCusker, P. Nielsen, A. Outhred, *et al.*, “The upper end of the observed cosmic ray energy

- spectrum,” *Journal of Physics A: Mathematical, Nuclear and General*, vol. 7, no. 8, p. 990, 1974.
- [76] J. Abraham *et al.*, “Observation of the Suppression of the Flux of Cosmic Rays above 4×10^{19} eV,” *Phys. Rev. Lett.*, vol. 101, p. 061101, Aug 2008.
- [77] D. Bird, S. Corbató, H. Dai, B. Dawson, J. Elbert, T. Gaisser, K. Green, M. Huang, D. Kieda, S. Ko, *et al.*, “Evidence for correlated changes in the spectrum and composition of cosmic rays at extremely high energies,” *Physical review letters*, vol. 71, no. 21, p. 3401, 1993.
- [78] M. Dyakonov, N. Efimov, T. Egorov, A. Glushkov, S. Knurenko, V. Kolosov, I. Makarov, V. Pavlov, P. Petrov, M. Pravdin, *et al.*, “Primary energy spectrum of cosmic rays with $e_0 \simeq 10^{16}$ - 10^{20} ev on data of the yakutsk array,” in *International Cosmic Ray Conference*, vol. 2, p. 93, 1991.
- [79] R. Knapik, *The cosmic ray energy spectrum from 1-10 EXA electron volts measured by the Pierre Auger Observatory*. PhD thesis, 2009.
- [80] N. Chiba, K. Hashimoto, N. Hayashida, K. Honda, M. Honda, N. Inoue, F. Kakimoto, K. Kamata, S. Kawaguchi, N. Kawasumi, Y. Matsubara, K. Murakami, M. Nagano, S. Ogie, H. Ohoka, T. Saito, Y. Sakuma, I. Tsushima, M. Teshima, T. Umezawa, S. Yoshida, and H. Yoshii, “Akeno Giant Air Shower Array (AGASA) covering 100 km² area,” *Nuclear Instruments and Methods in Physics Research Section A: Accelerators, Spectrometers, Detectors and Associated Equipment*, vol. 311, pp. 338–349, 1992.
- [81] R. Baltrusaitis, R. Cady, G. Cassiday, R. Cooperv, J. Elbert, P. Gerhardy, S. Ko, E. Loh, M. Salamon, D. Steck, and P. Sokolsky, “The Utah Fly’s Eye detector,” *Nuclear Instruments and Methods in Physics Research Section A: Accelerators, Spectrometers, Detectors and Associated Equipment*, vol. 240, no. 2, pp. 410–428, 1985.

- [82] R. Tennent, “The Haverah Park extensive air shower array,” *Proceedings of the Physical Society*, vol. 92, no. 3, p. 622, 1967.
- [83] R. Abbasi, T. Abu-Zayyad, J. Amann, G. Archbold, J. Bellido, K. Belov, J. Belz, D. Bergman, Z. Cao, R. Clay, *et al.*, “Measurement of the flux of ultrahigh energy cosmic rays from monocular observations by the High Resolution Fly’s Eye experiment,” *Physical review letters*, vol. 92, no. 15, p. 151101, 2004.
- [84] M. M. Winn, J. Ulrichs, L. S. Peak, C. B. A. McCusker, and L. Horton, “The cosmic-ray energy spectrum above 10^{17} eV,” *Journal of Physics G: Nuclear Physics*, vol. 12, no. 7, p. 653, 1986.
- [85] A. Borione, C. Covault, J. Cronin, B. Fick, K. Gibbs, H. Krimm, N. Mascarenhas, T. McKay, D. Müller, B. Newport, R. Ong, L. Rosenberg, H. Sanders, M. Catanese, D. Ciampa, K. Green, J. Kolodziejczak, J. Matthews, D. Nitz, D. Sinclair, and J. van der Velde, “A large air shower array to search for astrophysical sources emitting γ -rays with energies 10^{14} eV,” *Nuclear Instruments and Methods in Physics Research Section A: Accelerators, Spectrometers, Detectors and Associated Equipment*, vol. 346, no. 1–2, pp. 329–352, 1994.
- [86] J. Abraham *et al.*, “Trigger and Aperture of the Surface Detector Array of the Pierre Auger Observatory,” *Nuclear Instruments and Methods in Physics Research Section A: Accelerators, Spectrometers, Detectors and Associated Equipment*, vol. 613, pp. 29–39, 2010.
- [87] I. Allekotte, A. Barbosa, P. Bauleo, C. Bonifazi, B. Civit, C. Escobar, B. Garc a, G. Guedes, M. G. Berisso, J. Harton, M. Healy, M. Kaducak, P. Mantsch, P. Mazur, C. Newman-Holmes, I. Pepe, I. Rodriguez-Cabo, H. Salazar, N. S.-D. Grande, and D. Warner, “The surface detector system of the Pierre Auger Observatory,” *Nuclear*

- Instruments and Methods in Physics Research Section A: Accelerators, Spectrometers, Detectors and Associated Equipment*, vol. 586, no. 3, pp. 409–420, 2008.
- [88] X. Bertou, P. Allison, C. Bonifazi, P. Bauleo, C. Grunfeld, M. Aglietta, F. Arneodo, D. Barnhill, J. Beatty, A. Creusot, *et al.*, “Calibration of the surface array of the Pierre Auger Observatory,” *Nuclear Instruments and Methods in Physics Research Section A: Accelerators, Spectrometers, Detectors and Associated Equipment*, vol. 568, no. 2, pp. 839–846, 2006.
- [89] A. Hillas Proc. of the 12th Int. Conf. on Cosmic Rays, Proc. of the 12th Int. Conf. on Cosmic Rays, 1971.
- [90] D. Newton, J. Knapp, and A. Watson, “The Optimum Distance at which to Determine the Size of a Giant Air Shower,” *Astropart.Phys.*, vol. 26, pp. 414–419, 2007.
- [91] J. Hersil, I. Escobar, D. Scott, G. Clark, and S. Olbert, “Observations of Extensive Air Showers near the Maximum of Their Longitudinal Development,” *Phys. Rev. Lett.*, vol. 6, pp. 22–23, Jan 1961.
- [92] P. Abreu, M. Aglietta, E. Ahn, I. Albuquerque, D. Allard, I. Allekotte, J. Allen, P. Allison, J. A. Castillo, J. Alvarez-Muñiz, *et al.*, “The Pierre Auger observatory I: the cosmic ray energy spectrum and related measurements,” *arXiv preprint arXiv:1107.4809*, 2011.
- [93] J. Abraham *et al.*, “The fluorescence detector of the Pierre Auger Observatory,” *Nuclear Instruments and Methods in Physics Research Section A: Accelerators, Spectrometers, Detectors and Associated Equipment*, vol. 620, pp. 227–251, Aug 2010.
- [94] A. N. Bunner, *Cosmic ray detection by atmospheric fluorescence*. PhD thesis, Cornell University, 1967.

- [95] M. Ave, M. Bohacova, B. Buonomo, N. Busca, L. Cazon, S. Chemerisov, M. Conde, R. Crowell, P. Di Carlo, C. Di Giulio, *et al.*, “Measurement of the pressure dependence of air fluorescence emission induced by electrons,” *Astroparticle physics*, vol. 28, no. 1, pp. 41–57, 2007.
- [96] R. Nicholls, E. Reeves, and D. Bromley, “Excitation of n2 and o2 by 1/2 and 1 mev protons,” *Proceedings of the Physical Society*, vol. 74, no. 1, p. 87, 1959.
- [97] T. Waldenmaier, J. Blümer, and H. Klages, “Spectral resolved measurement of the nitrogen fluorescence emissions in air induced by electrons,” *Astroparticle Physics*, vol. 29, no. 3, pp. 205–222, 2008.
- [98] M. Ave, M. Bohacova, B. Buonomo, L. Cazon, S. Chemerisov, M. Conde, R. Crowell, P. Di Carlo, C. Di Giulio, M. Doubrava, *et al.*, “Spectrally resolved pressure dependence measurements of air fluorescence emission with AIRFLY,” *Nuclear Instruments and Methods in Physics Research Section A: Accelerators, Spectrometers, Detectors and Associated Equipment*, vol. 597, no. 1, pp. 41–45, 2008.
- [99] J. Blümer, R. Engel, and J. R. Hörandel, “Cosmic Rays from the knee to the highest energies,” *Progress in Particle and Nuclear Physics*, vol. 63, pp. 293–338, 2009.
- [100] R. Engel, D. Heck, and T. Pierog, “Extensive air Showers and hadronic interactions at high energy,” *Annual Review of Nuclear and Particle Science*, vol. 61, pp. 467–489, 2011.
- [101] Mainz, Germany, www.shott.com, *Schott Glaswerke*.
- [102] C. Aramo, M. Ambrosio, F. Bracci, P. Facal, R. Fonte, G. Gallo, E. Kemp, G. Matthiae, D. Nicotra, P. Privitera, G. Raia, E. Tusi, and G. Vitali, “The camera of the Pierre Auger Observatory Fluorescence Detector,” *Nuclear Instruments and Methods*

- in Physics Research Section A: Accelerators, Spectrometers, Detectors and Associated Equipment*, vol. 478, pp. 125–129, 2002.
- [103] A. Aab *et al.*, “The Pierre Auger Observatory: Contributions to the 33rd International Cosmic Ray Conference (ICRC 2013),” 2013.
- [104] P. Abreu *et al.*, “The Pierre Auger Observatory IV: Operation and Monitoring,” 2011.
- [105] H. Photonics, *Photomultiplier tubes*. Hamamatsu, 2000.
- [106] C. Aramo *et al.*, “Optical relative calibration and stability monitoring for the Auger fluorescence detector,” 2005.
- [107] Proceeding 29th ICRC, *Absolute Calibration of the Auger Fluorescence Detectors*, 2005.
- [108] A. Rovero, P. Bauleo, J. Brack, J. Harton, and R. Knapik, “Multi-wavelength calibration procedure for the pierre Auger Observatory Fluorescence Detectors,” *Astroparticle Physics*, vol. 31, no. 4, pp. 305–311, 2009.
- [109] *LS-1130-41100 Series FlashPac with FX-1160 xenon flash lamp with reflector and borosikicate window from Perkin Elmer Opto-electronics*.
- [110] S. BenZvi, R. Cester, M. Chiosso, B. Connolly, A. Filipčič, B. García, A. Grillo, F. Guarino, M. Horvat, M. Iarlori, C. Macolino, J. Matthews, D. Melo, R. Mussa, M. Mostafá, J. Pallota, S. Petrera, M. Prouza, V. Rizi, M. Roberts, J. R. Rojo, F. Salamida, M. Santander, G. Sequeiros, A. Tonachini, L. Valore, D. Veberič, S. Westerhoff, D. Zavrtanik, and M. Zavrtanik, “The Lidar system of the Pierre Auger Observatory,” *Nuclear Instruments and Methods in Physics Research Section A: Accelerators, Spectrometers, Detectors and Associated Equipment*, vol. 574, no. 1, pp. 171–184, 2007.
- [111] J. Abraham *et al.*, “Calibration and Monitoring of the Pierre Auger Observatory,” 2009.

- [112] B. Fick, M. Malek, J. A. J. Matthews, J. Matthews, R. Meyhandan, M. Mostafá, M. Roberts, P. Sommers, and L. Wiencke, “The Central Laser Facility at the Pierre Auger Observatory,” *Journal of Instrumentation*, vol. 1, no. 11, p. P11003, 2006.
- [113] P. Abreu *et al.*, “Techniques for Measuring Aerosol Attenuation using the Central Laser Facility at the Pierre Auger Observatory,” *JINST*, vol. 8, p. P04009, 2013.
- [114] P. Abreu, M. Aglietta, M. Ahlers, E. Ahn, I. Albuquerque, D. Allard, I. Allekotte, J. Allen, P. Allison, A. Almela, *et al.*, “Description of atmospheric conditions at the Pierre Auger Observatory using the global data assimilation system (GDAS),” *Astroparticle Physics*, vol. 35, no. 9, pp. 591–607, 2012.
- [115] W. Apel *et al.*, “Cosmic Ray Measurements with the KASCADE-Grande Experiment,” 2009.
- [116] J. Barranco, G. Contreras, D. Delepine, and M. Napsuciale, “Particles and fields. Proceedings, 13th Mexican Workshop, Leon, Mexico, October 20-26, 2011,” 2012.
- [117] C. Meurer, N. Collaboration, *et al.*, “HEAT-a low energy enhancement of the Pierre Auger Observatory,” *arXiv preprint arXiv:1106.1329*, 2011.
- [118] F. Sanchez, “The AMIGA detector of the Pierre Auger Observatory: An overview,” 2011.
- [119] N. Scharf, T. Hebbeker, and C. Meurer, “HEAT Energy Spectrum,” 2012.
- [120] M. Settimo, “Measurement of the cosmic ray energy spectrum using hybrid events of the Pierre Auger Observatory,” *The European Physical Journal Plus*, vol. 127, no. 8, pp. 1–15, 2012.
- [121] J. Abraham *et al.*, “Measurement of the energy spectrum of cosmic rays above 10^{18} eV using the Pierre Auger Observatory,” *Physics Letters B*, vol. 685, pp. 239–246, 2010.

- [122] M. Ave, M. Bohacova, B. Buonomo, L. Cazon, S. Chemerisov, M. Conde, R. Crowell, P. Di Carlo, C. Di Giulio, M. Doubrava, *et al.*, “Energy dependence of air fluorescence yield measured by AIRFLY,” *Nuclear Instruments and Methods in Physics Research Section A: Accelerators, Spectrometers, Detectors and Associated Equipment*, vol. 597, no. 1, pp. 46–49, 2008.
- [123] J. Brack, R. Cope, A. Dorofeev, B. Gookin, J. Harton, *et al.*, “Absolute Calibration of a Large-diameter Light Source,” *JINST*, vol. 8, p. P05014, 2013.
- [124] D. Boncioli *et al.*, “Cosmic Ray composition with the Pierre Auger Observatory,” in *Proceedings for the RICAP 2013*, 2013.
- [125] M. Unger, “Composition Studies with the Pierre Auger Observatory,” *Nuclear Physics B - Proceedings Supplements*, vol. 190, no. 0, pp. 240–246, 2009.
- [126] J. Abraham, P. Abreu, M. Aglietta, E. Ahn, D. Allard, I. Allekotte, J. Allen, J. Alvarez-Muniz, M. Ambrosio, L. Anchordoqui, *et al.*, “Measurement of the Depth of Maximum of Extensive Air Showers above 10^{18} eV,” *Physical review letters*, vol. 104, no. 9, p. 91101, 2010.
- [127] P. Abreu, M. Aglietta, E. Ahn, I. Albuquerque, D. Allard, I. Allekotte, J. Allen, P. Allison, J. A. Castillo, J. Alvarez-Muñiz, *et al.*, “The pierre auger observatory ii: Studies of cosmic ray composition and hadronic interaction models,” *arXiv preprint arXiv:1107.4804*, 2011.
- [128] A. Aab *et al.*, “Depth of Maximum of Air-Shower Profiles at the Pierre Auger Observatory: Measurements at Energies above $10^{17.8}$ eV,” *Phys.Rev.D*, 2014.
- [129] P. Abreu, M. Aglietta, E. Ahn, I. Albuquerque, D. Allard, I. Allekotte, J. Allen, P. Allison, J. A. Castillo, J. Alvarez-Muñiz, *et al.*, “The pierre auger observatory ii:

- Studies of cosmic ray composition and hadronic interaction models,” *arXiv preprint arXiv:1107.4804*, 2011.
- [130] P. Sokolsky and f. t. H. Collaboration, “Final Results from the High Resolution Fly’s Eye (HiRes) Experiment,” *PoS*, vol. ICHEP2010, p. 444, 2010.
- [131] Y. Petrov, *Constraints on the Galactic Magnetic Field with Two Point Cumulative Autocorrelation Function*. PhD thesis, Colorado State University, 2012.
- [132] J. Abraham, M. Aglietta, I. Aguirre, M. Albrow, D. Allard, I. Allekotte, P. Allison, J. Alvarez Muñiz, M. Do Amaral, M. Ambrosio, *et al.*, “Properties and performance of the prototype instrument for the Pierre Auger Observatory,” *Nuclear Instruments and Methods in Physics Research Section A: Accelerators, Spectrometers, Detectors and Associated Equipment*, vol. 523, no. 1, pp. 50–95, 2004.
- [133] P. Bauleo, A. Etchegoyen, J. Niello, A. Ferrero, A. Filevich, C. Guerard, F. Hasenbalg, M. Mostafa, D. Ravignani, and J. R. Martino, “A water tank Cherenkov detector for very high-energy astroparticles,” *Nuclear Instruments and Methods in Physics Research Section A: Accelerators, Spectrometers, Detectors and Associated Equipment*, vol. 406, no. 1, pp. 69–77, 1998.
- [134] X. Bertou, P. Allison, C. Bonifazi, P. Bauleo, C. Grunfeld, M. Aglietta, F. Arneodo, D. Barnhill, J. Beatty, N. Busca, *et al.*, “Calibration of the surface array of the Pierre Auger Observatory,” *Nuclear Instruments and Methods in Physics Research Section A: Accelerators, Spectrometers, Detectors and Associated Equipment*, vol. 568, no. 2, pp. 839–846, 2006.
- [135] R. Pesce, “Energy calibration of data recorded with the surface detectors of the Pierre Auger Observatory: An update,” 2011.

- [136] M. Ave, M. Bohacova, K. Daumiller, P. Di Carlo, C. Di Giulio, P. San Luis, D. Gonzales, C. Hojvat, J. Hörandel, M. Hrabovsky, *et al.*, “Precise Measurement of the Absolute Fluorescence Yield,” in *AIP Conference Proceedings*, vol. 1367, p. 29, 2011.
- [137] M. Ave, M. Bohacova, B. Buonomo, L. Cazon, S. Chemerisov, M. Conde, R. Crowell, P. Di Carlo, C. Di Giulio, M. Doubrava, *et al.*, “Measurement of the pressure dependence of air fluorescence emission induced by electrons,” *Astroparticle physics*, vol. 28, no. 1, pp. 41–57, 2007.
- [138] J. Abraham, P. Abreu, M. Aglietta, C. Aguirre, E. Ahn, D. Allard, I. Allekotte, J. Allen, P. Allison, J. Alvarez-Muniz, *et al.*, “Atmospheric effects on extensive air showers observed with the Surface Detector of the Pierre Auger Observatory,” *Astroparticle Physics*, vol. 32, no. 2, pp. 89–99, 2009.
- [139] J. Abraham *et al.*, “A Study of the Effect of Molecular and Aerosol Conditions in the Atmosphere on Air Fluorescence Measurements at the Pierre Auger Observatory,” *Astropart.Phys.*, vol. 33, pp. 108–129, 2010.
- [140] E. Mayotte, L. Wiencke, V. Rizi, A. Grillo, *et al.*, “The Central Raman Laser Facility at the Pierre Auger Observatory,” in *AGU Fall Meeting Abstracts*, vol. 1, p. 0310, 2013.
- [141] P. Abreu, M. Aglietta, M. Ahlers, E. Ahn, I. Albuquerque, I. Allekotte, J. Allen, P. Allison, A. Almela, J. Alvarez Castillo, *et al.*, “Identifying clouds over the Pierre Auger Observatory using infrared satellite data,” *Astroparticle Physics*, vol. 50, pp. 92–101, 2013.
- [142] A. Aab, J. Aublin, P. Billoir, M. Blanco, L. Caccianiga, R. Dallier, R. Gaior, D. Garcia-Gamez, P. Ghia, P. Lautridou, *et al.*, “Origin of atmospheric aerosols at the Pierre Auger Observatory using studies of air mass trajectories in South America,” 2014.

- [143] A. Bucholtz, “Rayleigh-scattering calculations for the terrestrial atmosphere,” *Appl. Opt.*, vol. 34, pp. 2765–2773, May 1995.
- [144] L. Tomankova, “Pierre Auger Fluorescence Detector Analysis of Relative Calibration Data,” Master’s thesis, Czech Technical Univeristy, 2012.
- [145] *NSHU550 UV LED*, *Nichia America Corp.* 48561 Alpha Dr. Wixom, MI.
- [146] J. Brack, R. Meyhandan, G. Hofman, and J. Matthews, “Absolute photometric calibration of large aperture optical systems,” *Astroparticle Physics*, vol. 20, no. 6, pp. 653–659, 2004.
- [147] “ μ Clinux Embedded Linux/Microcontroller Project.” <http://www.uclinux.org/description/>.
- [148] T. Larason, S. Bruce, and A. Parr, “NIST special Publication 250-41: NIST measurement services,” *Natl. Bur. Stand.*, pp. 46–50, 1998.
- [149] E. G. Ramberg, “Optical factors in the photoemission of thin films,” *Applied optics*, vol. 6, no. 12, pp. 2163–2170, 1967.
- [150] S.-O. Flyckt, *Photomultiplier tubes: principles and applications*. Photonis, 2002.
- [151] R. Knapik, P. Bauleo, B. Becker, J. Brack, R. Caruso, C. D. Fratte, A. Dorofeev, J. Harton, A. Insolia, J. Matthews, *et al.*, “The absolute, relative and multi-wavelength calibration of the Pierre Auger Observatory fluorescence detectors,” *arXiv preprint arXiv:0708.1924*, 2007.
- [152] L. Wiencke and t. P. A. Collaboration, “Atmospheric calorimetry above 10^{19} ev: Shooting lasers at the Pierre Auger Cosmic-Ray Observatory,” *Journal of Physics: Conference Series*, vol. 160, no. 1, p. 012037, 2009.
- [153] P. Abreu *et al.*, “Techniques for Measuring Aerosol Attenuation using the Central Laser Facility at the Pierre Auger Observatory,” *JINST*, vol. 8, p. P04009, 2013.

- [154] J. A. Matthews, “Optical calibration of the Auger fluorescence telescopes,” in *Astronomical Telescopes and Instrumentation*, pp. 121–130, International Society for Optics and Photonics, 2003.
- [155] *SpectraPro-150*, <http://ridl.cfd.rit.edu/products/manuals/Acton/old/MANUAL/Sp-150.pdf>.
- [156] *PAX- 10 10-Watt Precision-Aligned Pulsed Xenon Light Source*.
- [157] *OceanOptics USB2000-UV Spectrometer*, <http://www.oceanoptics.com/products/usb2000uvvis.asp>.
- [158] “cURL Website.” <http://curl.haxx.se/>.
- [159] “Schott Glass Manufactures website.” <http://www.us.schott.com/english/index.html>.
- [160] “Schott Glass Borofloat 33 product information.” <http://www.us.schott.com/borofloat/english/attribute/optical>.
- [161] “Schott Glass P-BK7 Datasheet.” http://www.schott.com/advanced_optics/us/abbe_datasheets/schott_datasheet_all_us.pdf.
- [162] M. Unger, B. R. Dawson, R. Engel, F. Schüssler, and R. Ulrich, “Reconstruction of longitudinal profiles of ultra-high energy cosmic ray showers from fluorescence and cherenkov light measurements,” *Nuclear Instruments and Methods in Physics Research Section A: Accelerators, Spectrometers, Detectors and Associated Equipment*, vol. 588, no. 3, pp. 433–441, 2008.
- [163] T. P. A. Collaboration, “The Pierre Auger Cosmic Ray Observatory.” 2015.
- [164] T. Gaisser and A. Hillas, “Proceedings of the 15th ICRC,” 1977.
- [165] M. J. Tueros, “Estimate of the non-calorimetric energy of showers observed with the fluorescence and surface detectors of the pierre auger observatory,” in *Proceedings of the International Cosmic Ray Conference*, 2013.

- [166] A. Obermeier, *The fluorescence yield of air excited by electrons measured with the AIRFLY experiment*. Forschungszentrum Karlsruhe in der Helmholtz-Gemeinschaft, 2007.
- [167] M. Ave, M. Bohacova, E. Curry, P. Di Carlo, C. Di Giulio, P. F. San Luis, D. Gonzales, C. Hojvat, J. Hörandel, M. Hrabovsky, *et al.*, “Precise measurement of the absolute fluorescence yield of the 337nm band in atmospheric gases,” *Astroparticle Physics*, vol. 42, pp. 90–102, 2013.
- [168] D. K. Killinger and N. Menyuk, “Laser remote sensing of the atmosphere,” *Science*, vol. 235, no. 4784, pp. 37–45, 1987.
- [169] A. Bucholtz, “Rayleigh-scattering calculations for the terrestrial atmosphere,” *Applied Optics*, vol. 34, no. 15, pp. 2765–2773, 1995.
- [170] H. Naus and W. Ubachs, “Experimental verification of rayleigh scattering cross sections,” *Optics Letters*, vol. 25, no. 5, pp. 347–349, 2000.
- [171] A. Ångström, “On the atmospheric transmission of sun radiation. ii,” *Geografiska Annaler*, pp. 130–159, 1930.
- [172] E. J. McCartney, “Optics of the atmosphere: scattering by molecules and particles,” *New York, John Wiley and Sons, Inc., 1976. 421 p.*, vol. 1, 1976.
- [173] T. Eck, B. Holben, J. Reid, O. Dubovik, A. Smirnov, N. O’neill, I. Slutsker, and S. Kinne, “Wavelength dependence of the optical depth of biomass burning, urban, and desert dust aerosols,” *Journal of Geophysical Research: Atmospheres (1984–2012)*, vol. 104, no. D24, pp. 31333–31349, 1999.
- [174] D. Heck, J. Knapp, J. Capdevielle, G. Schatz, T. Thouw, *et al.*, *CORSIKA: A Monte Carlo code to simulate extensive air showers*, vol. 6019. FZKA, 1998.
- [175] “CC-IN2P3 Website.” <http://cc.in2p3.fr/?lang=en>.

- [176] K. Werner, “The hadronic interaction model epos,” *Nuclear Physics B-Proceedings Supplements*, vol. 175, pp. 81–87, 2008.
- [177] J. Abraham *et al.*, “Measurement of the Proton-Air Cross Section at $s = \sqrt{57}$ TeV with the Pierre Auger Observatory,” *Physical Review Letters*, vol. 109, 2012.
- [178] S. Argiro, S. Barroso, J. Gonzalez, L. Nellen, T. Paul, T. Porter, L. Prado Jr, M. Roth, R. Ulrich, and D. Veberič, “The offline software framework of the pierre auger observatory,” *Nuclear Instruments and Methods in Physics Research Section A: Accelerators, Spectrometers, Detectors and Associated Equipment*, vol. 580, no. 3, pp. 1485–1496, 2007.
- [179] K. Kamata and J. Nishimura, “The lateral and the angular structure functions of electron showers,” *Progress of Theoretical Physics Supplement*, vol. 6, pp. 93–155, 1958.
- [180] K. Greisen, “Highlights in air shower studies, 1965.,” in *International Cosmic Ray Conference*, vol. 2, p. 609, 1965.
- [181] L. Prado Jr, B. Dawson, S. Petrerá, R. Shellard, M. Do Amaral, R. Caruso, R. Sato, and J. Bellido, “Simulation of the fluorescence detector of the pierre auger observatory,” *Nuclear Instruments and Methods in Physics Research Section A: Accelerators, Spectrometers, Detectors and Associated Equipment*, vol. 545, no. 3, pp. 632–642, 2005.
- [182] D. Gora, R. Engel, D. Heck, P. Homola, H. Klages, M. Risse, B. Wilczyńska, H. Wilczyński, *et al.*, “Universal lateral distribution of energy deposit in air showers and its application to shower reconstruction,” *Astroparticle Physics*, vol. 24, no. 6, pp. 484–494, 2006.
- [183] M. Roberts, “The role of atmospheric multiple scattering in the transmission of fluorescence light from extensive air showers,” *Journal of Physics G: Nuclear and Particle Physics*, vol. 31, no. 11, p. 1291, 2005.

- [184] P. Abreu *et al.*, “Measurement of the Cosmic Ray Energy Spectrum Using Hybrid Events of the Pierre Auger Observatory,” *Eur.Phys.J.Plus*, vol. 127, p. 87, 2012.
- [185] V. Verzi, “The energy scale of the pierre auger observatory,” *Proc. 33rd ICRC, Rio de Janeiro, Brasil*, pp. 15–18, 2013.
- [186] P. K. Grieder, *Extensive Air Showers*. Springer, 2010.
- [187] G. Cowan, *Statistical data analysis*. Oxford University Press, 1998.

APPENDIX A

MEASURED MULTI-WAVELENGTH CALIBRATIONS

Below are the four measured relative efficiencies of the telescopes measured in March 2014. The results measured in this thesis are shown as the solid curves, the error bars are the estimated statistical uncertainties, and the brackets are the estimated systematic uncertainties. All data are taken relative to the value at 375 nm.

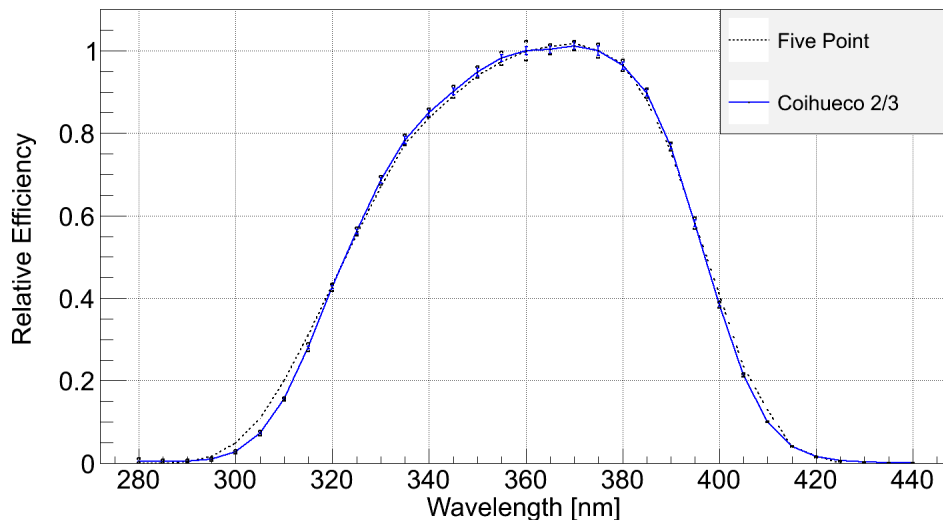


FIGURE A.1. Calibration for Coihueco bays two and three.

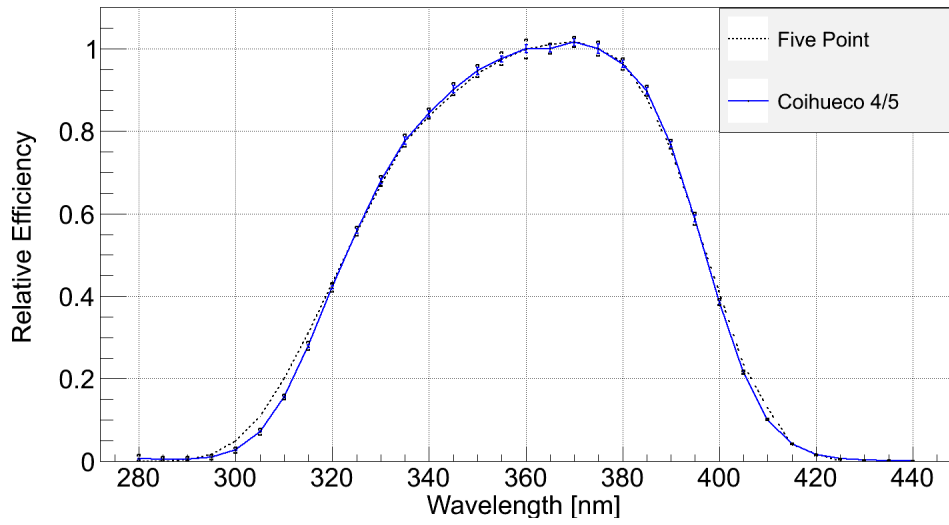


FIGURE A.2. Calibration for Coihueco bays four and five, to also be used in bays one and six, along with Loma Amarilla and HEAT.

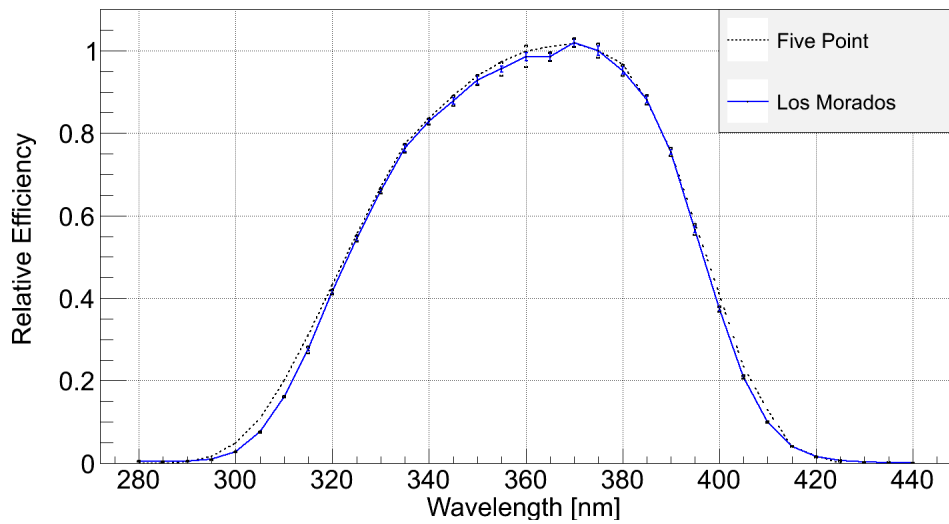


FIGURE A.3. Calibration for Los Morados, for use in all the bays.

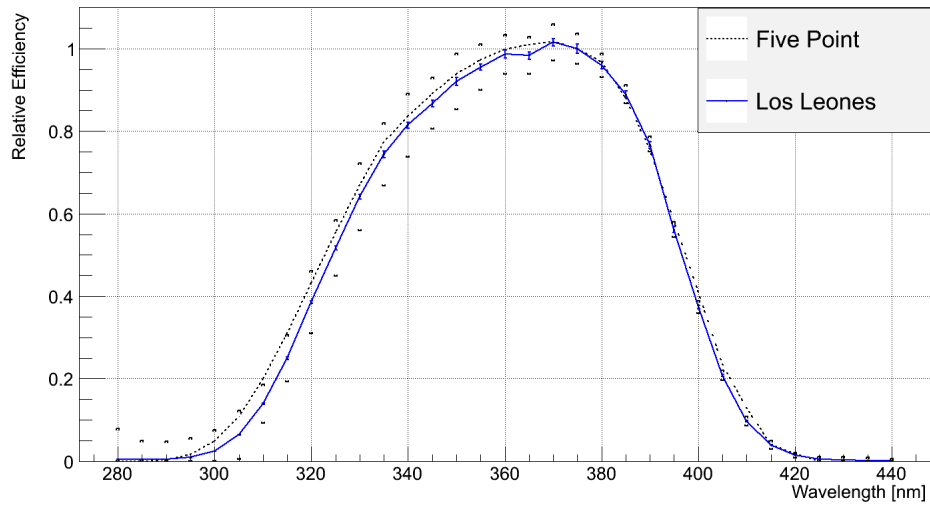


FIGURE A.4. Calibration for Los Leones, large systematic uncertainties are due to the comparison between the measurements at bays three and four.

APPENDIX B

RECONSTRUCTED X_{max} DISTRIBUTIONS

These are the histograms for the reconstructed X_{max} values for the $\Delta\log(E/eV) = 0.1$ energy bins, starting with the $10^{17.8}$ to $10^{17.9}$ eV in the upper left plot. The x-axis is X_{max} in g/cm^2 , but is not shown in the figures for clarity, and the binning for each distribution depends on the square root of the entries for that energy bin.

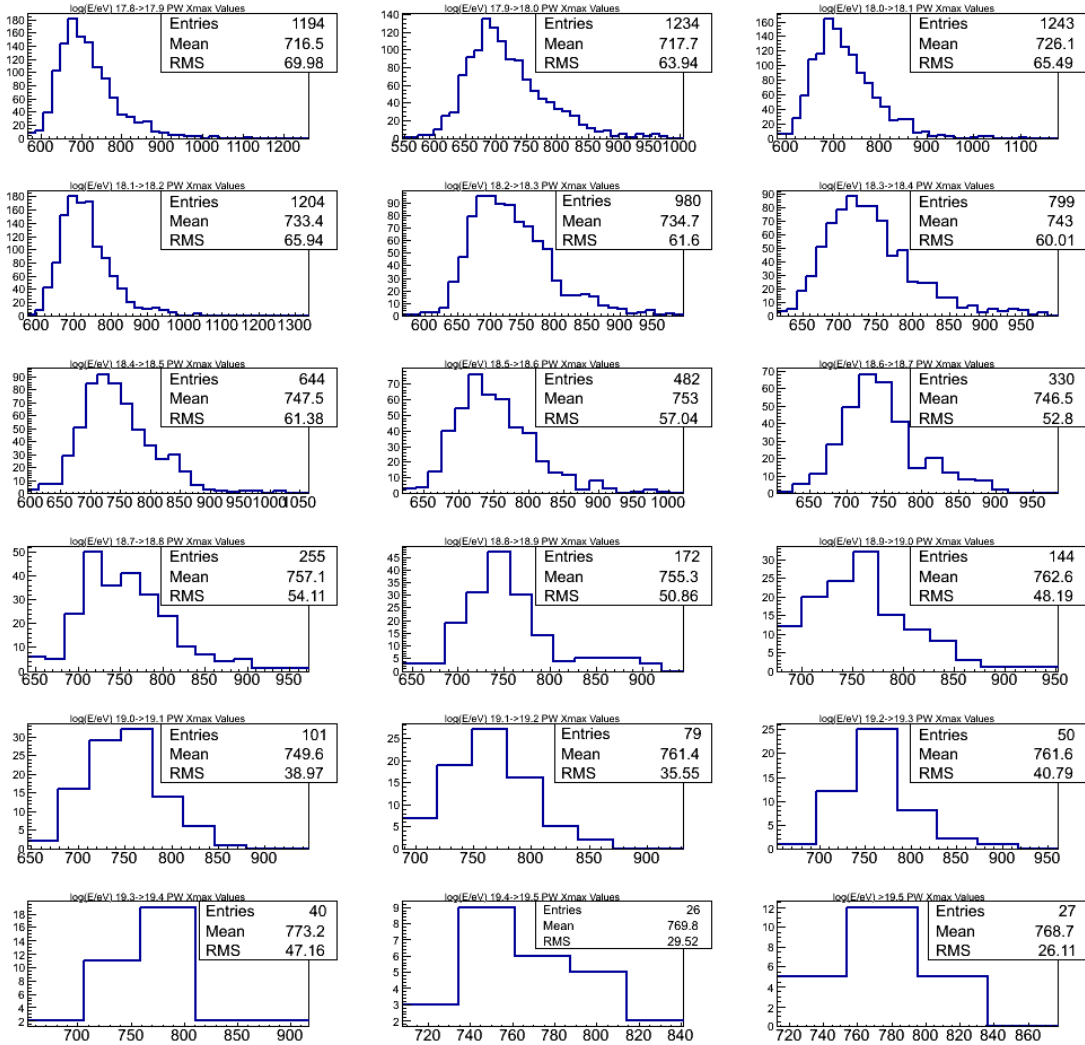


FIGURE B.1. X_{max} distributions for the golden data reconstructed with the the piece-wise calibration, where each plot is $\Delta\log(E/eV)=0.1$, starting with 17.8 to 17.9 in the upper left. The x-axis is X_{max} in g/cm^2 , but is not shown for clarity.

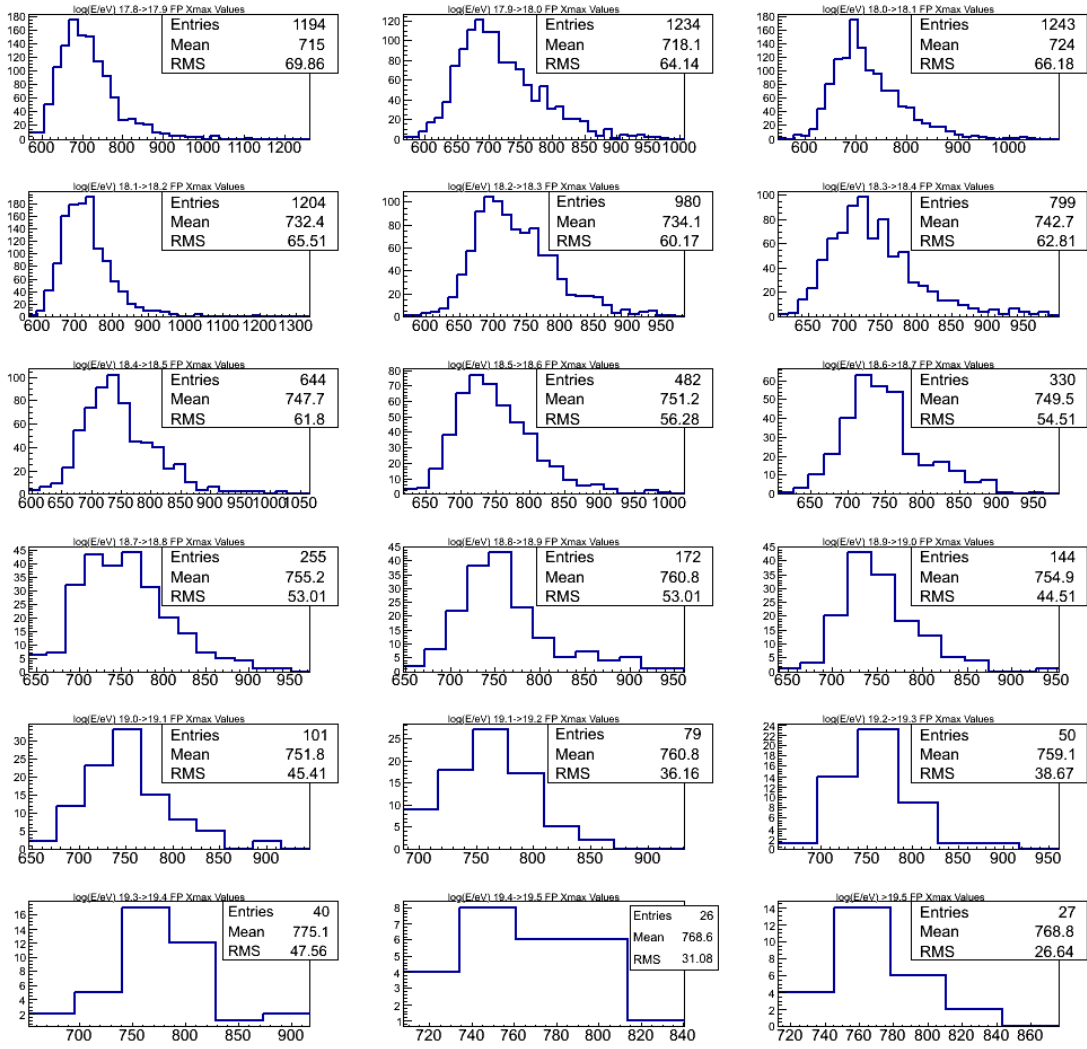


FIGURE B.2. X_{max} distributions for the golden data reconstructed with the five-point calibration.

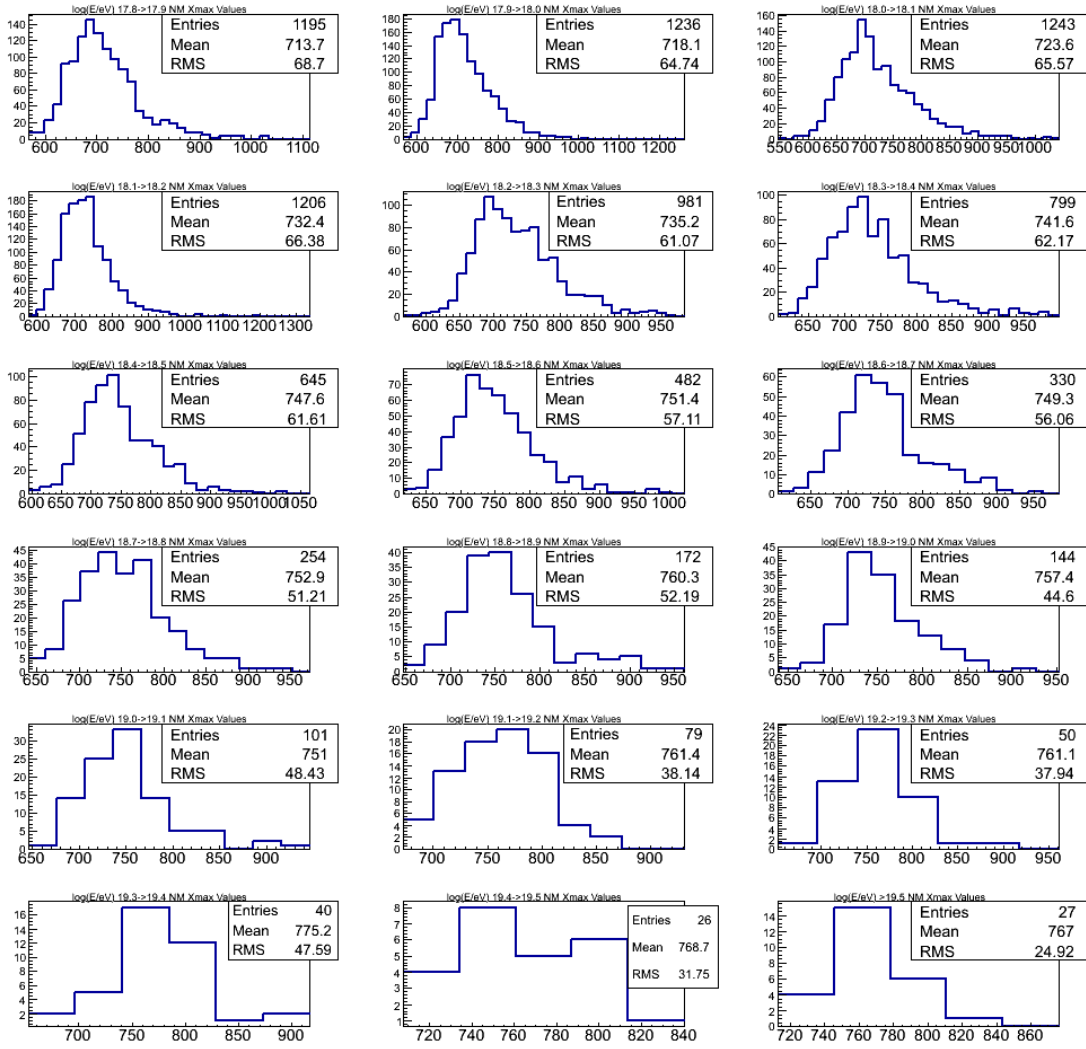


FIGURE B.3. X_{max} distributions for the new-multi-wavelength calibration, the work described in this thesis, for the eighteen energy bins.